UNIVERSIDADE DE SÃO PAULO
FFCLRP - DEPARTAMENTO DE FÍSICA
PÓS-GRADUAÇÃO EM FÍSICA APLICADA À MEDICINA E BIOLOGIA

Síntese e Caracterização de Nanopartículas Magnéticas para Aplicações Biomédicas

SOUDABEH ARSALANI

Tese apresentada à Faculdade de Filosofia, Ciências e Letras de Ribeirão Preto da Universidade de São Paulo, como parte das exigências para a obtenção do título de Doutor em Ciências, Área: Física aplicada à Medicina e Biologia

Ribeirão Preto - SP
2020

SOUDABEH ARSALANI

Síntese e Caracterização de Nanopartículas Magnéticas para Aplicações Biomédicas

Tese apresentada à Faculdade de Filosofia, Ciências e Letras de Ribeirão Preto da Universidade de São Paulo, como parte das exigências para a obtenção do título de Doutor em Ciências, Área: Física aplicada à Medicina e Biologia

Área de Concentração:
Física aplicada à Medicina e Biologia.
Orientador:
Oswaldo Baffa Filho

Ribeirão Preto –SP
2020

SOUDABEH ARSALANI

Synthesis and Characterization of Magnetic Nanoparticles for Biomedical Applications

A thesis submitted in partial fulfillment of the requirements for the degree of Doctor of Philosophy Department of Physics, Faculty of Philosophy, Sciences and Letters of Ribeirão Preto, University of São Paulo.

Study Area:

Physics Applied to Medicine and Biology

Supervisor:

Oswaldo Baffa Filho

Ribeirão Preto –SP

2020

FICHA CATALOGRÁFICA

Arsalani, Soudabeh

Síntese e Caracterização de Nanopartículas Magnéticas para Aplicações Biomédicas/ Soudabeh Arsalani; orientador Oswaldo Baffa Filho. Ribeirão Preto - SP, 2020.

111 f.:il.

Tese (Doutorado - Programa de Pós-Graduação em Física Aplicada à Medicina e Biologia) - Faculdade de Filosofia, Ciências e Letras de Ribeirão Preto da Universidade de São Paulo, 2020.

1. Nanopartículas magnéticas. 2. Imagem por ressonância magnética. 3. Radio-luminescência. 4. Imagem por partículas magnéticas.

Nome: Soudabeh Arsalani

Título: Síntese e Caracterização de Nanopartículas Magnéticas para Aplicações Biomédicas.

Title: Synthesis and Characterization of Magnetic Nanoparticles for Biomedical Applications.

Tese apresentada à Faculdade de Filosofia, Ciências e Letras de Ribeirão Preto da Universidade de São Paulo, como parte das exigências para a obtenção do título de Doutor em Ciências.

Aprovado em: ____/____/____.

Banca examinadora

Prof. Dr.: _____ Instituição: _____
Julgamento: _____ Assinatura: _____

Prof. Dr.: _____ Instituição: _____
Julgamento: _____ Assinatura: _____

Prof. Dr.: _____ Instituição: _____
Julgamento: _____ Assinatura: _____

Prof. Dr.: _____ Instituição: _____
Julgamento: _____ Assinatura: _____

Prof. Dr.: _____ Instituição: _____
Julgamento: _____ Assinatura: _____

To my parents,

my sisters

and brother

for all their love and support

Acknowledgments

First of all, I would like to express my special and deepest gratitude to my supervisor Prof. Dr. Oswaldo Baffa Filho who gave me the opportunity to work under his guidance and knowledge. In addition, I am very thankful to him for his support, encouragement, patience and helping me to gain invaluable experiences during my PhD. I further like to thank him for giving me the opportunity to participate in national and international conferences. Many thanks for always being there no matter how busy life was.

My second acknowledge goes to Prof. Dr. Éder José Guidelli, who helped me very much in finalizing this project. Thanks for all your support, making me happy and motivated to work. I learned so much with you, I am really thankful to you.

I would like to thank to the co-authors of my publications and manuscripts of this thesis. I am delighted to have worked with you and I look forward to working with you again.

I am grateful of all my group members for the constant help, support and making a very nice working atmosphere in the group in the last four years. In addition, the technicians of our lab, Carlão and Lourenco, get my special thanks for always helping me and managing the laboratory.

I am profoundly grateful to Dr. Frank Wiekhorst for giving me the opportunity to work at Physikalisch-Technische Bundesanstalt (PTB), thereby using methods which were essential for improving the quality of this thesis. I am also very thankful to him and his group members, to make a very nice and friendly atmosphere to work, also helping and supporting me during the time that I worked there.

Tons of thanks to my friends for supporting, listening, offering me advice, and making me happy through this entire process. Special thanks to my close friends: Iara, Kleython, Alejandro, Jeferson, Thiru and Jenny for your welcoming, dinners and game nights. Your help and friendship were all greatly appreciated. Thank you for your friendship and sharing your life stories with me.

Finally, I would like to thank very much my beloved parents, sisters and brother. Without your endless love and encouragement, writing such a thesis would not have been possible. Special thanks to my lovely sister Seti for supporting me spiritually throughout these years and my life in general. Thanks a lot for all your help, kindness, and love.

Resumo

Arsalani, Soudabeh. **Síntese e Caracterização de Nanopartículas Magnéticas para Aplicações Biomédicas**. 2020 127f. Tese (Doutorado – Programa de Pós-graduação em Física Aplicada à Medicina e Biologia) – Faculdade de Filosofia, Ciências e Letras de Ribeirão Preto, Universidade de São Paulo, Ribeirão Preto – SP 2020

Nanomateriais magnéticos com distribuições específicas de tamanho e forma têm despertado grande interesse nos últimos anos devido às suas propriedades promissoras para aplicações biomédicas. Esta tese apresenta os resultados da síntese e caracterização de nanopartículas superparamagnéticas de óxido de ferro (SPIONs) para aplicações biomédicas. O primeiro grupo de SPIONs foi preparado por um método simples de co-precipitação verde a uma temperatura amena e tampado por látex de borracha natural (NRL) extraído de hevea brasiliensis. Os resultados mostraram que o tamanho do núcleo, a distribuição do tamanho, a magnetização e a temperatura de bloqueio das nanopartículas magnéticas (MNPs) podem ser controlados pela concentração de NRL. É importante ressaltar que os MNPs revestidos com NRL mostraram maior magnetização em comparação com os MNPs nus que podem sugerir que o NRL é um agente estabilizador eficaz para cobrir MNPs com magnetização aprimorada para aplicações biomédicas. O desempenho dos MNPs nus e dos MNPs revestidos por NRL foi investigado pelo sistema de ressonância magnética (MRI). Os resultados da ressonância magnética mostraram que o relaxamento do R2 depende fortemente da espessura da casca do MNR e diminui aumentando a espessura da casca do MNL. Além disso, as razões de relaxividade (r2 / r1) podem ser controladas ajustando a concentração de NRL. Portanto, MNPs revestidos com NRL podem ser considerados como agentes de contraste eficazes para aplicações de ressonância magnética. O segundo grupo de SPIONs com propriedades fluorescentes e radioluminescentes foi sintetizado pelo método de decomposição térmica, coberto com ácido oleico (OA) e modificado por antraceno (AN) e álcool polivinílico (PVA) como fluoróforo e agente de dispersão em solução aquosa, respectivamente. Este nanocompósito multifuncional exibia fortes bandas de emissão azul após exposição a raios UV e raios-X. Além disso, a intensidade de radioluminescência desse nanocompósito mostrou uma relação linear com a taxa de dose de raios-X, o que é altamente desejável para aplicações biomédicas. A última parte desta tese foi dedicada a restringir a distribuição de tamanhos de IONP (EMG 700, Ferrotec) revestida com surfactantes aniônicos que foram realizados usando o método de separação magnética de baixo gradiente (LGMS) (<15 T / m), para melhorar seu desempenho como rastreadores de imagem por partículas magnéticas (MPI). Amostras antes e depois do LGMS com diferentes concentrações de nanopartículas de magnetita (Fe_3O_4) foram fotografadas em um scanner MPI pré-clínico. As imagens das amostras após a separação mostraram uma melhor resolução MPI. Além disso, mostramos que a técnica LGMS é capaz de separar entidades maiores de MNP da suspensão em um curto período de tempo, o que nos permitiu ajustar a distribuição de tamanho e as propriedades magnéticas do MNP por meio de separação magnética controlada por tempo.

Palavras-chave: Nanopartículas magnéticas; Imagem por ressonância magnética; Fluorescência; Radio-luminescência; Separação magnética; Imagem por partículas magnéticas.

Abstract

Arsalani, Soudabeh. **Synthesis and Characterization of Magnetic Nanoparticles for Biomedical Applications**. 2020. 127p. A thesis submitted in partial fulfillment of the requirements for the degree of Doctor of Philosophy Department of Physics, Faculty of Philosophy, Sciences and literature of Ribeirão Preto – SP, 2020.

Magnetic nanomaterials with specific size and shape distributions have attracted a large interest in recent years due to their promising properties for biomedical applications. This thesis presents the results of the synthesis and characterization of superparamagnetic iron oxide nanoparticles (SPIONs) for biomedical applications. The first group of SPIONs was prepared by a simple green co-precipitation method at a mild temperature and capping by natural rubber latex (NRL) extracted from *Hevea brasiliensis*. The results showed core size, size distribution, magnetization and blocking temperature of the magnetic nanoparticles (MNPs) could be controlled by the NRL concentration. Importantly, NRL-coated MNPs showed higher magnetization compared to the bare MNPs that can suggest NRL is an effective stabilizing agent to cover MNPs with enhancing magnetization for biomedical applications. The performance of the bare MNPs and NRL-coated MNPs were investigated by magnetic resonance imaging (MRI) system. MRI results showed R2 relaxation strongly depends on the NRL shell thickness of MNPs and it decreases by increasing the shell thickness of NRL. In addition, the relaxivity ratios (r2/r1) can be controlled by adjusting the concentration of NRL. Therefore, NRL coated MNPs can be considered as effective contrast agents for MRI applications. The second group of SPIONs with fluorescent and radioluminescent properties were synthesized by the thermal decomposition method, covered with oleic acid (OA) and modified by anthracene (AN) and polyvinyl alcohol (PVA) as fluorophore and the dispersion agent in aqueous solution, respectively. This multifunctional nanocomposite exhibited sharp blue emission bands upon exposure to UV and X-ray. Furthermore, the radioluminescence intensity of this nanocomposite showed a linear relation with the X-ray dose rate, that is highly desirable for biomedical applications. The last part of this thesis was devoted to narrow the size distribution of IONP (EMG 700, Ferrotec) coated with anionic surfactants that carried out using low gradient magnetic separation (LGMS) (<15 T/m) method, to improve their performance as magnetic particles imaging (MPI) tracers. Samples before and after LGMS with different concentrations of magnetite (Fe_3O_4) nanoparticles were imaged in a preclinical MPI scanner. The images of the samples after separation showed an improved MPI resolution. Furthermore, we show that the LGMS technique is capable of separating larger MNP entities from the suspension in a short period of time which allowed us to adjust the size distribution and magnetic properties of MNP via time-controlled magnetic separation.

Keyword: Magnetic nanoparticles; Magnetic resonance imaging; Fluorescence; Radio-luminescence; Magnetic separation; Magnetic particle imaging.

Table of Figures

List of Tables

Table of Contents

Chapter 1: General Introduction

Nanotechnology is one of the fastest-growing research and development fields in the last decades in all over the world and is expected to be one of the major industries of this century. Nano-sized constructed materials, particularly nanoparticles (NPs), because of having new significant physical and chemical properties are useful tools for a plethora of applications such as information storage [1, 2], catalysis [3, 4], sensing [5, 6], food industry [7], water purification [8], and biomedicine [9].

There is a wide range of metal or metal-oxide NPs. These NPs usually consist of a core of the respective metal/metal oxide which is surrounded by a ligand shell. Among all, magnetic nanoparticles (MNPs) have been one the most common used class on NPs in biomedical applications, especially in the field of diagnosis and detection of diseases. Diagnosis of diseases are critical to identify the effective treatment, to improve the quality of patient life, and to reduce the cost of treatment.

Cancer is a class of diseases in which a group of cells display uncontrolled growth, invasion, and sometimes metastasis and affect the lives of millions of people worldwide. Methods for the early stage accurate detection of cancer are important and an active area of current research [10]. The diagnoses of tumors and another diseases such as tissue damage, and neurological disorders have been more accurately made with the aid of various imaging techniques such as positron emission tomography (PET) [11], single photon emission computed tomography (SPECT) [12], ultrasound imaging [13], optical imaging [14], magnetic particle imaging (MPI) [15], and magnetic resonance imaging (MRI) [16, 17]. MNPs with narrow size dispersions, intense crystallinity and high biocompatibility have recently come into existence as highly effective contrast agents in imaging techniques [18].

1.1. Magnetic Nanoparticles

MNPs belong to a class of nanomaterial that can be employed under the influence of a magnetic field and their induced magnetic moment is able to be aligned to the direction of the external

magnetic field. Among all MNPs, iron oxides are the most frequently used for biomedical applications [19]. They can be found in different phases in nature such as FeO (wüstite), α-Fe_2O_3 (hematite), γ-Fe_2O_3 (maghemite) and Fe_3O_4 (magnetite). The most common used iron oxide nanoparticles (IONPs) are magnetite and maghemite for biomedical applications. Magnetite has a cubic inverse spinel crystal structure and is a ferromagnetic material. Spinel has the structure AB_2O_4 that A and B exhibit tetrahedral and octahedral cation sites, respectively, and O shows the oxygen anion site [20]. Magnetite contains 56 atoms including 32 oxygen atoms, 16 Fe^{3+} and 8 Fe^{2+} and can be denoted as $(Fe^{3+})_8^{tetr}\ \{Fe^{3+}Fe^{2+}\}_8^{octa}\ O_{32}$ [21, 22]. The cubic spinel structure of magnetite, and one tetrahedron and one octahedron sharing an oxygen atom are shown in Figure 1.1 (a, b), respectively.

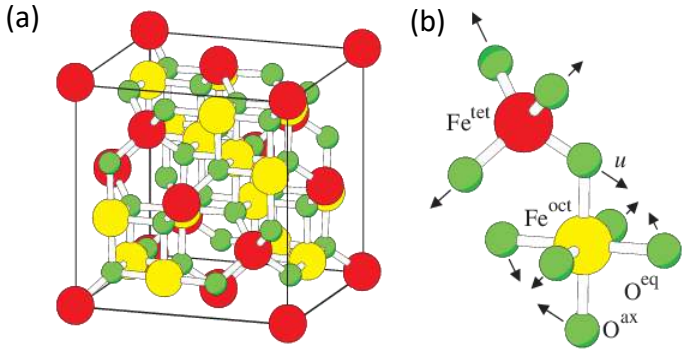

Figure 1. 1 (a) The cubic spinel structure of magnetite, and (b) one tetrahedron and one octahedron sharing an oxygen atom [23].

In magnetite, iron ions (Fe^{2+} and Fe^{3+}) fully occupy the octahedral and tetrahedral sites of the spinel structure. Spins from these two sublattices are antiparallel so the magnetic moments from Fe^{3+} cations cancel each other, and magnetite net magnetization occurs due to Fe^{2+} ions from octahedral sublattice. Magnetite is sensitive to oxidation and by oxidizing is transformed to maghemite. The physical and chemical properties of magnetite such as size, composition, shape and surface chemistry vary widely and influence their biological properties and their clinical applications [24].

1.2. Superparamagnetic Nanoparticles

Generally, superparamagnetism is a phenomenon exhibited by ferromagnetic materials at the nanoscale. The physical and chemical properties of nanomaterials change dramatically compared

to the bulk material due mainly to the size effects and surface phenomena at the nanoscale [25]. Bulk materials consist of multi-domain structures that are responsible for the magnetic properties of the bulk magnet. The movements of the domain walls, that separate multi domains, are the major factor controlling the magnetization reversal in bulk magnets. When the size of magnetic materials diminishes, their structure changes from multi-domain to single-domain and lead to new magnetic properties. In other words, as the size of magnetic material continues to decrease, it becomes more difficult to form domain walls, and below a critical size, which is dependent on the material, the necessary energy to make a domain wall becomes energetically inadequate. So, the particles become single-domain structures. When MNPs with single-domain structure are exposed to an external magnetic field, their magnetic moment will align to the same direction, called easy axis, to minimize the anisotropy energy. The magnetic anisotropy energy is given by the Equation [26]:

$$E = KVsin^2\theta \tag{1-1}$$

Where V is the magnetic core volume, θ is the angle between the magnetic moment and the easy axis, and K is the effective anisotropy coefficient.

The term KV in Eq 1.1 is known as the anisotropy energy barrier. When the volume of the magnetic core continues to decrease, the energy barrier between the two minimum energy directions ($\theta = 0\ or\ \pi$) is diminished and below a critical size, the anisotropy energy barrier can be overtaken by thermal fluctuation energy and the spin will fluctuate spontaneously. In Figure 1.2 the variation of the anisotropy and thermal energies (k_BT) for particles with large and small size are shown.

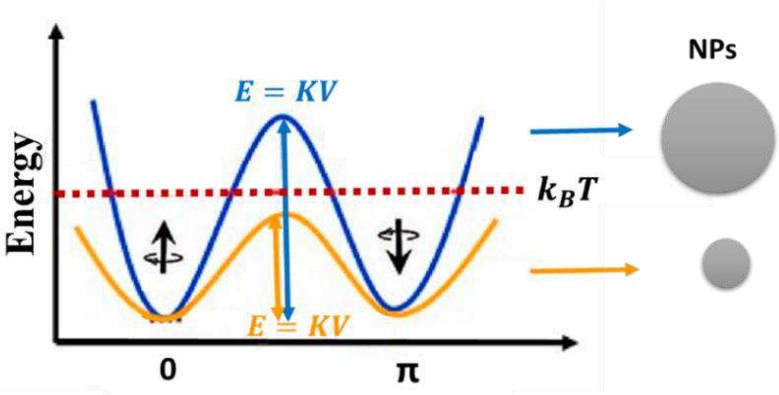

Figure 1. 2 The variation of the anisotropy and thermal energies for particles with large and small size. Modified from Ref. [27].

By applying an external magnetic field, the magnetic moments of the small particles are rapidly reoriented and they behave like paramagnetic but with a high susceptibility and saturation magnetization (M_s) [28]. Such particles are called superparamagnetic. The schematic transition from multi-domain to single-domain and to superparamagnetic state with increasing the particle diameter, and the magnetization curves for ferromagnetic, superparamagnetic and paramagnetic materials, are shown in Figure 1.3 (a, b), respectively. As it observed the superparamagnetic and paramagnetic materials does not display any coercivity (H_c) and remanence (M_r), while ferromagnetic material shows considerable coercivity and remanence which is not desirable for in vivo biomedical applications.

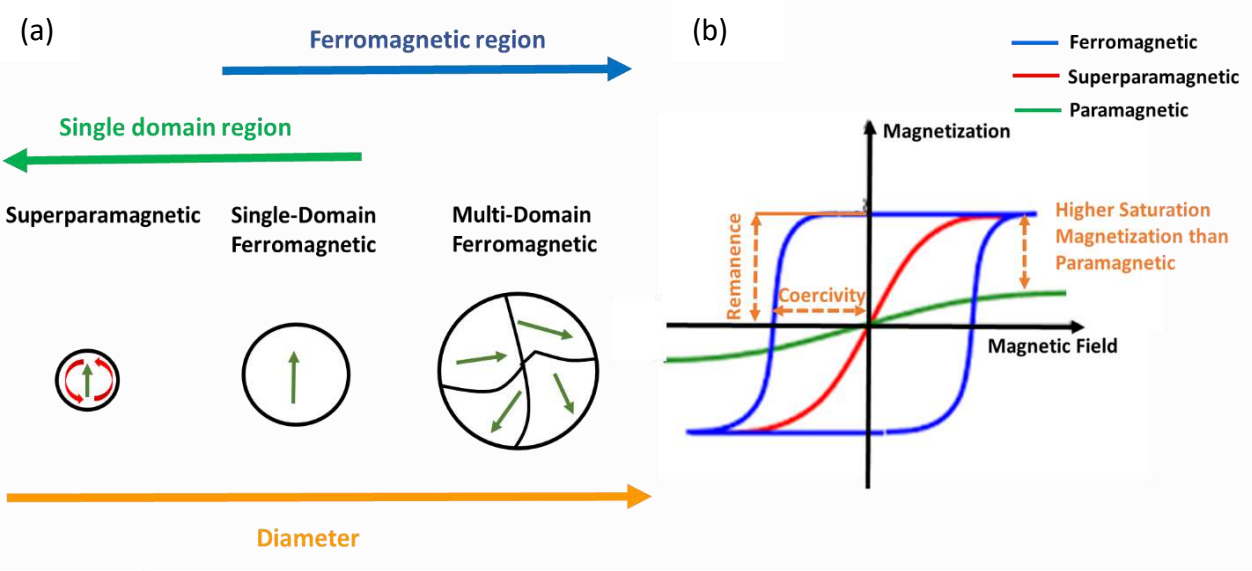

Figure 1. 3 (a) Schematic transition from multi-domain to single-domain and superparamagnetic state with increasing the particle diameter, and (b) the magnetization curves for ferromagnetic, superparamagnetic and paramagnetic materials are illustrated. Modified from Refs [29, 30].

1.3. Synthesis of Superparamagnetic Nanoparticles

There are three significant routes for the synthesis of superparamagnetic nanoparticles using: chemical, physical, and biological methods. These methods have been investigated in order to produce more stable, biocompatible, and shape and size-controlled MNPs [31]. In this thesis two chemical synthesis methods including co-precipitation and thermal decomposition are presented for biomedical applications.

1.3.1. Co-precipitation

The most early and widely used chemical method for synthesis of superparamagnetic iron oxide nanoparticles (SPIONs) is co-precipitation [32-35]. Specifically, ferrous (Fe^{+2}) and ferric salts (Fe^{+3}) in molar ratio 1:2 are co-precipitated under aqueous conditions in a fairly basic solution (NH_4OH or NaOH) at room temperature or under heat to yield either magnetite or maghemite [36-38]. This method is convenient, fast, low cost and can produce large quantities of NPs, however the prepared NPs does not show very narrow size distribution [39]. The particle size, shape, composition and magnetic properties of IONPs depended on the type of salts used (chlorides, sulfates, nitrates, etc.), the Fe^{2+}/Fe^{3+} proportion, the pH value, the reaction temperature, the ionic strength of the media, and the other reaction parameters including stirring rate, and dropping speed of basic solution [31, 40-42]. In this method SPIONs can be coated with surface stabilizers in a one-pot reaction either during or after the synthesis process to increase the stability and biocompatibility and decrease the size distribution of MNPs.

1.3.2 Thermal decomposition

Monodisperse MNPs by thermal decomposition method were introduced by Alivisatos [43] in 1999 and it was further developed by Sun and Park et al [44-46]. Highly monodispersed SPIONs with high crystallinity and shape control can be synthesized using thermal decomposition of organometallic precursors method. Some organic iron compounds (hydroxylamine ferron, iron pentacarbonyl, ferric acetylacetonate, iron oleate) are decomposed at high temperature inside the non-polar boiling solvent with a presence of the capping agent such as oleic acid [47]. Oleic acid acts as both stabilizer and reducing agent [48]. The acquired narrow size distribution of IONPs develops because the nucleation and growth mechanisms occur at different temperatures and can be well-separated. Generally, the nucleation starts around 200 - 240 °C and the growth process take place at relatively higher temperatures around 260 - 290 °C [45]. If the nucleation occurs throughout the growth process, the growth of each particle will differ from another, leading to a broad size distribution.

The reaction parameters such as temperature, concentration, surfactant concentration, refluxing time, seed-mediated growth and heating rate play significant roles in the size and morphology of the NPs [48]. The prepared IONPs are hydrophobic and can be stored in non-polar solvent such as hexane, cyclohexane, toluene, or other solvents.

1.4. Applications of Magnetic Nanoparticles in Biomedicine

MNPs specifically SPIONs, due to their superb properties such as small size, surface chemistry and superparamagnetism can be used in a wide variety of biomedical applications ranging from contrast agents for MRI to the destruction/killing of cancer cells by hyperthermia treatment [49]. In Figure 1.4 some of the biomedical applications of MNPs are shown. In this thesis, only a short review about a few principal imaging techniques such as MRI, MPI and fluorescence spectroscopy will be given.

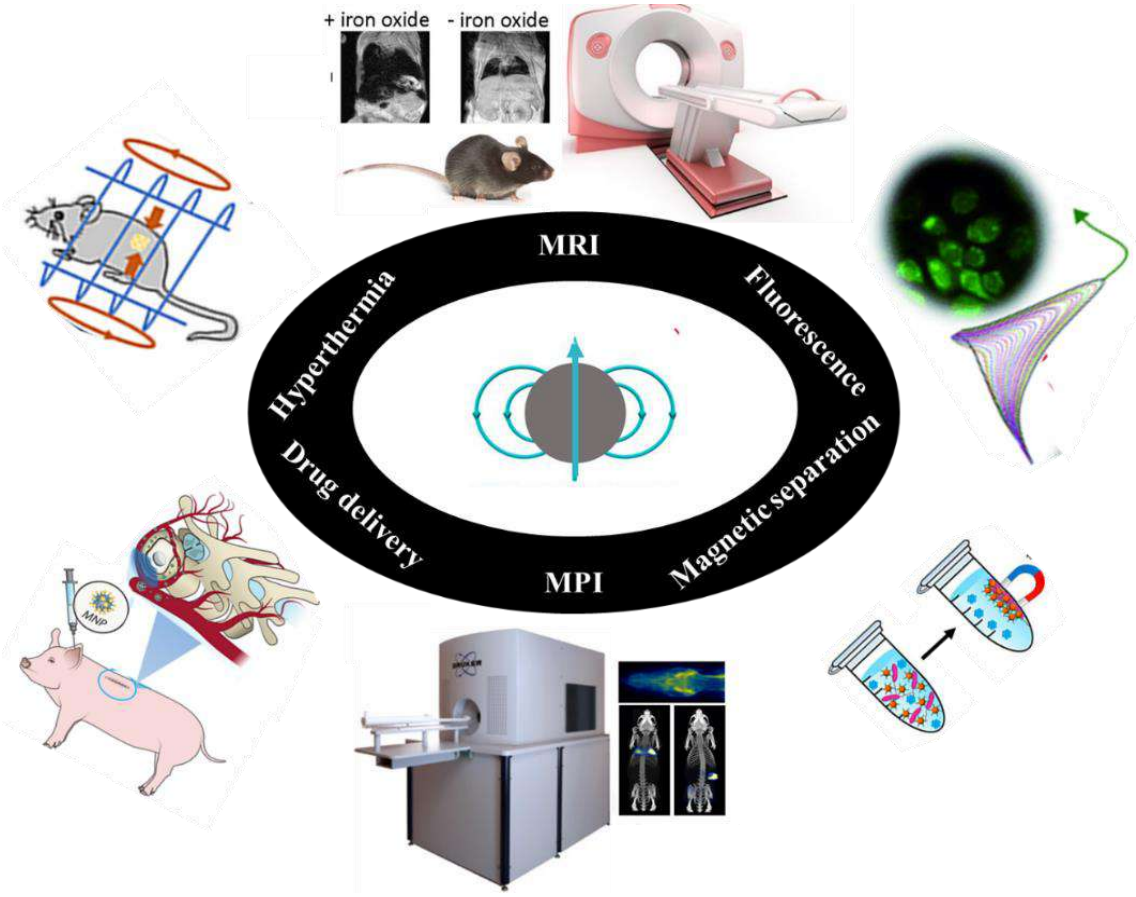

Figure 1. 4 MNPs are the center of several biomedical applications aiming diagnostic imaging based on different physical principles and therapy of a variety of diseases.

1.4.1. Magnetic resonance imaging

MRI currently is the most versatile and informative diagnostic imaging modality in the clinical area due to its superior spatial resolution and contrast in soft tissue without using harmful ionizing

radiations [50, 51]. This imaging is based on the detection of radio frequency (RF) signals, which can interpenetrate the skull and spinal column without deterioration. MRI principle is based on aligning of protons, which are present in the water molecules in the body tissues, in a strong applied magnetic field (B_0) and their precession with the Larmor frequency ($w_0 = \gamma B_0$) that cause the longitudinal magnetization [51]. By applying an RF pulse exactly at Larmor frequency, the spin of protons flip and align antiparallel to B_0. This process leads to a suppression of the longitudinal magnetization and the produce of a transverse magnetization. By removing the RF pulse the excited protons will be relaxed through the recovery of longitudinal magnetization as a result of T1 longitudinal relaxation, there will be also decay of transverse magnetization as a result of T2 transverse relaxation that leads to loss of phase coherence of the precessing protons in the transverse plane.

The resolution of MRI is modified by the contrast agents, which enhance the image contrast by shortening T1 or T2 of water protons. T1 contrast agents cause positive contrast increase to T1-weighted images, while T2 contrast agents provide negative contrast improvement to T2-weighted images. The efficiency of a contrast agent to increase the rate of relaxation is expressed by the relaxivity value of r1 and r2, which is defined as the slope of a plot of 1/T1 (R1) and 1/T2 (R2), respectively, versus concentration in the units of $mM^{-1}\ s^{-1}$. The current MRI contrast agents are commonly Gadolinium-based complexes (GBCA) (paramagnetic species) in the form of T1 positive agents and superparamagnetic nanoparticles as T2 negative agents [10].

1.4.2. Magnetic particle imaging

MPI is a promising new imaging modality for several applications such as vascular and perfusion imaging, cell tracking, oncology imaging, trauma imaging, and inflammation imaging [52]. MPI is a quantitative 3-dimensional (3D) imaging technique that can directly detect IONPs-based tracers without any background signal from surrounding tissues. This system is still in the preclinical stage but it has the potential to be competitive with traditional clinical imaging techniques due to its significant features such as superb contrast, high sensitivity, high resolution imaging and the safety of its tracers [53].

MPI exploits the non-linear magnetization curve of MNP tracers to determine the spatial distribution of tracers. Therefore, a time varying magnetic field (sinusoidal AC drive-field) is applied to the MNPs. The magnetization response, due to their non-linear magnetization curve,

includes the excitation frequency and harmonics of this frequency. A signal that is proportional to the time derivative of the particle magnetization is induced in a nearby receive coil. By Fourier transform the harmonics of the induced signal can be determined [54]. Spatial encoding is provided by superimposing a static magnetic gradient field. This field produce a field free point (FFP), where the magnetic field is zero at a single position, and it magnetically saturates all IONPs outside the FFP. The IONPs in the FFP can freely align with AC field and generate a time-varying magnetization, while IONPs in all other locations inside the field of view (FOV) are saturated and unable to align. Therefore, only the NPs in FFP contribute to the signal [55]. The raw MPI signal is obtained by moving the FFP through the field of view (FOV), and image reconstruction techniques generate a map of the particle distribution [53]. The principle of MPI configuration is illustrated in Figure 1.5.

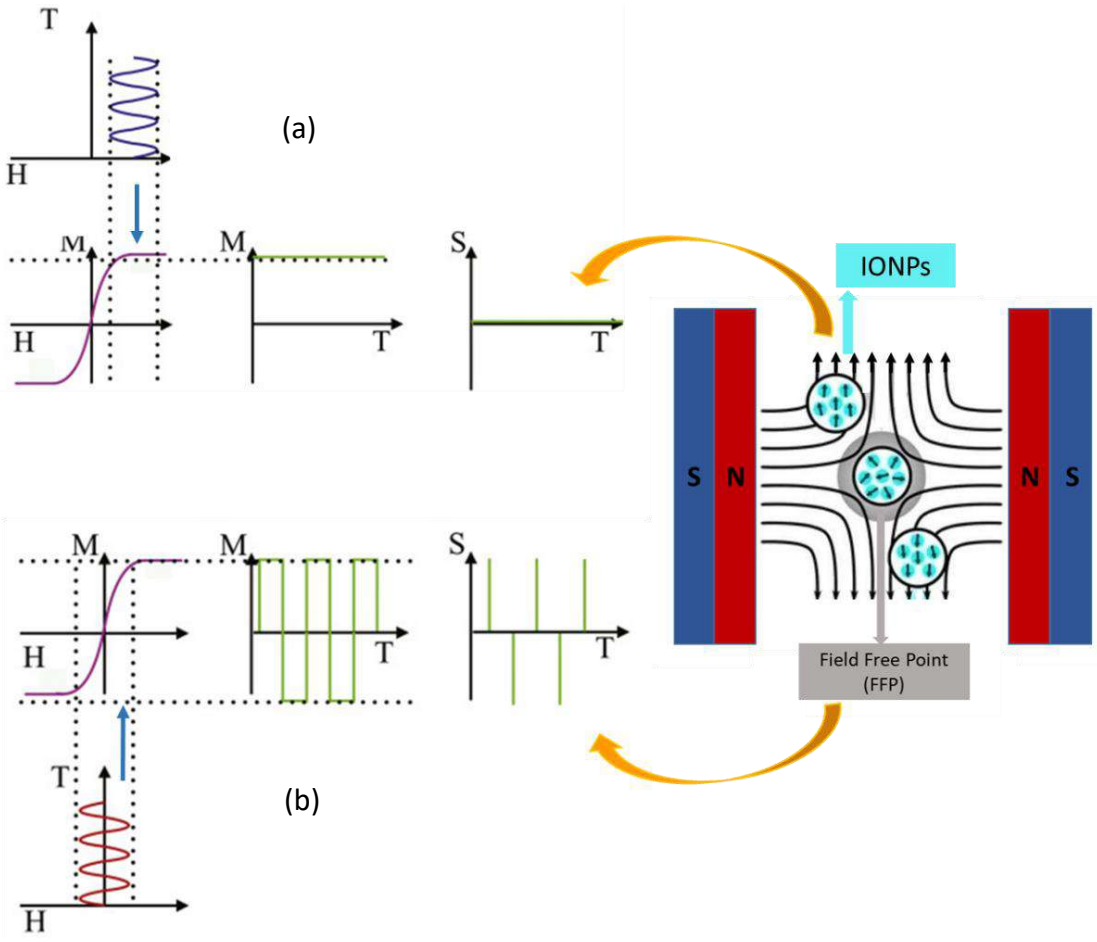

Figure 1. 5 Principle of MPI configuration. (a, b) Showing the signal from the IONPs outside and inside the FFP region, respectively. Modified from Refs [56, 57].

1.4.3. Fluorescence spectroscopy

Luminescence includes several types which can be classified by the energy source which initiates the luminescence process (Figure 1.6). Among them, fluorescence has been widely used in biomedical applications.

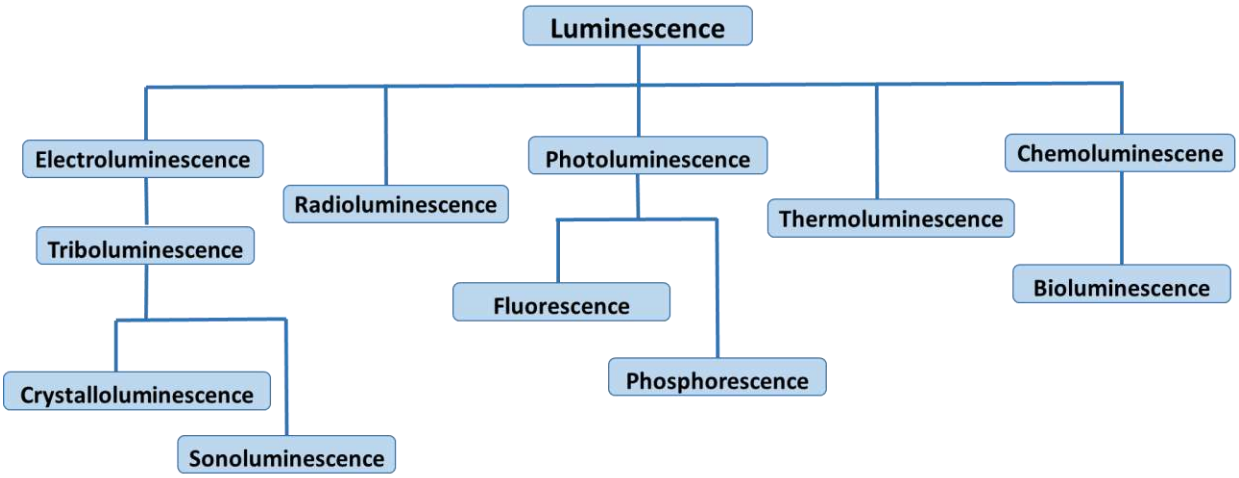

Figure 1. 6 Different types of luminescence which can be classified by the energy source that initiates the luminescence process.

Fluorescence spectroscopy is a promising noninvasive optical diagnostic technique. Over the past few decades, it has gained a considerable attention as a potential imaging technique with rapid diagnosis abilities [58, 59]. The specific focus of its application is early detection and diagnosis of cancer with high sensitivity and specificity due to its response to probe the biochemical changes [60].

Fluorescence relies on photon emission process that happens during molecular relaxation from electronic excited states. It is brought about by absorption of photons in the singlet ground state promoted to a singlet-excited state, that is very fast. After excitation, the molecule is quickly relaxed, in a timescale of femtoseconds to picoseconds, to the lowest vibrational level of the excited electronic state. When the excited molecule from the singlet electronic excited state returns to a vibrational level in the electronic ground state, emits a photon of lower energy, which corresponds to a longer wavelength, than the absorbed photon.

The fluorescence lifetime of a fluorophore is the time which the intensity has decayed by $1/e$ or 36.8% the original value. The decay of the fluorescence intensity as a function of time is described by an exponential function which is given by [61]:

$$I(t) = I_0 e^{-(t/\tau)} \quad (1\text{-}2)$$

Where $I(t)$ is the fluorescence intensity at time t, I_0 is a normalization term (the pre-exponential factor) and τ is the lifetime.

There are various types of fluorescent materials that are used for biomedical applications such as quantum dots, rare earth elements, organic dye molecules, etc. [62-64]. Recently, MNPs with fluorescent properties have been recognized as an emerging class of materials that exhibit great potential in cancer diagnosis [21, 65].

1.5. Objective and Scope of the Thesis

In this PhD thesis we present the work done to synthesize and functionalize superparamagnetic iron oxide nanoparticles (Fe_3O_4) by efficient covering agents to become more suitable for biomedical applications. More specifically, our first aim was devoted to green synthesis of SPIONs, with high magnetization, stability and biocompatibility for biomedical applications. For this synthesis, natural rubber latex (NRL) extracted from *Hevea brasilisensis* was considered as a capping agent to modify the surface of SPIONs. With green synthesis using NRL we could improve the biocompatibility of the MNPs that is essential for *in vivo* biomedical applications. Our second purpose was the synthesis of multifunctional SPIONs with optical properties. As far as both magnetic and optical properties of NPs play significant roles in biomedicine, therefore, we planned to produce small multifunctional NPs with high magnetic, fluorescent and radioluminescent properties, which can be suitable candidate for cancer diagnosis. The multifunctional SPIONs were covered with oleic acid and functionalized with anthracene, an organic molecule. Additionally, another aim of this project was to narrow the size distribution of SPIONs dispersed in water using a new, efficient and controllable magnetic separation method by low gradient magnetic field (<15 T/m) to improve their biomedical applications, specifically as tracers in MPI.

1.6. Thesis Outline

This thesis basically consists of four original articles that have been published/submitted. In this sense Chapter 2 to 5 can be considered as self-consistent unities containing introduction, materials and methods and results. The thesis is organized as follow.

Chapter 2 presents the green synthesis and surface modification of SPIONs with enhanced magnetization using natural rubber latex. This work was published in the Journal of ACS Sustainable Chemistry & Engineering.

Chapter 3 presents the results of magnetic (Fe_3O_4) nanoparticles coated by natural rubber latex as MRI contrast agent. This work was published in the Journal of Magnetism and Magnetic Materials (JMMM).

Chapter 4 presents the synthesis of radioluminescent iron oxide nanoparticles functionalized by anthracene for biomedical applications. This work was published in the Journal of Colloids and Surfaces A: Physicochemical and Engineering Aspects.

Chapter 5 presents the magnetic separation of iron oxide nanoparticles to improve their applications as tracers for MPI. This work was accepted in the Journal of Physics in Medicine & Biology.

Chapter 6 is a general conclusion of this thesis and suggestions for future works.

Chapter 2: Green Synthesis and Surface Modification of Iron Oxide Nanoparticles with Enhanced Magnetization Using Natural Rubber Latex

2.1. Introduction

Magnetic nanoparticles (MNPs) have demonstrated great promise, not only for recording technologies, but also for biological and medical applications such as protein purification, bacterial detection, magnetic resonance imaging (MRI), drug delivery, magnetic particle imaging (MPI) and hyperthermia [25, 66-70]. Iron oxide nanoparticles (IONPs), like magnetite (Fe_3O_4), are commonly used for these purposes and several chemical methods can be used to synthesize these MNPs, such as microemulsions [71], sol-gel synthesis [72], thermal decomposition [45], flow injection synthesis [73], and co-precipitation [74]. The co-precipitation technique is the simplest and most efficient chemical pathway to obtain magnetic particles. The main advantage of the co-precipitation process is that a large amount of nanoparticles can be synthesized [75].

Magnetic properties of nanoparticles are strongly dependent on their composition, morphology, particle size, size distribution, and degree of crystallinity [76]. The preferred core size of the nanoparticles in most medical applications is typically less than 50 nm. Usually, nanoparticles in this size range become a single magnetic domain and when the temperature is above a certain value, called the blocking temperature, they show superparamagnetic behavior [77]. Nanoparticles in the superparamagnetic state have large magnetic moments, because all their magnetic moments will be aligned in the same direction, so that when an external magnetic field is applied the resulting magnetization is the maximum possible for that specific material and size. These features make superparamagnetic nanoparticles very attractive for biomedical applications.

Much research has been done to prepare superparamagnetic nanoparticles with high functionality. Usually, MNPs tend to aggregate because of their large surface area/volume ratio and also due to

interparticle interactions. Functionalization of the MNPs is crucial for biological applications in order to improve their stability and biocompatibility [78]. Several coating materials have been used to modify the surface chemistry of nanoparticles and improve their stability, including organic surfactants, inorganic metals, inorganic oxides, bioactive molecules and structures, and organic polymers [79-81]. Currently, the most commonly used materials are organic polymers. With polymeric coating of the MNPs several functional groups from the polymer could be used for further functionalization potentially increasing drug transport and release during its biodegradation [82, 83]. Furthermore, most of the organic polymers are non-toxic and biocompatible, including dextran [84], chitosan [85], and plant extracts obtained from *Syzygium cumini, Bauhinia variegata, Cedrus deodara, Eleaocarpus sphaericus* and *Hevea brasiliensis* [86, 87]. Therefore, these types of materials have good potential as coating agents in biological applications.

Natural rubber latex (NRL), extracted from *Hevea brasiliensis*, was used for synthesis of silver nanoparticles [87]. This plant extract acts both as a reducing and capping agent. It is a naturally occurring form of cis-1,4polyisoprene and by weight consists of about 45% rubber, 50% water, and 5% other constituents such as protein, lipids, and carbohydrates [88]. The rubber particle consists of one v-terminal, two trans-1, 4 isoprene units, a long chain of cis-1, 4 isoprene repeating units, and ends in an a-terminal. The NR latex particle is essentially core-shell in structure with polyisoprene as the core, surrounded by a shell of non-rubber components (such as proteins and lipids). The proteins and phospholipids surrounding the rubber particle surface play an essential role in stabilizing the latex particles [89].

NRL has been widely used in the manufacturing of tires, balloons, airships and surgical gloves [90]. In addition, it has biomedical applications, such as drug delivery in guided bone regeneration [91, 92], as a biomaterial in vascular prosthesis fabrication [93], as a biomembrane for angiogenic processes [94], as a membrane for the controlled delivery of nanomaterials [95] and in folk medicine [96].

In the present study, superparamagnetic nanoparticles were synthesized using a green co-precipitation method with different concentrations of NRL. This process occurs at a mild temperature (90 ^{o}C) and is fast, eco-friendly and cost-effective. Prepared MNPs were characterized by various techniques. The functionalized surface of MNPs was studied by FTIR. Also, the magnetic properties of bare MNPs and NRL-coated MNPs were investigated by Hall

magnetometry. NRL-coated MNPs are very stable at room temperature and can be stored in liquid and powder forms for a few months or even used as a magnetic rubber film/membrane.

2.2. Materials and Methods

2.2.1. Preparation of magnetic Fe_3O_4 nanoparticles

MNPs were prepared by co-precipitation of ferric and ferrous salts. Briefly, 6.758 g of $FeCl_3.6H_2O$ was dissolved in 25 ml distilled water. Then, 3.97 g of $FeCl_2.4H_2O$ was dissolved in a 10 mL aqueous solution of hydrochloric acid (5.45 M). In a separate beaker, a 1.28 M NH_4OH aqueous solution was heated at 90 ^oC for a few min. Next, a mixture of iron **(**III**)** chloride (4 ml) and iron (II) chloride (1 ml) was added to this basic solution with vigorous stirring. The color of the solution changed instantly to black indicating the formation of MNPs. The prepared MNPs were kept in an ultrasonic bath for one hour to prevent agglomeration. The final product was precipitated using permanent magnet and rinsed with Milli-Q^{TM} water until the solution was a neutral pH. Finally, Fe_3O_4 was dried in an oven at 32 ^oC, yielding a black powder (Figure 2.1(a)).

2.2.2. Preparation of magnetic NRL-Fe_3O_4 nanoparticles

Magnetic NRL-Fe_3O_4 nanoparticles were obtained by a method similar to that of the uncoated MNPs. In this synthesis, an NRL solution (100 µL to 800 µL) was added to the NH_4OH (1.28 M) aqueous solution. After vigorous stirring for 3 minutes, the solution was heated in a water bath (90 ^oC) for 10 minutes. Then the mixed solution of ferric and ferrous chloride was added to the NRL solution under vigorous stirring. A black precipitate formed immediately. The solution was kept in an ultrasonic bath for one hour to avoid agglomeration. The samples were named according to the volume of NRL added during the synthesis. For example, the sample prepared with 100 µL of NRL was named NRL-100 and so on, up to the sample NRL-800.

It is worth noting that MNPs with NRL volumes such as 1600 µL were also synthesized but, because of the high concentration of NRL, we observed polymerization after adding iron salts. Therefore, maximum NRL volume should be limited to 800 µL for this amount of iron salts.

2.2.3. Purification of magnetic NRL-Fe_3O_4 nanoparticles

Prepared MNPs were washed with Milli-Q^{TM} water (using permanent magnet) several times until a neutral pH was achieved. The final samples were dried at 32 ^oC. After drying, powders were

obtained for the samples, both uncoated-MNPs and NRL-100, and rubbery films for samples NRL-400 and NRL-800. The images of prepared samples are shown in Figure 2.1(a- d).

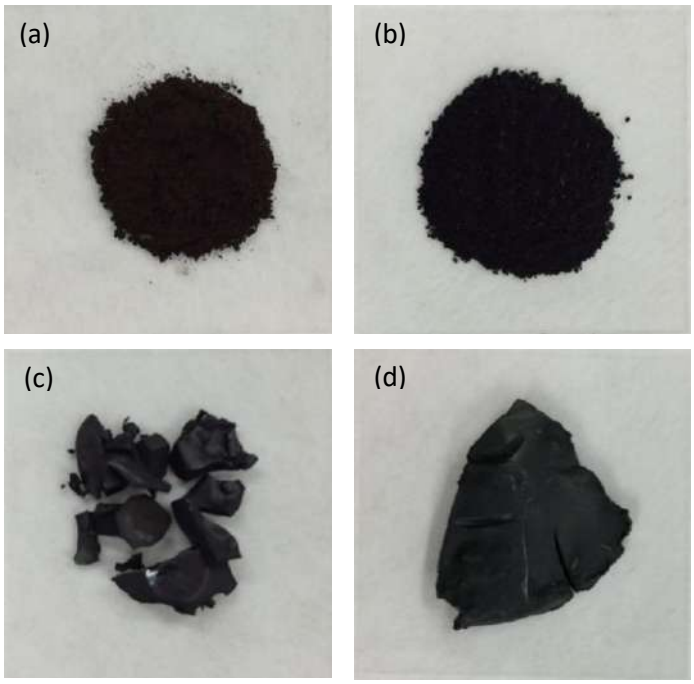

Figure 2. 1 Images of dried samples: (a) bare MNPs, (b) NRL-100, (c) NRL-400, and (d) NRL-800 MNPs.

Because of the high content of latex in NRL-400 and NRL-800 samples, as evidenced by Figure 2.1, it was important to estimate the percentage of iron oxide and rubber in each sample. By drying 1 mL of latex solution we estimated that each milliliter of latex solution contains 0.49 g of solid rubber. Then, we calculated the mass of latex in each sample by measuring the total mass of bare-MNPs, NRL-100, NRL-400, and NRL-800. Thereafter, we calculated the NRL mass percentage in each sample by considering the total mass of each sample and their respective mass of latex. We obtained a mass percentage of rubber of 9.2%, 29.9% and 41% for NRL-100, NRL-400, and NRL-800, respectively. To calculate the mass of iron oxide produced, after washing the samples three times we subtracted the remaining mass of latex/rubber from the total mass of each sample. The mass of iron oxide in the sample NRL-100, NRL-400, and NRL-800 was calculated as 0.42, 0.4 and 0.48 g, respectively.

In order to confirm the aforementioned method to calculate the mass percentages of NRL and Fe_3O_4 in each sample, the amount of iron was also estimated by phenanthroline spectrophotometric iron quantification assay, using 100 µL of the NRL-400 sample. By this assay, the molecular weight of iron was determined as 0.627 mg and by our method (subtracting the mass of latex) we estimated 0.683 mg. Therefore, the results are similar, with only 8% of difference, what is acceptable for a fast determination of the concentration.

2.2.4. Characterization of magnetic Fe_3O_4 and NRL- Fe_3O_4 nanoparticles

The prepared MNPs were characterized by different methods. The morphology and size of the MNPs were investigated by transmission electron microscopy (TEM; JEOL-JEM-100 CXII), by drying a drop of the washed colloidal dispersion onto a copper grid covered with a conductive polymer. The TEM size of MNPs were measured by ImageJ software (around 40 nanoparticles per sample). Origin software was employed to plot the histograms of TEM images. The hydrodynamic diameter and zeta potential of the nanoparticles suspensions were determined by dynamic light scattering (DLS) using a Zeta-Sizer system (Malvern Instruments). The data was collected at a fixed angle (90º) and fixed wavelength (633 nm He–Ne laser). The crystalline properties and phase identification were acquired by XRD (D5005 Diffractometer, Bruker) analysis, using x-ray beam nickel-filtered copper K radiation (λ=1.5406 Å) in the range $10º<2\theta º<70º$. The surface functionalization was characterized by FTIR (Shimadzu IRPrestige-21) in the region between 4000 and 400 cm^{-1} for powder samples (uncoated and 100-NRL MNPs) and MIRacle^{TM} single reflection (ATR-PIKE Technologies) in the region 4000 and 600 cm^{-1} for the magnetic rubber films (400-NRL and 800-NRL samples). The magnetic properties of the MNPs were measured by a custom-made Hall effect magnetometer [97]. The measurements were taken at room temperature (25 ºC) and using applied magnetic fields in the range −2.0 to +2.0 T. The samples had a total weight of about 15 mg, but the magnetization curves were normalized by the mass of iron oxide, i.e., the mass of the latex was subtracted from the total mass of each sample.

2.3. Results and Discussions

The hydrodynamic size of the MNPs was estimated by Dynamic Light Scattering (DLS). DLS measurements of bare MNPs and NRL-coated MNPs are shown in Figure 2.2 (a-d) after washing them with Milli-Q^{TM} water 3 and 10 times. The hydrodynamic sizes after 3 washings for bare MNP, NRL-100, NRL-400 and NRL-800 are 80, 108, 142 and 164 nm, respectively. We also

observed that the hydrodynamic size of MNPs decreases as a function of the number of washings, probably due to removal of weakly bound NRL molecules from the latex shell. After 10 washings, for instance, hydrodynamic sizes decrease to 65, 71, 73 and 78 nm for bare MNP, NRL-100, NRL-400 and NRL-800, respectively. The hydrodynamic sizes of NRL-coated MNPs are larger than the uncoated MNPs, indicating the coating of MNPs by NRL molecules (Figure 2.2). Furthermore, the hydrodynamic size of the particles increases when increasing the amount of NRL, probably due to the big size of rubber molecules [98], suggesting that thicker NRL layers are deposited upon increasing NRL concentration.

The hydrodynamic size and polydispersity index (PDI) of MNPs decrease after 10 washing procedures (Table 2.1), indicating improved monodispersity of NRL-MNPs in solution. The hydrodynamic size of NRL-400 and NRL-800 decrease significantly compared to the bare MNPs and NRL-100 MNPs, probably due to removal of weakly adsorbed latex molecules in the outer NRL shells. This result suggest that the prepared NRL coated MNPs have core-shell structure and shell-thicknesses can be controlled by both NRL concentration and the number of washings. Above 10 times washing, hydrodynamic size did not change, suggesting strong bonding between the NRL molecules (in the inner latex shells) and the MNPs.

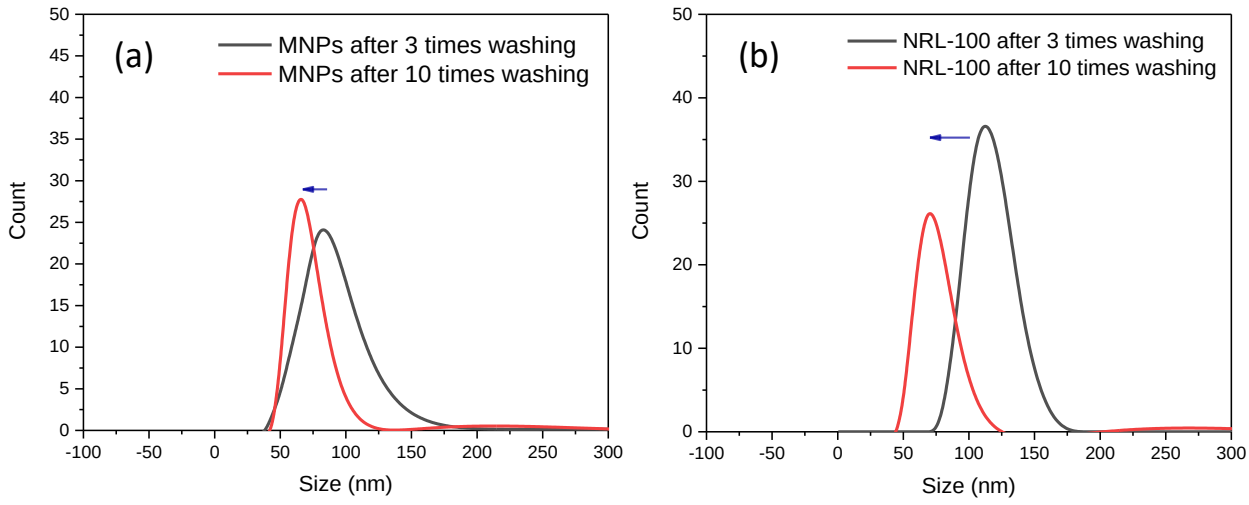

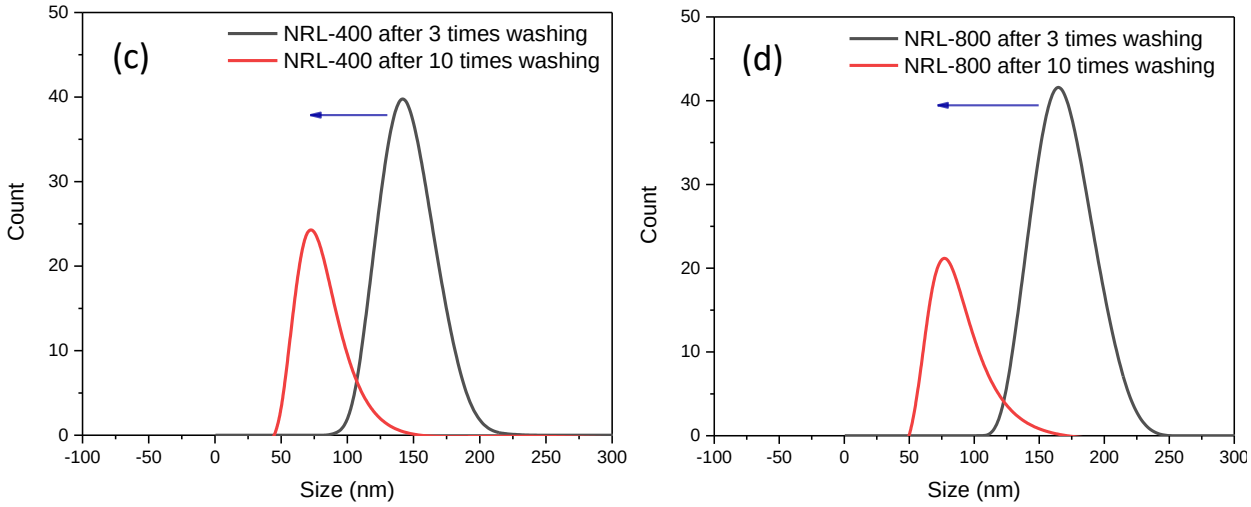

Figure 2. 2 Particle size distribution of MNPs obtained by the DLS technique, for (a) bare MNPs, (b) NRL-100, (c) NRL-400, and (d) NRL-800 MNPs.

Figure 2.3 shows TEM images and histograms of the size distributions of bare MNPs and NRL-coated MNPs. The nanoparticles have a spherical shape for all samples. The average core sizes are estimated to be 12±4, 13±2.8, 10.3±2.2 and 7.9±1.5 nm for bare MNPs, NRL-100, NRL-400 and NRL-800 MNPs, respectively.

The size distribution and average size of MNPs are influenced by the amount of NRL. Increasing the NRL concentration decreased the particle size. This is probably because, upon increasing the concentration of NRL, which is the capping/ligand agent, more NRL molecules can attach to the surface of the nanoparticles, preventing agglomeration and decreasing their growth. Therefore, increasing the NRL concentration decreases the iron oxide core size and leads to a more homogeneous particle size distribution. These results are in agreement with reference [99], where chitosan was used as the capping agent and the particles became smaller with increasing chitosan/Fe mass ratios.

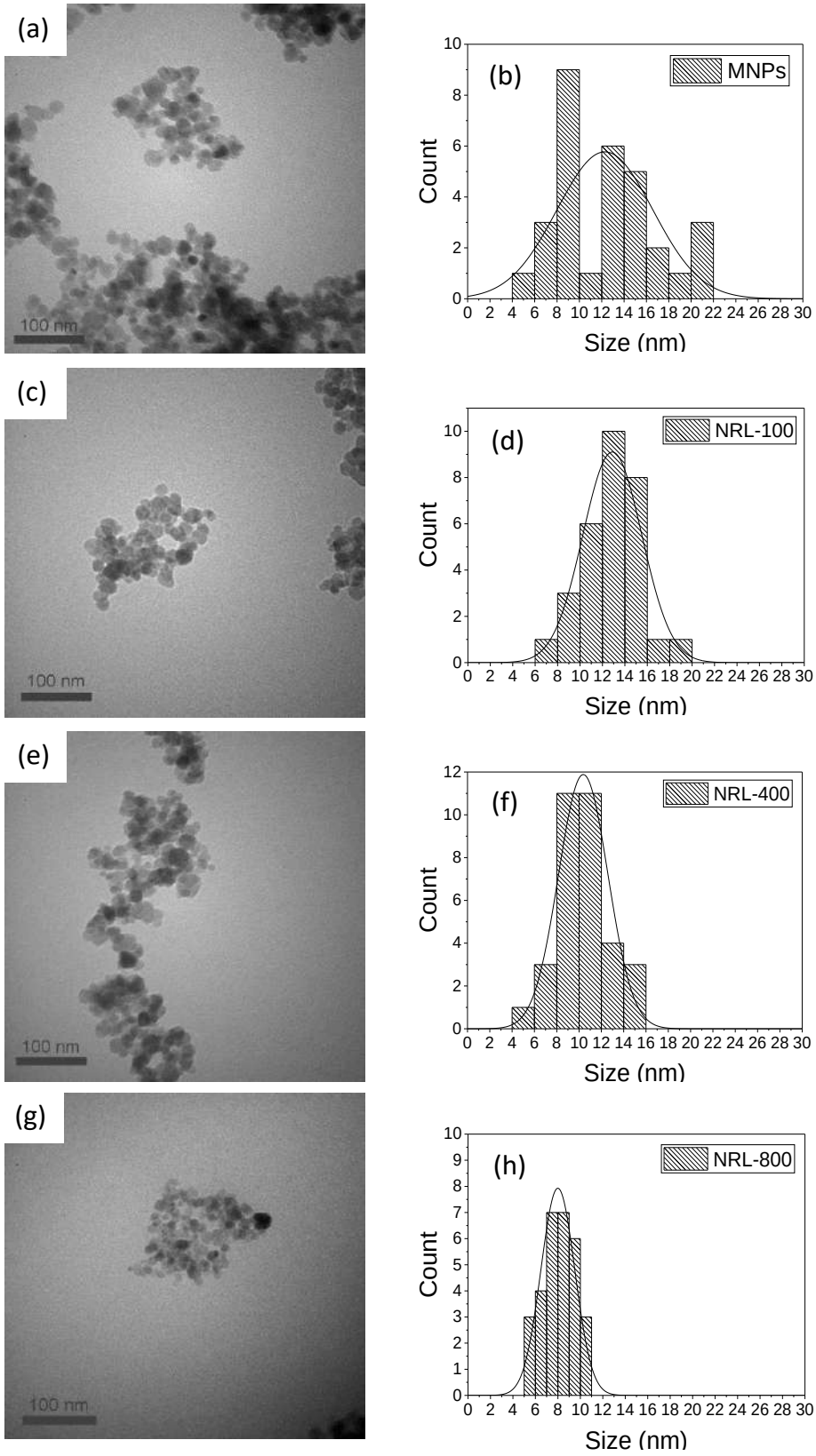

Figure 2. 3 TEM images and histograms of the particle size distribution of bare MNPs (a-b), NRL-100 (c-d), NRL-400 (e-f), and NRL-800 (g-h).

One important question at this point is why the nanoparticle diameters measured by DLS and TEM do not agree and why the nanoparticles observed by TEM images are not well dispersed in the grid. One possible explanation for the observed size difference is that DLS measures hydrodynamic size, which encompasses core size plus shell thickness, while TEM will see only the iron oxide core due to the low electronic density of the NRL molecules. According to the literature, the rubber particles have diameter above 15 nm [98]. Therefore, the larger sizes pointed by DLS may be caused by the presence of a thick rubber shell. This hypothesis is reinforced by the observation that increased number of washing decreases the hydrodynamic size of the nanoparticles, as discussed above.

This, however, does not explain why nanoparticles are not well dispersed in the TEM grid, and why we could not observe the NRL shell around the NRL-MNPs. The absence of a NRL shell in TEM images could be due to elastic and electronic properties of NRL. Most of stabilizing agents used for nanoparticle preparation consist of organic molecules, but few/none of the reported ligands present elastic/rubber properties. It should also be mentioned that nanomaterials are usually expelled from polymeric matrices, and this expulsion depends on nanoparticle size and concentration [100-102]. Polymer matrices are usually able to accommodate only a small percentage of nanoparticles, leading to segregation when using high nanoparticle concentration [100]. In this sense, the absence of the NRL shell in TEM images may be consequence of the expulsion of the MNPs from the latex matrix, during the rubber polymerization caused by the drying procedure in the TEM grid. Furthermore, DLS results reveal that while in solution (before drying/polymerization) hydrodynamic size decreases by washing the NPs, probably due to removal of weakly bound NRL molecules, i.e., non-polymerized rubber molecules. Therefore, we attribute the larger size pointed by DLS - compared to TEM - as consequence of the total hydrodynamic size (core + shell) because the NRL-MNPs are still in solution (non-polymerized NRL), whereas the low dispersity of nanoparticles observed in TEM is due to the expulsion of the nanoparticles from the latex matrix during drying and polymerization.

It should also be emphasized that the low atomic number of the rubber leads to low contrast image, hindering observation of the NRL shell. In fact, NRL was not observed in any region of the TEM grid, reinforcing this hypothesis. Taken together, these two hypothesis may explain the non-

observation of the NRL shell in the TEM images. Table 2.1 summarizes the sizes of the MNPs as measured by TEM and DLS, along with the polydispersity index (PDI).

Table 2. 1 Size of magnetic nanoparticles obtained by TEM and DLS technique.

Samples	NRL (µL)	TEM size (nm)	DLS size after 3x washing (nm)	PDI	DLS size after 10x washing (nm)	PDI	Zeta potential (mV)
Uncoated-MNPs	0	12±4	80	0.37	65	0.37	-4.4
NRL-100	100	13±2.8	108	0.49	71	0.39	+32.2
NRL-400	400	10.3±2.2	142	0.51	73	0.38	+33.4
NRL-800	800	7.9±1.5	164	0.57	78	0.36	+32.0

Since the stability of MNPs is very important for biomedical applications [103], the surface charge of prepared samples was measured by zeta potential analysis. The zeta potentials of bare MNPs and NRL-coated MNPs suspensions are shown in Figure 2.4. The zeta potential of bare MNPs was -4.4 mV, whereas the values for NRL-100, NRL-400 and NRL-800 are +32.2, +33.4 and +32 mV, respectively. From the literature, nanoparticle suspensions become stable when the zeta potential value is greater than ± 30 mV [104, 105]. Based on that, we conclude that the NRL-coated MNP suspensions are more stable than the bare MNP suspensions.

The surface surrounding the rubber particles contains both positive and negative charges. The negative charges are attributed to ionization of adsorbed carboxyl groups on phospholipid molecules, and the positive charges are generated from specific amino groups of the adsorbed proteins [106]. Earlier reports showed that the zeta potential of the latex (obtained from *Hevea brasiliensis)* exhibited the negative value in pH range from 4 to 12 [96]. However, it has been shown that the rubber latex can be used for metal ion adsorption and has the ability to adsorb various divalent cations [107] and, in addition, this matrix has the ability to ion-exchange (IEX) with both cations and anions [108]. In our studies, the rubber latex (NRL-MNPs) particles can adsorb both divalent cations such as Fe^{2+} ions as well as other monovalent cations such as NH_4^+ and H^+ [109]. Upon adsorption of these cations, the negatively charged surface of the latex (NRL-MNPs) particles would first neutralize and then become positive. In other words, cations such as NH_4^+ and H^+ adsorbed on the latex surface may change the net surface charge to positive.

Therefore, the adsorption of these cations by the rubber latex results the positive zeta potential of the NRL coated MNPs.

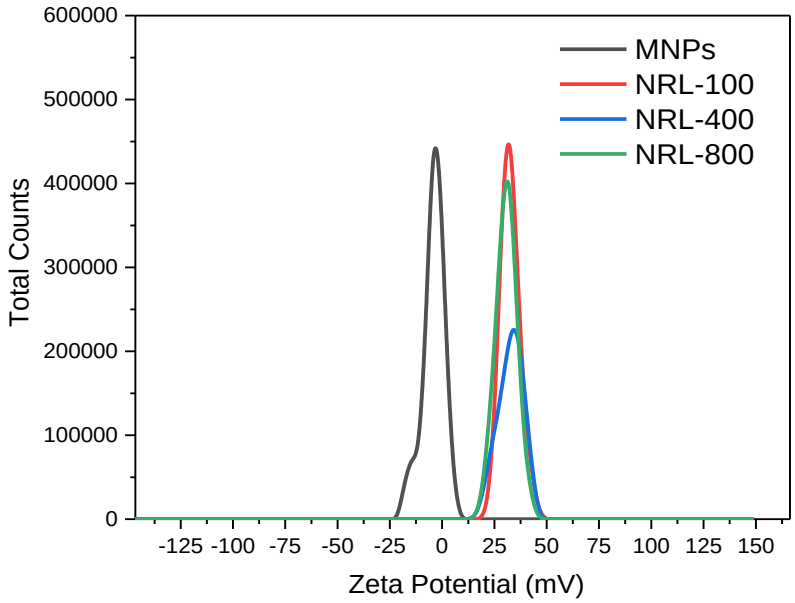

Figure 2. 4 Zeta potential of bare MNPs and NRL- coated MNPs.

X-ray diffraction (XRD) was used to analyze the crystallographic structure of the uncoated and NRL-coated MNPs, (Figure 2.5). A series of characteristic peaks were observed for Fe_3O_4 (2θ = 30.1, 35.5, 43.1, 53.6, 57.0 and 62.6^o) relative to the (2 2 0), (3 1 1), (4 0 0), (4 2 2), (5 1 1), and (4 4 0) planes, respectively, indicating that the functionalization does not degrade the core magnetite. These peaks showed that the nanoparticles were pure magnetite (Fe_3O_4) with a spinel structure (JCPDS card no. 85-1436) [110]. The crystallite size of the nanoparticles was calculated from the main peak (3 1 1) using Scherrer's equation. The calculated crystal sizes were 9, 10, 8.3 and 11 nm for samples of bare MNPs, NRL-100, NRL-400, and NRL-800, respectively.

The crystal sizes calculated here are in good agreement with the average sizes obtained from TEM images, indicating that the particles are composed of single crystals. It is worth noting that for the NRL-800 sample, the high concentration of latex gives rise to a rubber film instead of powder (Figure 2.1d). Therefore, the intensity of the XRD peaks decreases due to the high percentage of amorphous rubber surrounding the MNPs and lower percentage of MNPs - $\approx$ 41% of the total mass in sample NRL-800 is latex - leading to less intense XRD peaks and, consequently, less

accurate particle size calculation (total sample mass was the same for all XRD analyses). The crystallinity of samples cannot be verified and compared here, due to the high percentage of latex in NRL-400 and NRL-800 samples, and the consequent lower XRD intensities.

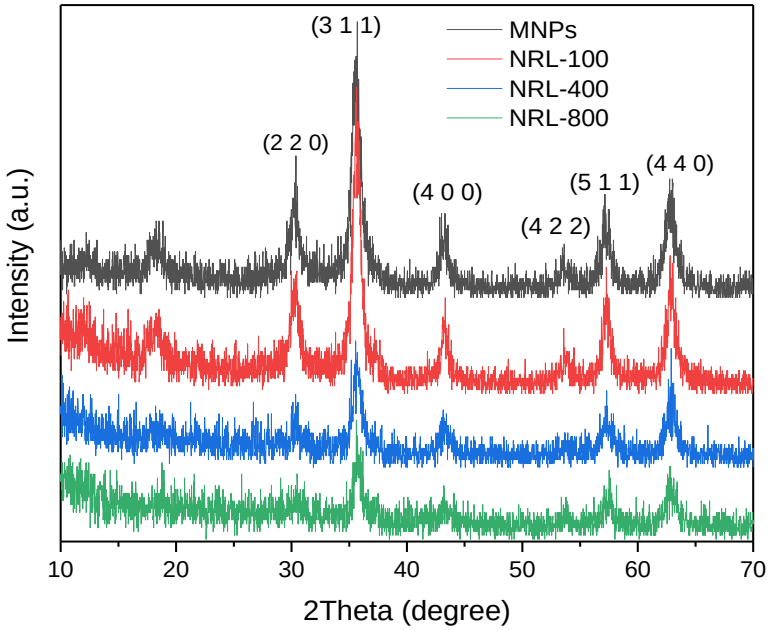

Figure 2. 5 XRD patterns of MNPs uncoated and NRL-coated with different concentrations.

FTIR spectroscopy confirmed the binding of the magnetite surface with NRL molecules. Figure 2.6 shows infrared spectra of bare MNPs, NRL-coated MNPs, and pure NRL. Compared to bare MNPs, several additional peaks could be observed for the NRL-coated MNPs, further suggesting the successful coating of the iron oxide surface with NRL molecules. The spectra of bare MNPs and NRL-100 MNPs have an intense band at 573 cm^{-1}, ascribed to the stretching vibration mode of the Fe-O bond in the crystalline lattice of magnetite (Fe_3O_4) [111].

A broad band centered at 3414 cm^{-1} and a band at 1634 cm^{-1} attributed to OH-stretching and OH-bending, respectively, are observed only in the spectrum of the bare MNPs. These hydroxyl groups are probably adsorbed on the nanoparticle surface, due to residual water in the dried MNPs. Removal of residual water in oxides usually requires annealing for long times at high temperatures. In the case of ZnO nanoparticles, for instance, the minimum required temperature is 150° C, but temperatures as high as 300° C can be used [112-114]. However, magnetite is unstable at high

temperatures and magnetic and structural phase transitions occur above 250° C [115, 116]. So, annealing is unlikely to be successful in removing the OH band of the surface of MNPs while maintaining the magnetite phase. The absence of -OH vibration bands for NRL-coated MNPs may suggest that surface hydroxyls (probably due to hydrated nanoparticles), are replaced by NRL molecules and treatment to remove residual water is no longer necessary. In other words, the binding of the MNPs to NRL molecules protects the magnetic cores from water, preventing hydration of the nanoparticle surface. This is a very important feature for biomedical applications, because these MNPs will be constantly exposed to biological fluids that might alter their properties.

The various absorption bands observed in the pure NRL spectrum are identical to the ones observed for the cis-1,4-polyisoprene references [117], confirming that the major constituent of latex is the cis isomer of polyisoprene. The main vibration bands of pure NRL are associated with C–H stretching at 2960 and 834 cm^{-1}, the symmetric and asymmetric stretching of the CH_3 group at 2918 and 2854 cm^{-1}, and the symmetric and asymmetric bending of the same group in the region of 1447 and 1376 cm^{-1} [118]. In Figure 2.6, the band of the NRL spectrum at 834 cm^{-1}, attributed to C-H groups, slightly shifts to 831, 838 and 842 cm^{-1} for NRL-100, NRL-400 and NRL-800, respectively. Also, when the amount of NRL is increased, the intensity of bands in the region of 2960, 2918, 2854 cm^{-1} increases, due to the higher NRL concentration. The existence of C-H groups and the changing of the intensity and position of these bands in all NRL-MNPs spectra suggest the functionalization of the magnetic nanoparticles (Fe_3O_4) with latex cis-1,4-polyisoprene.

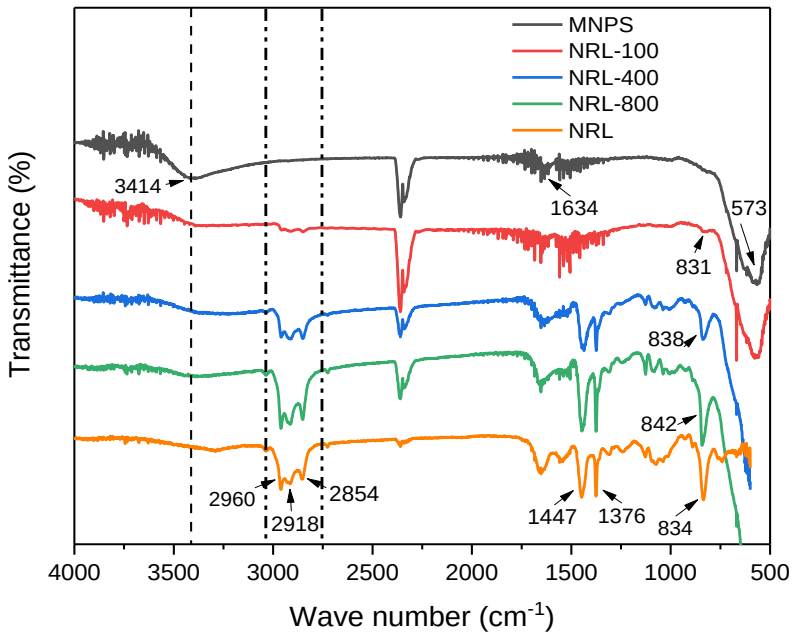

Figure 2. 6 FTIR spectra of bare MNPs, NRL-coated MNPs and pure NRL.

In order to study the magnetic behavior of Fe_3O_4 nanoparticles, magnetization measurements were recorded with a custom-made Hall effect magnetometer at room temperature. The magnetization curves were plotted twice, with and without considering the mass of NRL. The magnetization curves for uncoated MNPs and NRL-coated MNPs, considering the total mass of each sample (iron oxide + NRL) are presented in Figure 2.7. All measurements were performed at fields from -2.0 to +2.0 T. The magnetization from 1.5 T to 2.0 T varies by less than 0.3%. We then estimated the saturation magnetization at 2.0 T.

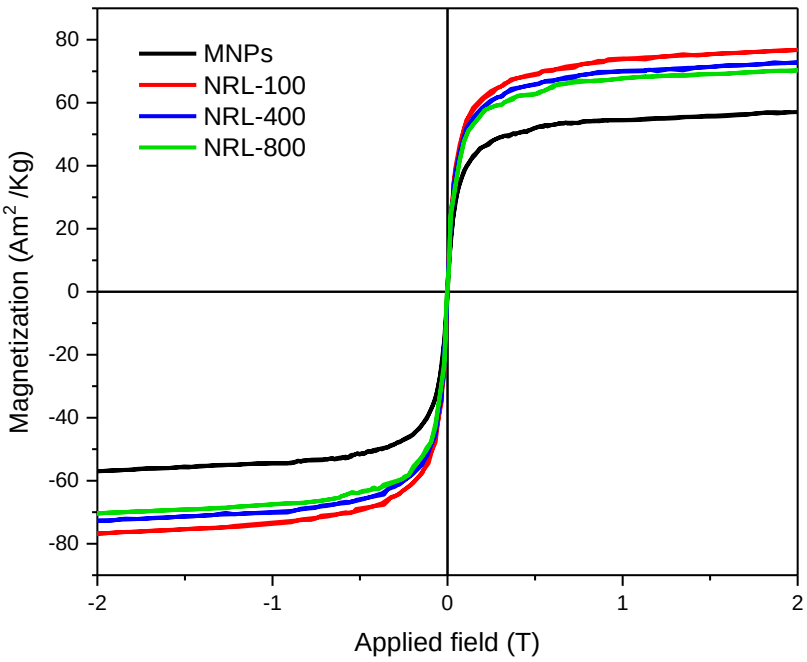

Figure 2. 7 Magnetization curves of bare MNPs and NRL-coated MNPs measured by Hall magnetometer considering the total mass of each sample.

The hysteresis curves of all the samples do not display coercivity or remanence which indicates that they are superparamagnetic [77]. This is because the MNPs are smaller than 20 nm and are likely to have a single magnetic domain [119]. The saturated magnetic intensity for uncoated MNPs was 57 Am^2/kg, and the saturation magnetization values for samples NRL-100, NRL-400, and NRL-800 were 77, 73, and 70 Am^2/kg, respectively. The magnetization of all the NRL-coated MNPs is higher than the magnetization of bare magnetic nanoparticles. According to the literature, some surface ligands may decrease the interparticle interactions, which reduces the disorder of the surface spins and thereby increases the magnetization of MNPs. For instance, this effect has been observed for MNPs coated with fucan polysaccharides [79]. However, the improved MNPs of NRL-coated MNPs are more likely attributed to the elimination of residual water upon binding of the NRL molecules onto the MNPs surface, as supported by the FTIR spectra. As previously discussed, the presence of hydroxyl groups (OH-stretching and OH-bending) is observed only in uncoated MNPs, leading to worse crystal quality and consequently lower magnetization.

Figure 2.8 shows the magnetization curves for uncoated MNPs and NRL-coated MNPs considering only the mass of iron oxide (subtracting the NRL mass of the total mass). The

magnetization values for uncoated MNPs and NRL-coated MNPs considering the total mass (MNPs + NRL) and the magnetic nanoparticle mass are shown in Table 2.2.

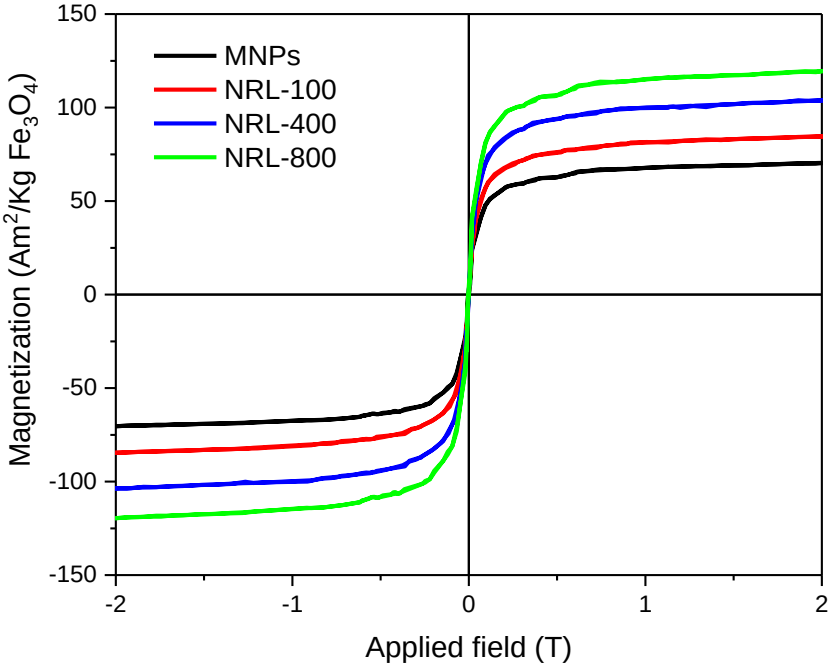

Figure 2. 8 Magnetization curves of bare MNPs and NRL-coated MNPs measured by Hall magnetometer considering only the mass of iron oxide nanoparticles.

Table 2. 2 Saturation magnetization values of bare MNPs and NRL-coated MNPs considering the total mass and the MNP mass.

Samples	**M_s at 2T Total Mass (Am^2/Kg)**	**M_s at 2T MNPs Mass (Am^2/Kg_{Fe3O4})**
MNPs	57	57
NRL-100	77	85
NRL-400	73	104
NRL-800	70	119

After subtracting the mass of NRL, the saturation magnetization of NRL-coated MNPs increases significantly (Table 2.2). The saturation magnetizations are 85, 104 and 119 Am^2/kg for NRL-100, NRL-400 and NRL-800 MNPs, respectively. So, latex can be considered an effective stabilizing agent with enhanced magnetization and suitable properties for biomedical applications.

2.4. Summary

In this work, we reported the green synthesis of iron oxide nanoparticles by a chemical co-precipitation method, using natural rubber latex at mild temperature. This method provides a straightforward way to tune the size and saturation magnetization of MNPs. The patterns obtained from XRD showed that MNPs with spinel structure were formed. TEM images showed that the NRL-coated MNPs have spherical morphology with particle sizes ranging from 7.9 to 13 nm. Increasing the NRL concentration produces smaller nanoparticles with a narrower size distribution. The NRL-coating improved colloidal stability, as evidenced by the increased positive zeta potential. FTIR spectroscopy revealed the presence of residual water in the uncoated nanoparticles, but not in the NRL-coated ones. The presence of bands related to the cis-1,4-polyisoprene confirmed that the MNPs were successfully coated with NRL latex. Magnetic measurements revealed a superparamagnetic behavior for the synthesized MNPs. Also, the NRL-coated MNPs have higher saturation magnetization value compared to the bare MNPs. Therefore, latex can be considered as an effective biocompatible stabilizing agent for the green synthesis of MNPs with improved saturation magnetization and suitable properties for biomedical applications like hyperthermia and MRI contrast agents.

Chapter 3: Magnetic Fe_3O_4 Nanoparticles Coated by Natural Rubber Latex as MRI Contrast Agent

3.1. Introduction

Magnetic nanoparticles (MNPs) due to their adjustable properties such as size, magnetism, and easy conjugation with biologically functional units have attracted considerable interest in biomedical applications such as cellular therapy in cell labelling [120], selective protein separation [121], hyperthermia in cancer treatment [122], targeted drug delivery [123] and magnetic resonance imaging (MRI) contrast agent [124]. Improvements in imaging modalities for the diagnoses of tumors, tissue damage, and neurological disorders have been investigated in the biomedical field using these particles [125].

Currently, the representative imaging modalities in preclinical research or clinical settings are X-ray computed tomography (CT), positron emission tomography (PET), ultrasound, single photon emission computed tomography (SPECT), magnetic particle imaging (MPI) and MRI [126]. Among them, MRI has been recognized to be one of the most important and non-invasive diagnostic technique. The stronger contrast of soft tissues and organs in MRI makes it a powerful and common diagnostic tool in medicine [127].

Over the last decades, the most used clinical MR contrast agents have been gadolinium (Gd) complexes that works based on the T1 (longitudinal relaxation) contrast agent. However, Gd-based complexes are toxic and they can cause brain lesions due to undesirable accumulation [128] or health risks for patients with chronic kidney disease (CKD) because these patients are not able to effectively remove these heavy metal complexes [129, 130]. Therefore, iron oxide nanoparticles (IONPs) have been emerged as an effective imaging contrast agent for MRI due to their versatile functionalization with surface capabilities and biocompatibilities. Several parameters of MNPs such as core size, size distribution, composition, shape, hydrodynamic size and surface coating strongly affect the MRI signal [42]. Presently, IONPs with ultra-small size have gained high

attention as safer T1 contrast agents compared to Gd-based [50]. Meanwhile, superparamagnetic iron oxide nanoparticles (SPIONs) and related ferrite NPs are widely used as T2 (transverse relaxation) contrast agents. They can reduce the T2 relaxation times due to their high magnetization. Therefore, IONPs can be used as contrast agents for both longitudinal relaxation and transverse relaxation depend on their core sizes.

Several studies evaluated the relationship between the core size of the MNPs and their relaxivities (r1 and r2), which are the slope of the plot of R1 and R2 relaxation, respectively, versus concentration in the units of mM^{-1} s^{-1} [51, 131]. They showed that values of the r1 and r2 relaxivities increase linearly with increasing particle core size. However, in this work, we evaluate the dependency of hydrodynamic size of NRL coated iron oxide nanoparticles on their relaxivities. These MNPs were synthesized using a simple co-precipitation method in a mild temperature (85^{o} C) with low concentration of iron salts. NRL, extracted from *Hevea brasiliensis*, was used as the surface coating. The relaxivity values of the bare MNPs and NRL-MNPs with different hydrodynamic size were investigated in the water phantom with 3 Tesla clinical MRI.

3.2. Materials and Methods

3.2.1. Synthesis of magnetic nanoparticles

The superparamagnetic iron oxide nanoparticles were prepared via a simple chemical co-precipitation method. Briefly, 3.37 g of $FeCl_3.6H_2O$ was dissolved in 12.5 ml distilled water and 1.98 g of $FeCl_2.4H_2O$ was dissolved in a 5 mL aqueous solution of hydrochloric acid (2.72 M). Then, the mixture of iron **(**III**)** chloride (1 ml) and iron (II) chloride (0.25 ml) was added to NH_4OH aqueous solution (1.28 M) with vigorous stirring at 85 ^{o}C temperature. The solution color changed rapidly to black indicating the formation of MNPs. The prepared sample was then washed with distilled water to remove chloride ions and reach a neutral pH. The final MNP preparation was dried in an oven at 32 ^{o}C.

3.2.2. Synthesis of NRL-magnetic nanoparticles

NRL-magnetic Fe_3O_4 nanoparticles were synthesized using a co-precipitation method in a mild temperature (85 ^{o}C), similar to the procedure reported in the literature [132]. However, because small nanoparticles are preferred for MRI contrast imaging [133-135], we employed here lower concentration of iron salts in order to produce smaller nanoparticles. Therefore, in this synthesis,

an NRL solution (100 µL and 400 µL) was added to the NH_4OH (1.28 M) aqueous solution. Afterwards, the basic solution was heated up to 85 ^oC for 5 minutes. After adding the mixed solution of iron salts to the NRL and NH_4OH solution under vigorous stirring, a black precipitate formed instantly. Synthesized NRL-MNPs were washed with Milli-Q® water a few times until a neutral pH was achieved, then they were dried at 32 ^oC. The synthesized MNPs were named according to the volume of NRL added during the synthesis. For example, the sample prepared with 100 µL of NRL was named MNPs-100NRL and so on.

It is worth noting that MNPs with NRL concentration such as 800 µL were synthesized, but because of the low concentration of iron salts and high concentration of NRL we observed polymerization after adding iron salts. Therefore, when the concentration of iron salts is low the amount of NRL should be lower than 800 µL.

3.2.4. Characterization of magnetic nanoparticles

The synthesized MNPs were characterized by various techniques. The phase identification of MNPs was obtained by an XRD (D5005 Diffractometer, Bruker) analysis using X-ray beam nickel-filtered Cu-K radiation (λ=1.5406 Å) in the range $10°<2\theta°<70°$. The morphology and core size of the MNPs were investigated through transmission electron microscopy (TEM) using a JEOL-JEM-100 CXII instrument, by drying a drop of the washed colloidal dispersion onto a copper grid covered with a conductive polymer. The hydrodynamic size of the nanoparticles suspensions was acquired by dynamic light scattering (DLS) using a Zeta-Sizer system (Malvern Instruments). The data was collected at a fixed angle (90^o) and fixed wavelength (633 nm He–Ne laser). The magnetic properties of the MNPs were measured by a custom-made Hall effect magnetometer [97]. The measurements were taken at room temperature (25 °C) and under different applied magnetic fields from – 2.0 to +2.0 T. The magnetization curves were normalized by the mass of IONPs, the mass of the latex was subtracted from the total mass of each sample, more details can be find in reference [132]. The temperature dependence of the DC magnetization was measured in both zero-field cooled (ZFC) and field cooled (FC) regimes in a wide temperature range (10−300 K), applying 5.0 mT magnetic field.

3.2.5. Relaxivity measurements

To estimate the nuclear relaxivity characteristics of the bare MNPs and NRL-MNPs, longitudinal (T1) and transverse (T2) relaxation times were assessed via alteration of the Fe concentration. The synthesized MNPs at various iron concentrations (0.2, 0.5, 0.8, 1.1, and 1.4 mM) were incorporated in a gelatin matrix to simulate biological tissues. All MR relaxation measurements were performed on a 3.0 T MRI scanner (PHILIPS, Achieva). Spin echo sequence with 10 different repetition time (TR=200-1850 ms) was used for T1 assessment. A multi-spin echo sequence with eight different echo times (TE=14-112 ms) was performed for T2 estimation. For both cases, the final image resulted in a FOV of 110 x 110 mm^2, effective pixel size of 0.52 mm. MRI data were fitted to well-known MRI relaxation equations using a script written based on *MATLAB2016*® to obtain R1 (1/T1) and R2 (1/T2) values. From these values for different iron concentrations, relaxivity values (r1 and r2) were calculated using a linear fit for each latex content condition.

3.3. Results and Discussions

The XRD pattern of the bare MNPs and NRL-MNPs is presented in Figure 3.1. The XRD pattern of the synthesized samples shows diffraction peaks indexed to (2 2 0), (3 1 1), (4 0 0), (4 2 2), (5 1 1), (4 4 0) and (5 5 3) reflection characteristics of cubic spinel phase of magnetite (JCPDS card no. 85-1436), revealing a magnetite crystalline phase of the prepared magnetic nanoparticles (Fe_3O_4) [110]. The average crystalline size was calculated from the (3 1 1) diffraction peaks by using Scherrer's equation. The average crystal size of bare MNPs, MNPs-100NRL and MNPs-400NRL were calculated as 9.5, 7.8 and 7 nm, respectively.

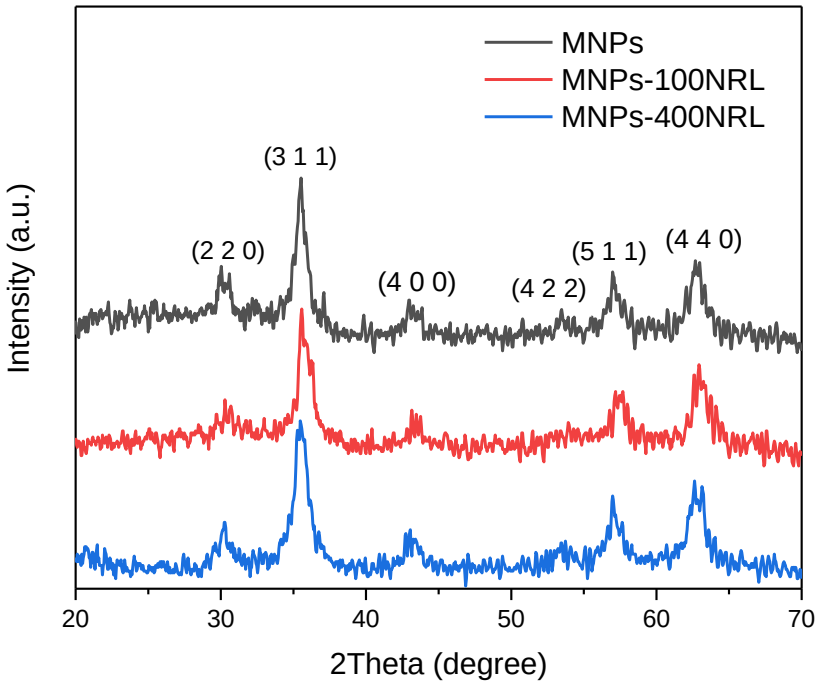

Figure 3. 1 XRD patterns of bare MNPs and NRL-MNPs.

The morphology and core size of MNPs were characterized by TEM. Histograms of the size distributions and TEM images of bare MNPs and NRL-coated MNPs shown in Figure 3.2 (a-f). It can be observed that iron oxide particles with small core size were produced. The average sizes for bare MNPs, MNP-100NRL, MNPs-400NRL were estimated 14±5, 10±2 and 9.2±2 nm, respectively. The size distribution of bare MNPs is very broad (Figure 3.2 (b)) and two Gaussian peaks with mean average size of 10 and 20 nm can be considered for this histogram. The TEM sizes of MNPs as measured here are in good agreement with the average crystal sizes obtained by XRD pattern. The average size and size distribution of MNPs decrease by using NRL. Size reduction can be caused due to attaching of rubber molecules to the surface of the particles during the synthesis thus preventing the growth and agglomeration of MNPs [132].

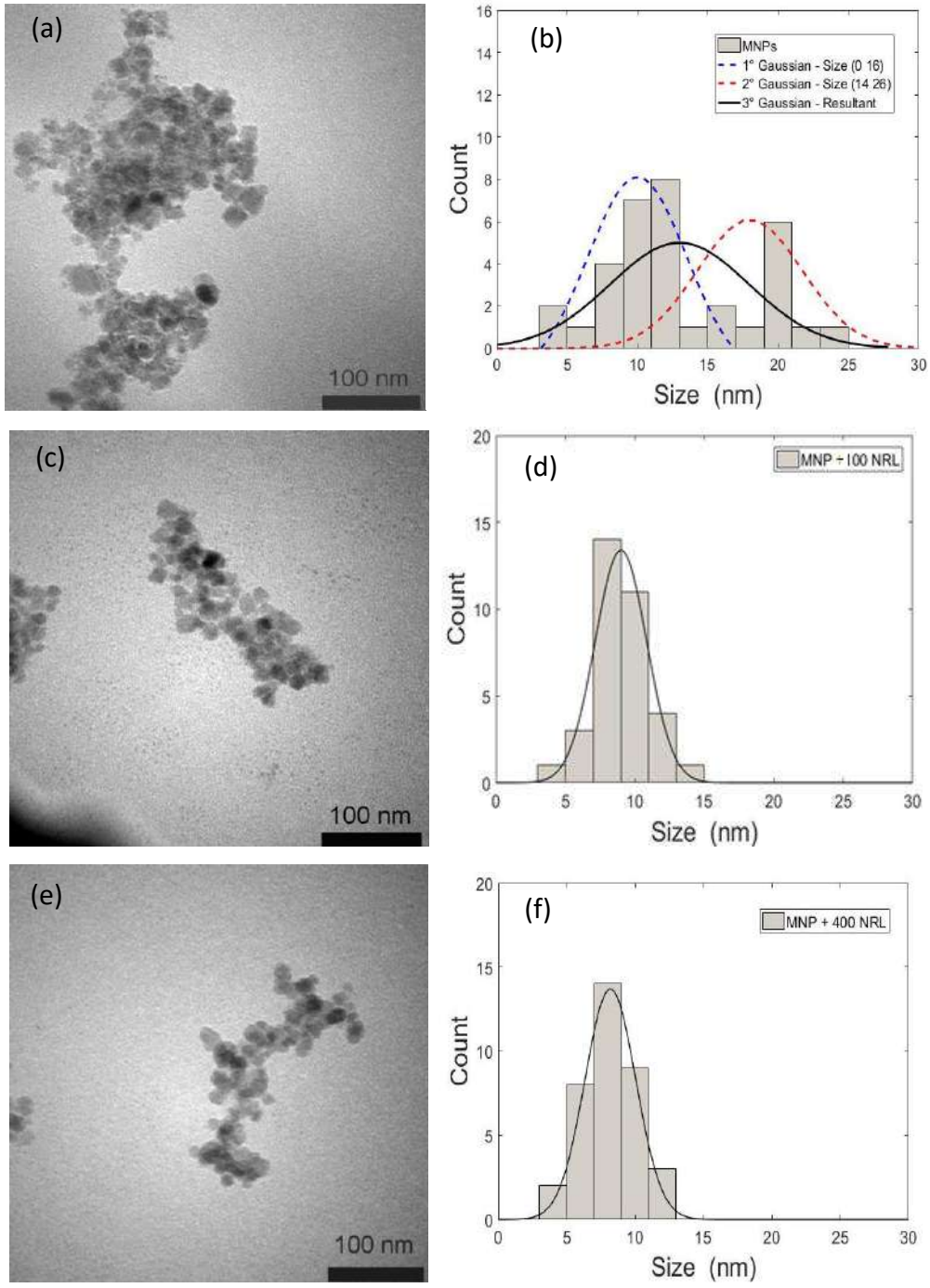

Figure 3. 2 TEM images and histograms of (a-b) bare MNPs, (c-d) MNPs-100NRL, and (e-f) MNPs-400NRL.

The hydrodynamic size of the iron oxide nanoparticles, which is the core size of the nanoparticle and the surrounding layer (core+shell), was measured by dynamic light scattering (DLS). The hydrodynamic sizes for bare MNPs, MNPs-100NRL and MNPs-400NRL are 66, 80 and 105 nm,

respectively. It can be seen (Table 3.1) that the hydrodynamic size of MNPs increases by NRL concentration, suggesting the formation of a thicker NRL shell on the surface of bare MNPs as the NRL concentration increases. Table 3.1 summarizes the size of MNPs obtained by XRD, TEM and DLS techniques.

Table 3. 1 The measured size of MNPs by XRD, TEM and DLS techniques.

Samples	**NRL (µL)**	**XRD size (nm)**	**TEM size (nm)**	**DLS size (nm)**
MNPs	0	9.5	14±5	66
MNPs-100NRL	100	7.8	10±2	80
MNPs-400NRL	400	7.0	9±2	105

Figure 3.3 shows the magnetization curve of prepared samples, normalized to the iron oxide mass (Fe_3O_4), obtained by a Hall magnetometer at room temperature. Magnetization curves demonstrate neither coercivity nor remanence and saturation at 2.0 T field, showing that the prepared MNPs have typical characteristics of superparamagnetism at room temperature [77]. The magnetization values at 2.0 T of bare MNPs, MNP-100NRL and MNPs-400NRL were 53, increase to 67 and 81 Am^2/kg-Fe_3O_4 respectively. The uncertainty in the magnetization values is ± 0.2 Am^2/kg [97].

As it can be observed (Figure 3.3) the magnetization value of the NRL-coated MNPs is higher than the magnetization of bare magnetic nanoparticles and by increasing the amount of NRL, magnetization increases. The improved magnetic properties of the NRL-coated MNPs can be attributed to the elimination of residual water (hydroxyl groups) upon binding of the NRL molecules onto the MNPs surface, leading to better crystal quality and consequently higher magnetization [132]. In addition, the surface ligands can decrease the interparticle interactions. Thus by enhancing the amount of NRL, the interparticle interactions decrease, which may facilitate the re-order of the spins at MNP surface and consequently increasing the magnetization of MNPs [79, 132, 136].

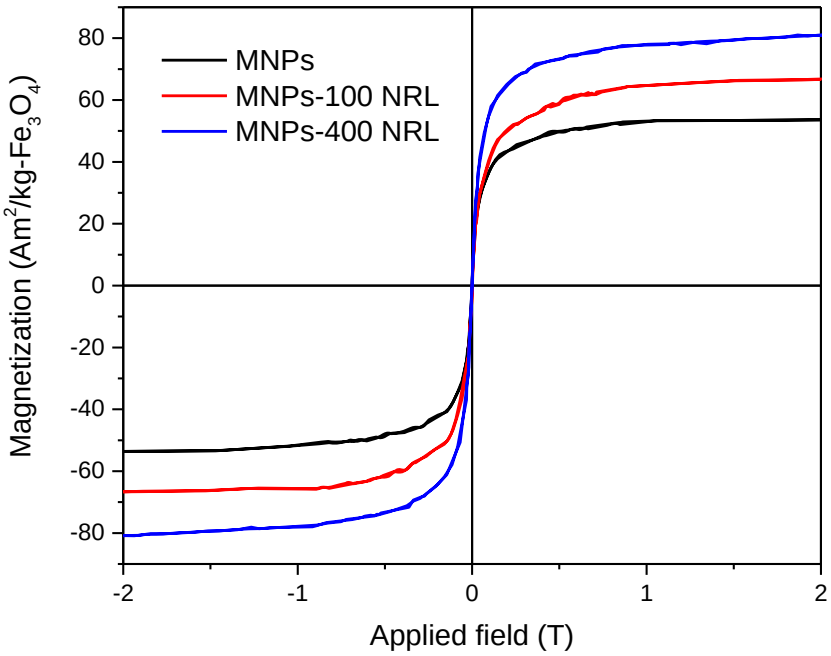

Figure 3. 3 Magnetization curves of prepared MNPs at room temperature by considering the only mass of iron oxide nanoparticles.

Figure 3.4 shows the zero-field-cooled (ZFC) and field-cooled (FC) curves of the prepared MNPs. ZFC magnetizations were obtained by cooling sample in a zero magnetic field and then increasing the temperature ranging from 10 K to 300 K in a small magnetic field of 5.0 mT, while FC curves were measured by cooling the samples from 300 K in the same external field. Commonly, in ZFC curve, magnetization increases with temperature and reaches the maximum at a characteristic temperature. This peak temperature of ZFC is identified as the blocking temperature (T_B) [137]. Above the blocking temperature, the magnetization decreases as the temperature increases.

Figure 3.4 reveals that the magnetization ZFC curve coincides with FC curve above 100 K. Furthermore, the irreversible behavior of these curves evidences the superparamagnetism characteristic of MNPs [138]. Thus, the ZFC/FC curves agree with the magnetization results. The temperature at the ZFC peak of bare MNPs is about 98 K and is shifted to a significantly lower value of 73 K and 68 K for MNPs-100NRL and MNPs-400NRL, respectively. Indeed, for the iron oxide NPs, transition from the blocked to the superparamagnetic regime occurs at different temperatures for different particle sizes. It is observed that, all samples exhibit T_B at lower temperature than 100 K and was influenced by the particle size of MNPs. The higher T_B value in

ZFC curves was obtained for larger magnetite nanoparticles (bare MNPs) and the lower blocking temperatures were obtained for smaller nanoparticles (NRL-MNPs).

Generally, blocking temperature increases with increasing particle size of the NPs, because the distance between the particles is not enough to reduce the dipolar interactions [138, 139]. Therefore, by covering MNPs with NRL and decreasing the core size, the blocking temperature will be diminished. Without covering of MNPs the agglomeration of the nanoparticles will take place, because of the increased attractive force between the nanoparticles. The agglomerated nanoparticles act as a cluster, leading to an increase in the blocking temperature [74].

The broad peak of the ZFC and flattening of the FC curve of bare MNPs, as shown in Figure 3.4, can be due to the anisotropic distribution of the iron oxide nanoparticles and strong interactions between nanoparticle moments [140-143]. The anisotropic distribution is consequence of the size distribution of the nanoparticles. The enhancement in the standard deviation from $\sigma = 2$ to 5 with increases in size from 9 to 14 nm also provides us with confirmation of the broadening anisotropic distribution of the bare magnetic nanoparticles.

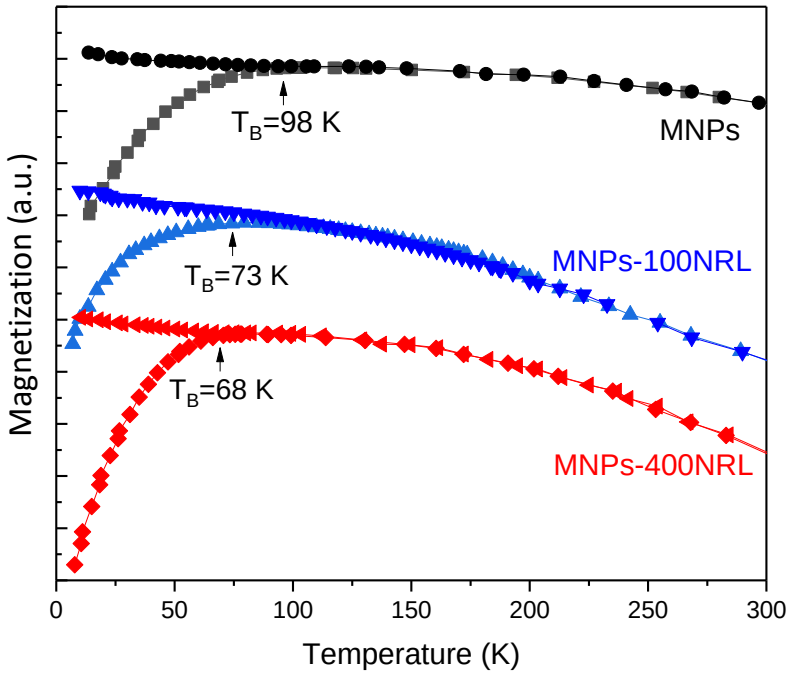

Figure 3. 4 Temperature dependence of magnetization in ZFC and FC protocols for bare MNPs and NRL-MNPs.

The MRI relaxation properties of the bare MNPs and NRL-MNPs were characterized using a MRI scanning system with a magnetic field of 3T. Figure 3.5 (a, b) shows the T1-weighted and T2-weighted images of nanoparticles at different concentrations of Fe_3O_4 (0.2, 0.5, 0.8, 1.1, and 1.4 mM) in gelatin matrix.

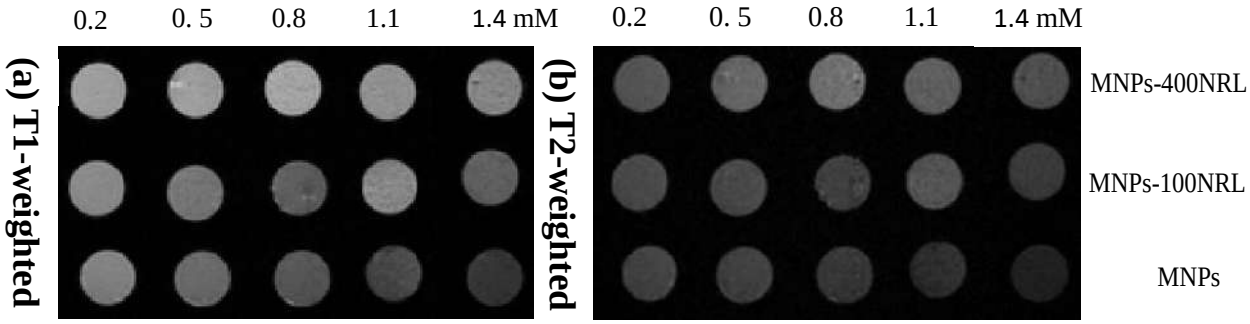

Figure 3. 5 (a) T1-weighted and (b) T2-weighted images of bare MNPs, MNPs-100NRL and MNPs-400NRL at different concentrations of Fe_3O_4.

To quantitatively analyze the MRI relaxation properties of nanoparticles, the longitudinal (R1) and transversal (R2) relaxation rates of MNPs were extracted using a Matlab software script. Figure 3.6 (a, b) shows the R1 and R2 relaxation rates as a function of the concentration of MNPs for all prepared samples. We can observe (Figure 3.6 (a)) bare MNPs has higher R2 values compare to NRL coated MNPs and by increasing the amount of latex R2 significantly decreases, while R1 shows a slight decrease (Figure 3.6 (b)). Although the MNPs-400NRL has core size close to the MNPs-100NRL, the shell thickness is larger, as indicated by the DLS measurements (Table 3.1), leading to larger total particle size (core + shell). Therefore, a possible explanation for this effect is associated with the hydrodynamic size of these particles, resulting in the physical exclusion of the protons from the magnetic field and decreasing R1 and R2. Similar behavior have been reported for coating MNPs with PEG [144]. The r1 and r2 values of MNPs are shown in Table 3.2.

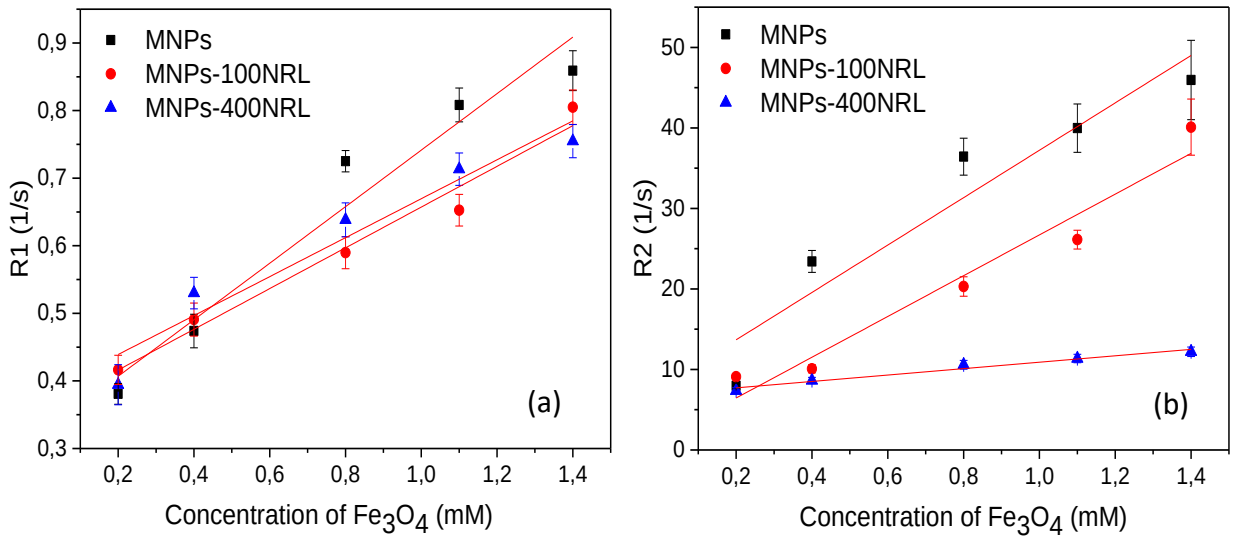

Figure 3. 6 (a) Plots of R1 and (b) R2 relaxation rates of bare MNPs, MNPs-100NRL and MNPs-400NRL.

Table 3. 2 The r1 and r2 values of as-prepared MNPs.

Samples	**r1 (mM^{-1} s^{-1})**	**r2 (mM^{-1} s^{-1})**	**r2/r1**
MNPs	0.69 ± 0.26	31.3 ± 5.3	45.1 ± 1.7
MNPs-100NRL	0.68 ± 0.23	20.5 ± 3.2	30.0 ± 1.6
MNPs-400NRL	0.55 ± 0.22	3.9 ± 0.3	7.3 ± 3.4

The r2 values of bare MNPs, MNPs-100NRL and MNPs-400NRL were 31.3, 20.5, and 3.9 mM^{-1} s^{-1}, and the r1 values were 0.69, 0.68, and 0.55 mM^{-1} s^{-1}, respectively (Table 3.2).

Our results clearly show that it is possible to tailor the coating thickness to affect the r2/r1 ratio. This ratio is important because it is employed in several cases to distinguish between normal and malignant tissues. Figure 3.7 indicates the relaxivity ratio r2/r1 diminishes with the NRL concentration, this behavior is determined by r2 reduction of MNPs.

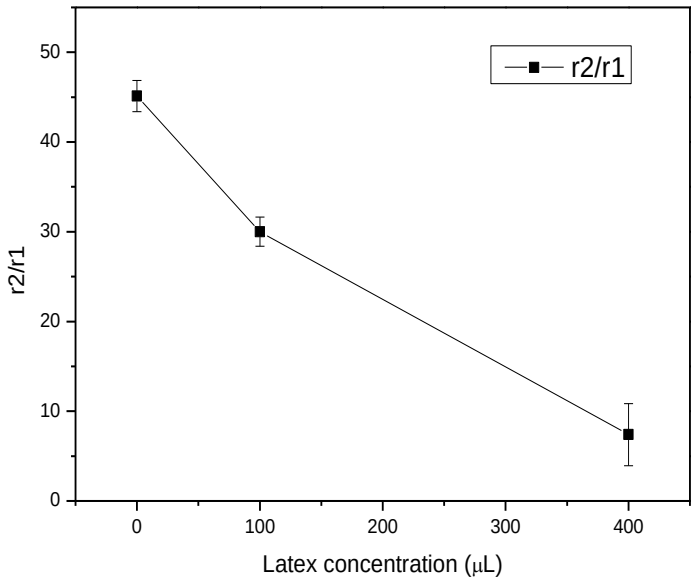

Figure 3. 7 The r2/r1 ratios of prepared MNPs with different NRL concentration.

The r2/r1 ratios of bare MNPs, MNPs-100NRL and MNPs-400NRL are 45.1, 30, and 7.3, respectively. Therefore, based on the type of diseases and desirable r2/r1 ratio we can apply the prepared MNPs with suitable thickness of NRL as MRI contrast agents.

3.4. Summary

In this work, superparamagnetic iron oxide nanoparticles were synthesized by a chemical co-precipitation method using natural rubber latex as covering agent. The XRD patterns revealed magnetic nanoparticles (Fe_3O_4) with spinel structure and small crystal size between 7 nm to 9.5 nm were formed. Using NRL caused smaller nanoparticles with narrower size distribution, higher hydrodynamic size and lower blocking temperature compare to the bare MNPs. NRL coated MNPs demonstrated superparamagnetic behavior with high magnetization values. In conclusion, we have shown that the thickness of the NRL coating of MNPs can significantly affect their relaxivity. As coating thickness increases, there is a considerable decrease in r2 and a slight decrease in the r1 of the prepared NRL-MNPs. Therefore, relaxivity ratio r2/r1 of MNPs can be controlled by adjusting the NRL concentration during the synthesis process.

Chapter 4: Synthesis of Radioluminescent Iron Oxide Nanoparticles Functionalized by Anthracene for Biomedical Applications

4.1. Introduction

Magnetic nanoparticles (MNPs) play a significant role in medicine and biotechnology such as detection of biomarkers, cancer diagnosis and therapy. In particular, iron oxide (Fe_3O_4) nanoparticles (IONPs) due to their low toxicity, high magnetization and high biocompatibility [145, 146] have received considerable attention in biomedical applications, including contrast agents in magnetic resonance imagining (MRI) and ultrasound [147, 148], fluorescence imaging [149], cell and protein separation and detection [150], treatment by hyperthermia [151, 152], drug and siRNA delivery [153, 154], and also in bio and chemo-sensing [155].

Several parameters of MNPs such as core size, size distribution, shape, surface functionalization and degree of crystallinity play essential roles in determining the magnetic response of MNPs, therefore influencing their biomedical activity [132]. Usually, IONPs with core size smaller than 50 nm become a single magnetic domain and when the temperature is above a certain value, called the blocking temperature, they show superparamagnetic behavior. Nanoparticles (NPs) in the superparamagnetic state present large magnetic moments without any remanence and coercivity [77]. Therefore, by removing external magnetic field no magnetic moment will remain in superparamagnetic NPs, resulting in preventing the side effects of aggregation, such as blocking of lymphatic vessels [156]. These features make superparamagnetic NPs very interesting for biomedical applications. Another interesting possibilities of these MNPs is that they are able to be easily functionalized with monoclonal antibodies, peptides or proteins, different hydrophobic and hydrophilic coatings, drug molecules and fluorescent compounds [157]. There is currently a focus on the synthesis of small nanoparticles which possess both magnetic and fluorescent/luminescent properties [158]. Mostly, the fluorescence is determined by the molecular electronic structure and molecular geometry. However, the fluorophore environment can strongly affect these properties.

The essential environmental factors which can have an influence on fluorescence properties are the solution pH, temperature, solvent polarity, ionic strength and oxygen concentration. Moreover, the fluorescent properties are dependent on other processes such as electron and resonance energy transfer and quenching [159].

The main challenge in synthesizing MNPs with fluorescent properties is quenching the fluorescence of the fluorophore by the magnetic core [160]. In several studies, MNPs specially IONPs have been used as a fluorophore quencher. For instant, Cheng Yu et al. [161] used Fe_3O_4 nanoparticles as a highly efficient fluorescence quencher for BODIPY-ATP. They have shown that the quenching mechanism is due to photoinduced electron transfer (PET) from the BODIPY-ATP excited state to the unfilled d shell of Fe^{3+} and Fe^{2+}. Chan Song et al. [162] have shown the fluorescence quenching ability of α-Fe_2O_3 nanoparticles towards different fluorophore-labelled nucleic acid probes based on a contact quenching mechanism. Therefore, fluorescence quenching can occur due to strong interactions between the fluorophore and the surface of the magnetic core, resulting in energy and electron transfer processes between them and then quenching process [157, 162-164]. The most common way to prevent quenching of the fluorescent intensity is to coat the core of MNPs with an insulating layer such as silicon dioxide, or embed these MNPs into a polymer matrix [160, 164]. However, coating MNPs by silicon or some polymers may lead to a significant decrease in magnetization [165-167].

The MNPs coated by fluorescent materials can be oriented and heated by external magnetic fields, and can also provide a sensitive label for imaging in cells. Therefore, they can be used as a multimodal diagnostic and therapeutic tool [160]. However, biological tissues are not significantly responsive to magnetic fields, and magnetic fields can pass through tissue without considerable absorption but fluorescence measurements have some limitations in thick tissue due to optical scattering and autofluorescence backgrounds [168]. Radioluminescent materials can resolve this disadvantage due to the low background. Moreover, the radioluminescence emitted by the nanoparticles could be used in photodynamic therapy processes, thus resolving the problem of light scattering in deep tumors when external sources are employed.

Herein, we developed a multifunctional magneto-radioluminescent NPs for biomedical applications. The synthesis of magnetic (γ-Fe_2O_3) radioluminescent NPs have previously been reported by Chen et al. [168], but these MNPs did not present superparamagnetic behavior, which

is essential for in vivo biomedical applications. They showed ferrimagnetic properties with high remanence and coercivity that it may lead to some drawbacks such as aggregation of MNPs in the absence of magnetic field, resulting in clogging blood or blocking vessels.

To our knowledge, the synthesis of superparamagnetic iron oxide NPs with radioluminescent properties, by an organic molecule, has not been reported previously, which is so important for biomedical applications. In this work, our challenge is to synthesize small superparamagnetic iron oxide NPs with high fluorescent and radioluminescent properties. The IONPs were synthesized by the thermal decomposition method and covered by oleic acid (OA) in order to stabilize and protect the magnetic core against oxidation [169], additionally the strong interactions between the surface of magnetic core and fluorophores can be reduced. The monodisperse IONPs/OA coated were modified by anthracene (AN) as a fluorophore. Finally, the prepared IONPs/OA/AN nanocomposites were functionalized by polyvinyl alcohol (PVA) to disperse in aqueous solution. The prepared multifunctional IONPs/OA/AN/PVA nanocomposite with magnetic, fluorescent and radioluminescent properties can be a potential candidate for biomedical application.

4.2. Materials and Methods

4.2.1. Synthesis

Monodisperse IONPs covered by OA were synthesized by the thermal decomposition method according to the reported procedure in two steps [45]. The first step is to prepare an iron-oleate precursor, while the second step is the actual synthesis of iron oxide nanoparticles.

4.2.1.1. Synthesis of iron-oleate complex

In a typical synthesis of iron-oleate complex, 5.4 g of $FeCl_3 \cdot 6H_2O$ and 18.25 g of sodium oleate were dissolved in a solvent containing 40 ml of ethanol, 30 ml of distilled water and 70 ml of hexane. The solution was heated to 70 ^{o}C for 4 h. When the reaction was completed, the iron-oleate complex was washed four times in a separating funnel. Then, the resultant iron-oleate complex was kept in an oven at 40 ^{o}C to evaporate the hexane.

4.2.1.2. Synthesis of iron oxide nanoparticles/oleic acid

In a typical experiment for 6 nm particles, 3.6 g of the prepared iron-oleate complex and 0.57 g of oleic acid were dissolved in 20 g of 1-octadecene. The reaction mixture was heated to 325 ^{o}C with

a constant heating rate of 3.3 C min^{-1}, and then kept at that temperature for 20 min. As the temperature in the mixture reached 322 ^{o}C, the initial reddish-brown color of the solution turned to brownish black, resulting in the formation of nanoparticles. Then, the prepared IONPs/OA were washed several times with a mixture of hexane and ethanol. After washing, the IONPs/OA were dried in an oven at 40 ^{o}C for 12 h.

4.2.1.3. Synthesis of iron oxide nanoparticles/oleic acid /anthracene

IONPs/OA/AN were prepared by adding AN to IONPs/OA in a 3:1 w/w ratio, respectively. Liquid assisted grinding was followed by adding ethanol to this mixture, taking the ratio of liquid volume to mass of solid IONPs as 500 μL mg^{-1}, and the mixture was then ground for 20 minutes at room temperature. The prepared nanocomposites were washed several times with ethanol and separated by a permanent magnet in order to remove the excess free or unbound anthracene.

4.2.1.4. Synthesis of iron oxide nanoparticles/oleic acid/anthracene/PVA

Polyvinyl alcohol (PVA), a water soluble hydrophilic polymer with superb functionalization ability adhesive properties along with biocompatibility, was used to disperse the prepared IONPs/OA/AN in aqueous solution. About 15 μL of a PVA water solution 1.25 mg/mL was added to 5 mg/mL of iron oxide mass of IONPs/OA/AN solution. The solution was gently mixed for a certain time. Then, the IONPs/OA/AN nanocomposite will be covered by PVA and the final nanocomposite (IONPs/OA/AN/PVA) can be kept in water. Figure 4.1 (a- d) represent the schematic of the IONPs/OA/AN/PVA preparation. The images of IONPs/OA inside hexane and IONPs/OA/AN/PVA inside water are shown in Figure 4.2 (a, b), respectively.

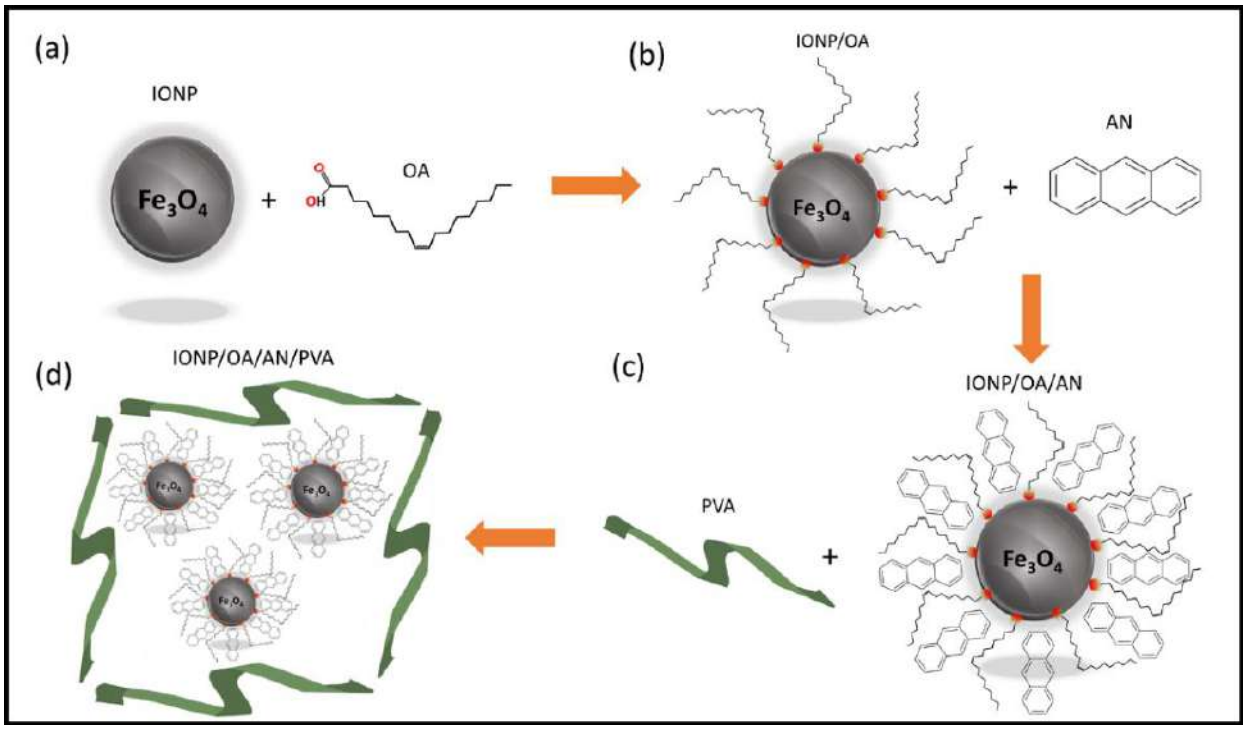

Figure 4. 1 (a- d) The schematic representation of the IONPs/OA/AN/PVA preparation showing the main steps involved in the synthesis.

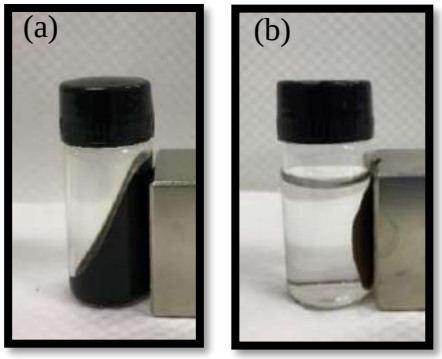

Figure 4. 2 (a) Images of IONPs/OA in hexane, and (b) IONPs/OA/AN/PVA in water.

4.2.2. Characterization of iron oxide nanoparticles/oleic acid/anthracene/PVA

The prepared samples were characterized by different methods. The crystalline properties and phase identification of MNPs were obtained by XRD (D5005 Diffractometer, Bruker) analysis, using X-ray beam nickel-filtered copper K radiation (λ = 1.5406 Å) in the range of $10° < 2\theta° < 70°$. The morphology and core size of particles were investigated by transmission electron

microscopy (TEM; JEOL-JEM- 100 CXII), by drying a drop of the washed colloidal dispersion onto a copper grid. The TEM size of particles was measured using ImageJ software. The hydrodynamic diameter (h_d) and polydispersity index (PDI) of the water dispersible nanocomposite were measured by dynamic light scattering (DLS) using a Zeta-Sizer system (Malvern Instruments). The data was measured at a fixed angle of 90 degree and wavelength of 633 nm He–Ne laser. The surface functionalization was verified by FTIR spectroscopy (Shimadzu IRPrestige-21) in the region between 4000 and 500 cm^{-1}. Simultaneous thermal analyses (TGA/DSC) of the samples in powder form were measured from 25 to 800 ^oC under a N_2 atmosphere ramp of 10 ^oC/min using TGA/DTA/DSC Equipment (Model SDTQ600-TA Instruments).

The magnetic properties of the samples were measured by a custom-made Hall effect magnetometer [97]. The measurements were taken at room temperature (25 °C) using applied magnetic fields in the range −2.0 to +2.0 T. The magnetization curves were normalized by the mass of magnetic core (Fe_3O_4). The mass of the organic coatings was subtracted from the total mass of the sample based on TGA measurements.

The Fluorescence spectra of the samples were recorded using a Hitachi F-7000 spectrofluorometer equipped with a 150 W xenon arc lamp. The excitation and emission monochromator slit widths were set at 5 nm. Radioluminescence measurements were performed under X-Ray irradiation from an X-ray tube (GE-Isovolt Titan E-160M-2), operating at 160 kVp and varying the tube current (2-10 mA). The X-ray dose rate at the sample position was around 9 Gy/min.

4.3. Results and Discussions

4.3.1. Composition, size and morphology

Figure 4.3 (a, b) shows the X-ray diffraction pattern of pure AN, IONPs/OA and IONPs/OA/AN/PVA. The XRD pattern of AN (Figure 4.3 (a)) depicts the lattice planes (-111), (002), (-202), (200), (-210) and (-222), where all of these peaks appear in the IONPs/OA/AN/PVA pattern (Figure 4.3 (b)) [170, 171], showing the presence of AN with the same lattice planes in nanocomposite. In addition, the IONPs/OA pattern exhibits 2θ values at 30.1, 35.5, 43.1, 57.0, and 62.6° corresponding to reflection planes (220), (311), (400), (511), and (440) of the magnetite crystal structure, respectively (JCPDS card no. 85-1436) [132]. The position and relative intensity

of all peaks for IONPs/OA/AN/PVA match well with the IONPs/OA sample, suggesting that this sample also has a magnetite structure and the core is stable in terms of the crystalline phase, even after modifying IONPs/OA with AN and PVA. The lattice planes of AN in IONPs/OA/AN/PVA spectrum are marked with stars and the magnetite phases are marked by plus signs. Note, due to the high intensity of AN peaks, the peaks of magnetite phase appear small and broad, therefore we insert the XRD pattern of IONPs/OA in Figure 4.3 (b) to be more clear the magnetite peaks.

The mean crystallite size of IONPs/OA was obtained from the half-width at half maximum of the peaks (311), and calculated by the Scherrer equation [172]. The estimated average crystallite size of IONPs/OA was estimated as 6 nm.

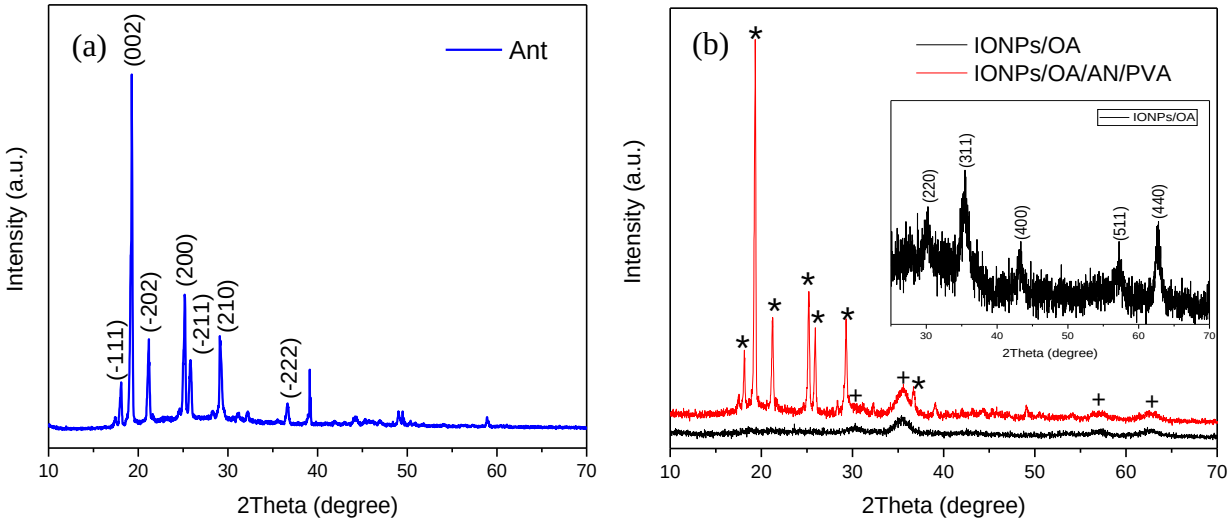

Figure 4. 3 (a) XRD pattern of pure AN and (b) IONPs/OA and IONPs/OA/AN/PVA.

The TEM images and histograms of the size distribution of IONPs/OA in hexane and IONPs/OA/AN/PVA in water are shown in Figure 4.4 (a- d), respectively. It was observed that the monodisperse IONPs/OA and IONPs/OA/AN/PVA were composed of almost spherical particles with a mean size of 6.2±1.2 nm and 5±1.2 nm, respectively, which is in good agreement with XRD results. The slight reduced core size of MNPs in IONPs/OA/AN/PVA nanocomposite can be due to the grinding of IONPs/OA with AN.

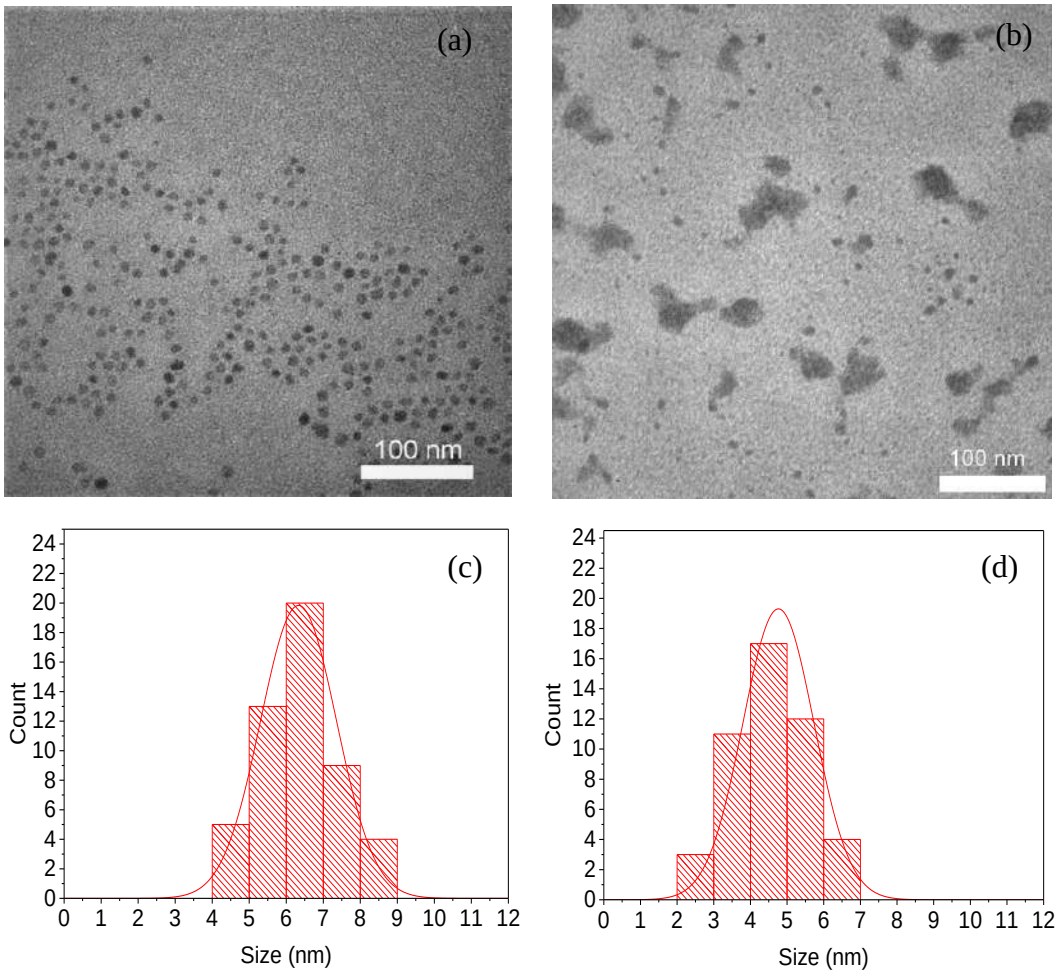

Figure 4. 4 (a, b) TEM images, and (c, d) histograms of the size distribution of IONPs/OA and IONPs/OA/AN/PVA, respectively.

Since the hydrodynamic diameter and polydispersity of MNPs are essential for biomedical applications, these parameters were measured for IONPs/OA/AN/PVA sample in aqueous phase by DLS (Figure 4.5). The d_h and PDI of the prepared nanocomposite are about 72 nm and 0.28, respectively. The d_h of this nanocomposite is larger than the size by XRD and TEM, because XRD shows the crystallite size of the particles and the obtained sizes in TEM histogram (Figure 4.4 (d)) are related to the core size of MNPs, while DLS indicates the overall size, taking into account the magnetic core, the organic layer (OA, AN and PVA), and the ions surrounding the nanocomposite [173]. In addition, the polymer may coat a few particles together, as it was shown in Figure 4.1 (d) and 4.4 (b), resulting in increased hydrodynamic size.

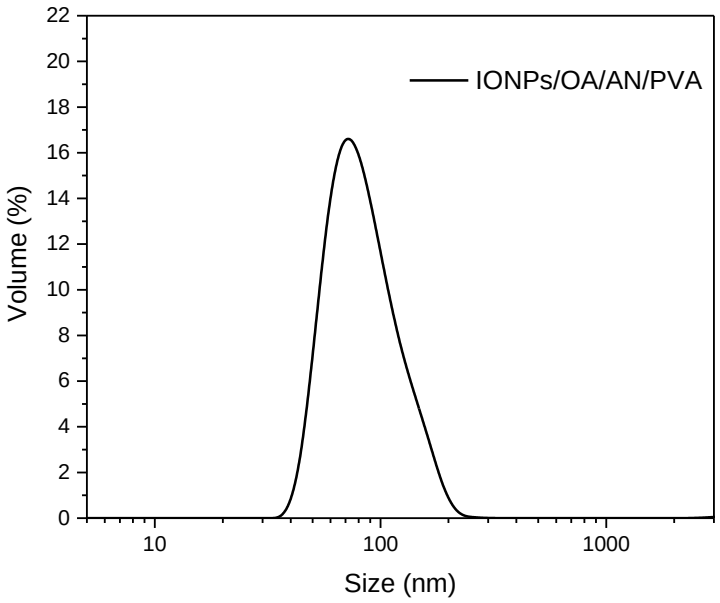

Figure 4. 5 The hydrodynamic diameter of the IONPs/OA/AN/PVA sample by DLS measurement.

4.3.2. FTIR spectroscopy and TGA

The FTIR spectra of Figure 4.6 show a comparison of the IONPs/OA, IONPs/OA/AN/PVA, and AN in the wavenumber ranging from 4000 cm^{-1} to 500 cm^{-1}. The observed spectrum of IONPs/OA agrees with those previously published by various researchers [169, 174-176]. The analysis of IONPs/OA and IONPs/OA/AN/PVA indicates absorption peaks at 580 cm^{-1}, corresponding to the Fe–O vibration related to the magnetite phase [71]. In addition, these spectra show the presence of 1425 cm^{-1} and 1545 cm^{-1} bands characteristic of the symmetric (*v*s: COO^{-}) and asymmetric (*v*as: COO^{-}) stretching vibration, respectively. These bonds are attributed to the oleate ion immobilized on the surface of magnetite nanoparticles [177, 178]. According to some authors [179, 180], the type of interactions between metal atoms and carboxylate head of OA can be distinguished by the wavenumber separation of *v*as (COO^{-}) and *v*s (COO^{-}) bands. Since, the wavenumber separation of the IONPs/OA before and after functionalizing with AN and PVA is almost the same (Δ= 1545-1425= 120 cm^{-1}) it can be concluded that the interactions between OA and metal atoms have not changed after grinding AN with IONPs/OA. Furthermore, all peaks of pure AN, including a small peak around 3047 cm^{-1} that is attributed to aromatic C–H stretching and the two intense peaks at 724 cm^{-1} and 884 cm^{-1} that are assigned to C–H out-of-plane bending vibration and C-H aromatic bending vibration of AN [170, 181] can be observed in FTIR spectra of IONPs/OA/AN/PVA

nanocomposite. These FTIR results reveal the presence of AN and OA in the final prepared nanocomposite.

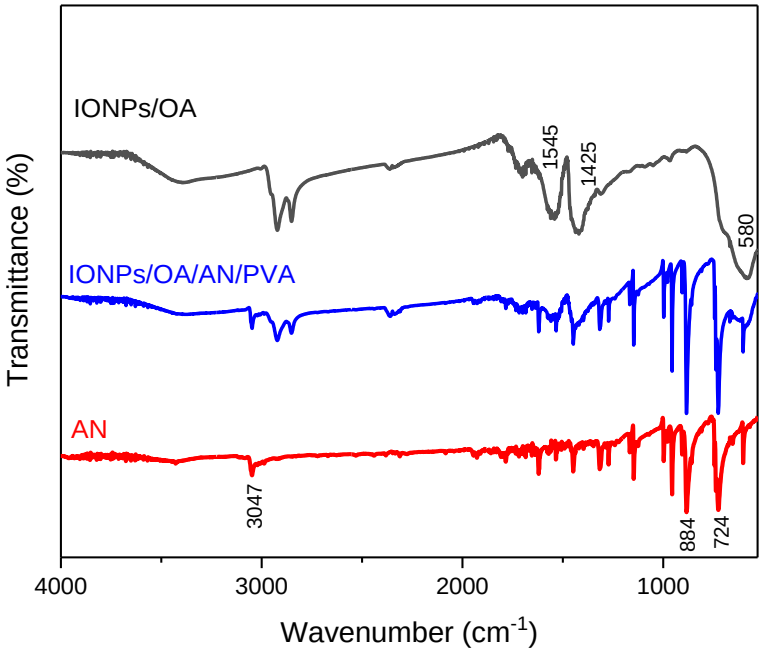

Figure 4. 6 FTIR spectra of IONPs/OA, IONPs/OA/AN/PVA, and AN.

Further evidence of the presence of AN is provided from the weight loss observed during TGA. This analysis was employed for IONPs/OA, IONPs/OA/AN/PVA and pure AN (Figure 4.7 (a)). The degradation curves of IONPs/OA and IONPs/OA/AN/PVA demonstrated the loss percentages of approximately 3 % and 2 % , respectively, under the temperature of 150 °C, which are related to the water molecules adsorbed on the nanoparticle surface [182, 183]. Two significant losses are observed on IONPs/OA curve between 180 to 420 °C; the first weight loss is at 260 °C, and the second weight loss appears at 350 °C (Figure 4.7 (b)). The first weight loss, which may be due to OA being weakly bound to the MNP surface, is about 15 %; and the second weight loss, which can be attributed to the bonded OA on the surface of MNPs, is almost 36 % [183-185]. For pure AN, Figure 4.7a reveals that AN is thermally stable up to 140 °C, and totally decomposed at 245 °C. The TGA degradation profile of IONPs/OA/AN/PVA is showing weight losses at three steps of 240, 300 and 350 °C, in which the first step is well matched with AN weight loss, and the second and third steps are well matched with OA degradation temperatures, supporting the claim of OA and AN existing in the final nanocomposite.

The mass percentage of OA for IONPs/OA sample is estimated about 50 % and the residual mass can be attributed to the IONPs that is about 47 %. The mass percentage of OA, IONPs and AN for IONPs/OA/AN/PVA nanocomposite is estimated around 24 %, 27 % and 47%, respectively. In the case of PVA the mass percentage cannot be accurately estimated by the TGA curve of IONPs/OA/AN/PVA nanocomposite because, according to literatures [186, 187], the weight loss of PVA occurs in 230 °C - 430 °C range, which is very close to the degradation temperature of oleic acid. Although we cannot precisely determine the mass percentage of PVA, it is possible to verify that the mass percentage of PVA and oleic acid together is 24%. Once the mass of PVA employed in the synthesis is very low, most of this percentage (24%) is believed to be associated with oleic acid.

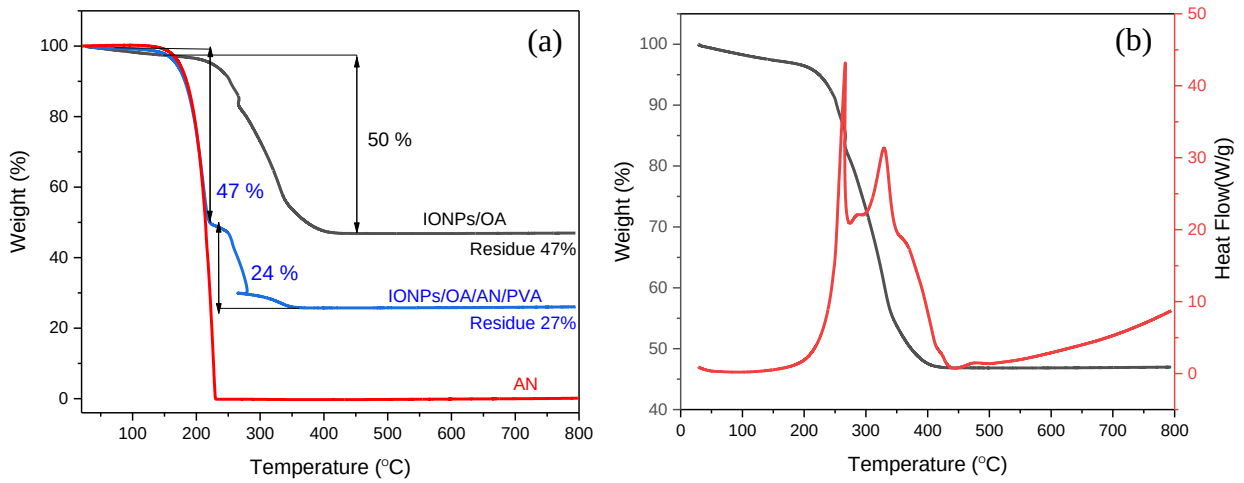

Figure 4. 7 (a) TGA of IONPs/OA, IONPs/OA/AN/PVA and AN and (b) TGA and DSC of IONPs/OA.

4.3.3 Magnetization

Magnetization measurements of IONPs/OA and IONPs/OA/AN/PVA samples are depicted in Figure 4.8. As expected, both samples exhibited superparamagnetic behavior at room temperature without any remanence or coercivity with high saturation magnetization, which is extremely desirable for biomedical applications [132, 188]. The magnetization values for IONPs/OA and IONPs/OA/AN/PVA are about 70 Am^2/kg and 63 Am^2/kg, respectively at 2.0 T.

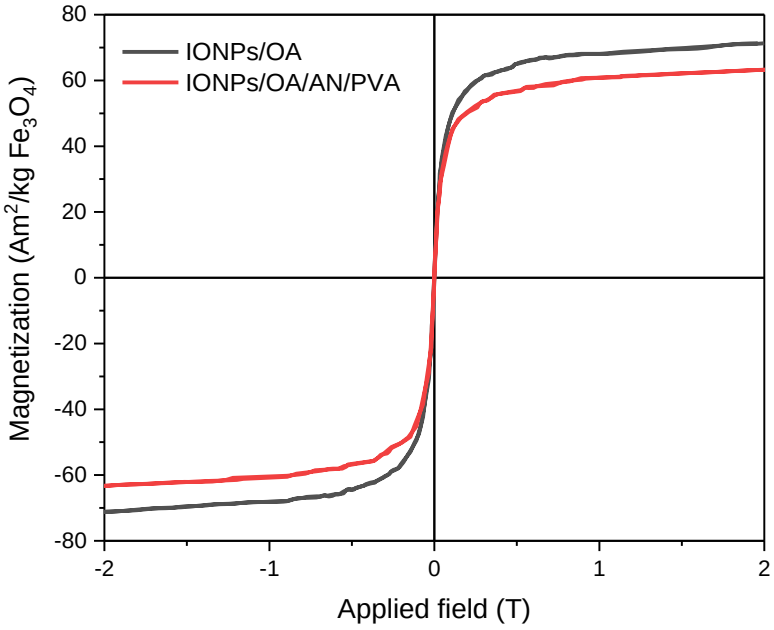

Figure 4. 8 Magnetization curves of IONPs/OA and IONPs/OA/AN/PVA at room temperature.

4.3.4. Fluorescence and luminescence lifetime

The fluorescence emission spectra of the prepared nanocomposites and AN at λ_{ex} = 375 nm are depicted in Figure 4.9. As expected, no fluorescence emission band is detected in IONPs/OA spectrum. However, three strong emission bands and a shoulder in the blue region can be seen for the fluorescence spectrum of AN and IONPs/OA/AN in ethanol. The high fluorescence intensity of IONPs/OA/AN spectrum can suggest that OA coating on IONPs can reduce the interactions between AN and the surface of magnetic core, resulting in decreased energy and electron transfer processes between them and then decreased fluorescence quenching. However, in IONPs/OA/AN/PVA spectrum, a fluorescence quenching can be observed only for the first emission band. This quenching can be caused by the different fluorophore environment (solvents) or due to the electron structure of IONPs/OA/AN/PVA nanocomposite.

Figure 4.10 (a, b) shows the IONPs/OA and IONPs/OA/AN/PVA samples in powder form under ultraviolet light, respectively. The IONPs/OA exposed to UV light does not show any light emission, while the IONPs/OA/AN/PVA nanocomposite shows a strong blue luminescence.

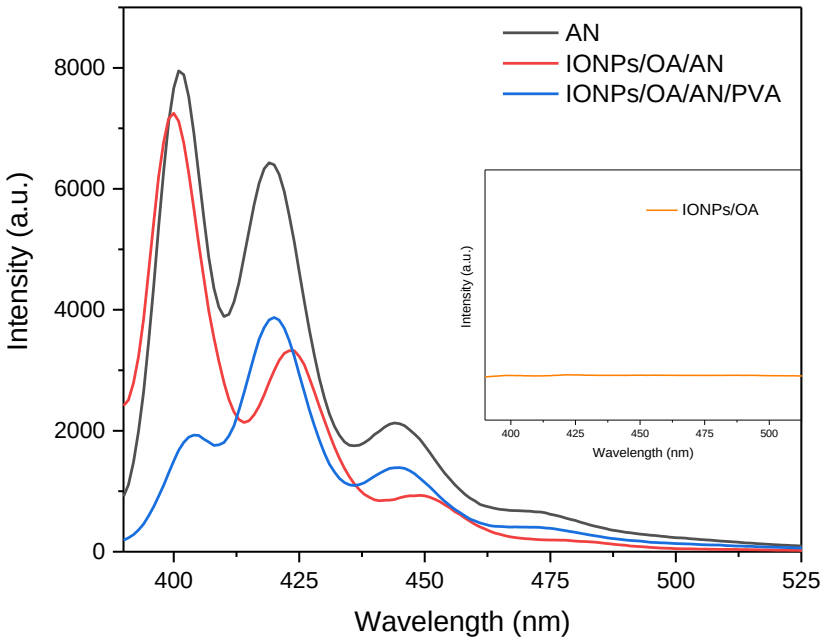

Figure 4. 9 Fluorescence emission spectra of IONPs/OA (inset), IONPs/OA/AN/PVA and AN dispersed in solvent at λ_{ex}= 375 nm.

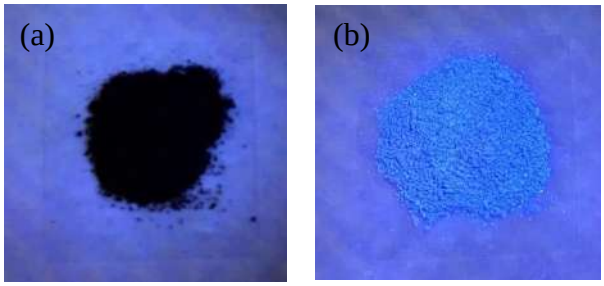

Figure 4. 10 (a) The image of IONPs/OA and (b) IONPs/OA/AN/PVA solid samples exposed to ultraviolet light.

Fluorescence lifetimes of AN and IONPs/OA/AN in ethanol and IONPs/OA/AN/PVA in water were measured (Figure 4.11). It is worth noting that the fluorescence lifetime is influenced by several external factors including polarity, temperature, and the existence of fluorescence quenchers [189], but it does not depend on some factors such as fluorophore concentration, self-absorption, sample thickness, fluorescence intensity, and excitation intensity, for instance [190]. Table 4.1 shows the lifetimes (τ) of IONPs/OA/AN, IONPs/OA/AN/PVA and AN calculated by fitting with Edinburgh Instruments software. The τ of anthracene solution follows the single-

exponential lifetime model, whereas a bi-exponential model better fits the decay curves related to the hybrid particles.

Table 4. 1 Lifetimes of different samples calculated by fitting of Edinburgh instruments software.

Lifetime (ns)	AN	IONPS/OA/AN	IONPS/OA/AN/PVA
τ_1	4.26 (100%)	4.55 (97.57%)	5.66 (48.64%)
τ_2	-	11.74 (2.43%)	2.76 (49.95%)
τ_3	-	-	0.7 (1.41%)

Multi-exponential decay may occur in the case of a mixture of fluorophores in different environments, with each of them undergoing an individual single-exponential decay, for instance when the fluorophore is in the presence of solvents surrounded by one or more polar molecules resulting in a lifetime distribution [191]. One would conclude that there are more than one fluorophore population in IONPS/OA/AN and IONPS/OA/AN/PVA compared with AN because of the lifetime distribution.

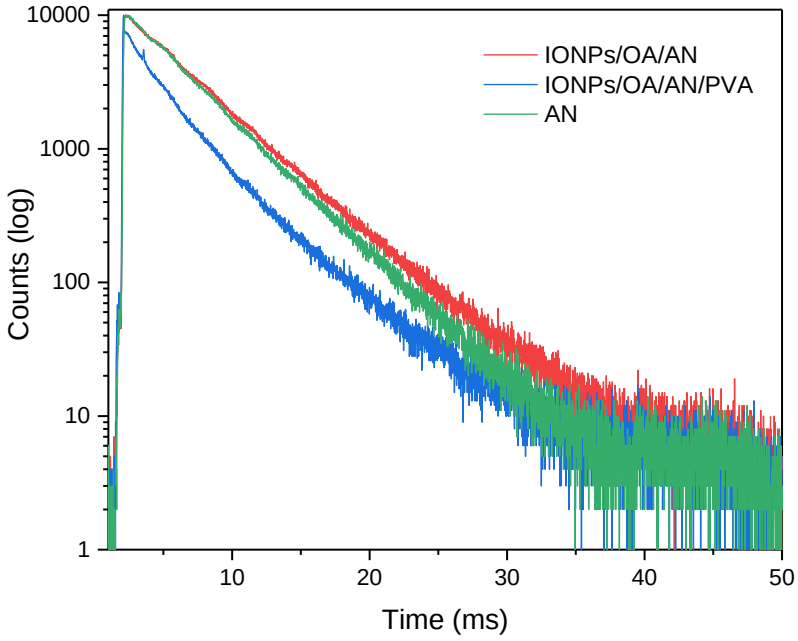

Figure 4. 11 Fluorescence lifetime of IONPs/OA/AN, IONPs/OA/AN/PVA and AN.

The radioluminescence spectra of IONPs/OA/AN/PVA at different currents of X-ray tube are shown in Figure 4.12a. As it can be seen this nanocomposite exposed to X-rays (2 mA to 10 mA) presents radioluminescence emission (Figure 4.12 (a)). Furthermore, a linear increase of the radioluminescence intensity of nanocomposite as a function of the current applied in the X-ray tube (dose rate of X-rays) can be observed (Figure 4.12 (b)), which is highly desirable for biomedical applications [192, 193]. However, the peaks in X-ray luminescence of IONPs/OA/AN/PVA are shifted to red compared to its fluorescence, what is also attractive for biological applications because of the decrease in scattering and longer propagation in biological tissues. These shifts may be due to the environment of the fluorophore and the use of powder samples in X-ray luminescence spectroscopy instead of solution, resulting in the agglomeration of AN in powder sample and leading to shifts in the emission bands.

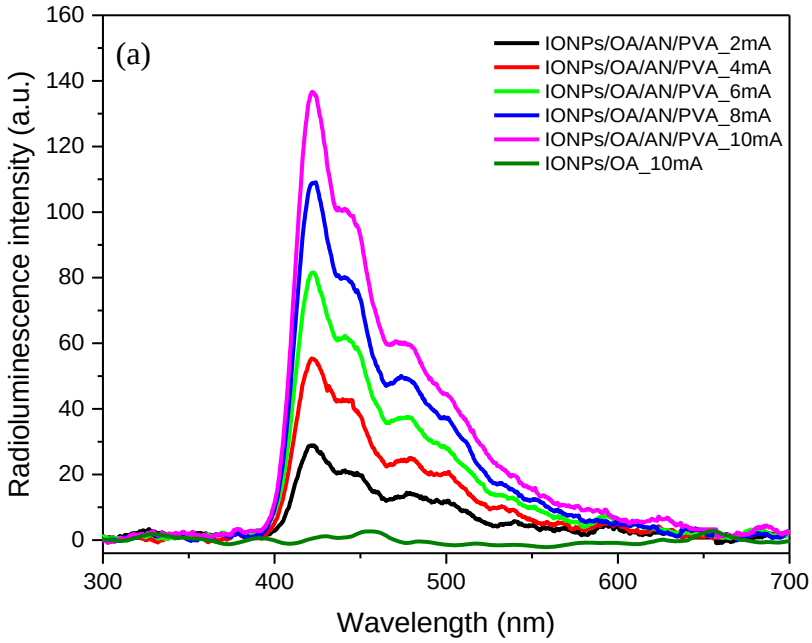

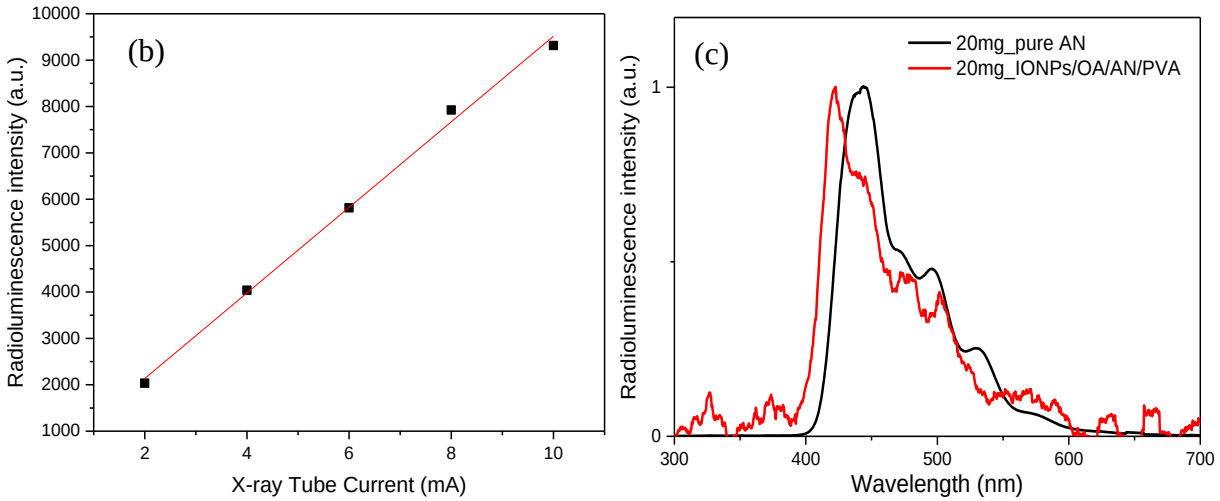

Figure 4. 12 (a) Radioluminescence of IONPs/OA/AN/PVA in different currents applied to the X-ray tube and IONPs/OA in an applied current of 10 mA. (b) Radioluminescence intensity as a function of the tube current reveals linear behavior. (c) Normalized radioluminescence intensity of pure AN and IONPs/OA/AN/PVA.

The normalized radioluminescence intensity of pure AN and IONPs/OA/AN/PVA (20 mg) have been shown in Figure 4.12 (c). IONPs/OA/AN/PVA nanocomposite show a blue shift compared with pure AN. This blue shift can be due to the intermolecular interactions and structural arrangement of this nanocomposite, among other factors [189, 194].

4.4. Summary

In this work, we reported the synthesis of the multifunctional iron oxide nanoparticles with fluorescent and radioluminescent properties for biomedical applications. The IONPs/OA were synthesized by the thermal decomposition method and were functionalized with AN as fluorophore. The IONPs/OA/AN became water dispersible by covering them with PVA. The magnetite phase of the iron oxide cores was confirmed by the XRD and FTIR results. The TEM images demonstrated that magnetic nanoparticles are monodisperse with small core sizes. The magnetization curves showed superparamagnetic behavior of the nanoparticles before and after functionalization with high magnetization values, which is very important for biomedical applications. Furthermore, the IONPs/OA/AN/PVA presented sharp blue emission upon exposure to UV and X-ray with low quenching process. Therefore, this nanocomposite with magnetic, fluorescent and radioluminescent properties can be effectively used in practical applications of biomedicine such as labeling, detection and treatment.

Chapter 5: Magnetic Separation of Iron Oxide Nanoparticles to Improve Their Application for Magnetic Particle Imaging

5.1. Introduction

Over the last decades, medical imaging technologies such as computed tomography (CT), ultrasound imaging, magnetic resonance imaging (MRI), and positron emission tomography (PET) have been playing important roles in clinical diagnosis [147, 195]. Compared to these traditional techniques, magnetic particle imaging (MPI) is a rather young 3D imaging modality with high spatial and high temporal resolution which allows tracking and quantification of magnetic nanoparticle (MNP) tracers such as iron oxide nanoparticles (IONP) [52, 196]. IONP are the most frequently used MNP systems employed in biomedical applications due to their high stability, high biocompatibility and magnetization, and low toxicity [132, 148, 197].

The spatial resolution and sensitivity of the MPI images depend on the applied magnetic field and the properties of the MNP tracers such as the core size, core size distribution, anisotropy of the magnetic core, and surface modification of MNP [196, 198]. Numerical simulations of Yoshida et al.[199] showed that MPI image quality can efficiently be improved by employing MNP with narrow size distribution and small anisotropy energy. In general, size distribution plays an essential role in biomedical applications, especially in vivo, and it is extremely important for evaluation of magnetic properties of MNP [200]. Theoretically, particles with a broader size distribution tend to present a higher aggregation rate rather than those with the same size [19, 201]. Therefore, the large size distribution of MNP can lead to aggregation, resulting in some drawbacks such as changing the magnetic properties of MNP or medical issues (blood clotting, blocking blood vessels and circulation time) [202-204]. Therefore, some techniques are required and applied to reduce the size distribution. So far, several methods have been reported for MNP such as magnetic field flow fractionation filtration [205, 206], separation in electric fields [207] and gradient magnetic separation [208].

Recently, magnetic separation (MS) technique, which commonly is classified into low gradient magnetic separation (LGMS) (<100 T/m) and high gradient magnetic separation (HGMS) (>100 T/m), has gained a great attention in biotechnology applications ranging from wastewater treatments to biomedical applications [209-211]. The motion of MNP in an inhomogeneous magnetic field is known as magnetophoresis and is characterized by the separation time parameter which is determined by the magnetophoretical velocities of the MNP. Generally, magnetophoresis processes are caused by two principal different types: cooperative magnetophoresis which is a quick process enhanced by interactions of particles, and noncooperative magnetophoresis which is a slow process caused by the movement of the individual particles in magnetic fields [212]

the magnetophoresis process depends on several parameters such as core size, core size distribution, zeta potential, shape, magnetic moment and concentration of MNP [211, 213]. Some researchers have been investigating the effect of these parameters on separation time of MNP by magnetophoresis experiments. For instance, Lim et al. studied the effect of MNP shape on separation time, showing that the separation time of nanorods is shorter than of nanospheres [214]. The effect of zeta potential on magnetophoretical behavior was investigated by Benelmekki et al. [213]. They found increased separation times for MNP with higher zeta potential. Furthermore, Cuevas et al. [209] investigated the effect of concentration on separation time for MNP over a few minutes of MS in a homogeneous 30 T/m gradient.

Mostly, inhomogeneous gradients are used in MS techniques. However, in an inhomogeneous magnetic field gradient, the magnetic force on the MNP is different at every point of the system that can lead to an uncontrolled and unrepeatable separation process. The significant advantage of using a homogeneous gradient is that the MNP experience identical magnetic forces everywhere in the system and the separation process is performed under more precisely controlled homogeneous conditions. Therefore, changes in the separation processes can more directly be related to characteristics of MNP and/or sample viscosity. In the present study, we treated the commercial IONP (EMG 700) with MS technique using a homogeneous magnetic field gradient of 15 T/m, to improve their capability for biomedical applications such as MPI tracer. In addition, we investigated the magnetophoretical behavior of IONP at different concentrations in the range 2 to 120 mmol/L over a 24-hour time period. We demonstrate that LGMS is a quick and efficient

technique to narrow the size distribution of MNP in aqueous phase and to improve their magnetic properties for biomedical applications such as MPI.

5.2. Materials and Methods

5.2.1. Materials

In this work, commercial IONP (EMG 700, FerroTec) with 10 nm core size and zeta potential of -34 mV were used. These MNP have a magnetite core (Fe_3O_4) with an anionic surfactant coating. They are currently employed in basic physics and biomedical research. A blue and black liquid ink were used as a control to study the optical dynamic range of the detector of the magnetophoretic system. In this study, the samples were named "EM" followed by their concentration value, for example an EM sample with 8 mmol/L concentration was denoted as "EM8".

5.2.2 Magnetophoresis experiment

The magnetophoresis device to provide a homogeneous magnetic field gradient used in our experiments is the SEPMAG LAB (Sepmag Systems, SL, Barcelona, Spain) with MLAB210 adaptor. It contains of three cylindrical cavities, two of them for 2 mL volume tubes and one for a 15 mL tube. This device is designed to provide a uniform magnetic gradient of 15 T/m to supply uniform magnetophoretic conditions in the cylindrical cavities. The magnetic force experienced by the magnetic particles is given by [215]:

$$F_m = m\mu_0 \frac{\partial H}{\partial r} \tag{5-1}$$

where m is the magnetic moment of the nanoparticle, μ_0 is the magnetic constant, and $\frac{\partial H}{\partial r}$ is the radial magnetic gradient.

The magnetic force causes the particles to move with a magnetophoretical velocity. The velocity of the magnetic particles depends on the balance between the drag force and the applied magnetic force. While the drag force ($F_d = 6\pi r\eta v$) depends on the viscosity of the solution and the radius of the MNP [211], the magnetic force depends on the magnetic moment of the MNP and the gradient of the magnetic field.

The schematic setup and process of the magnetophoresis technique are depicted in Figure 5.1 (a, b), respectively. In this setup the optical measurement direction is perpendicular to the magnetic force direction (Figure 5.1(a)). The MNP in the sample volume move towards the wall of the

sample tube with a certain velocity, changing the transparency of the detection area of the light sensor over time (Figure 1(b)). The half separation time (t_{50}) and slope (defined by the dimensionless exponent "p") of magnetophoresis curves were calculated by fitting a logistic function ($y = A_2 + \frac{(A_1 - A_2)}{(1 + {}^{x}/_{x_0})^{p}}$) to the measurement data.

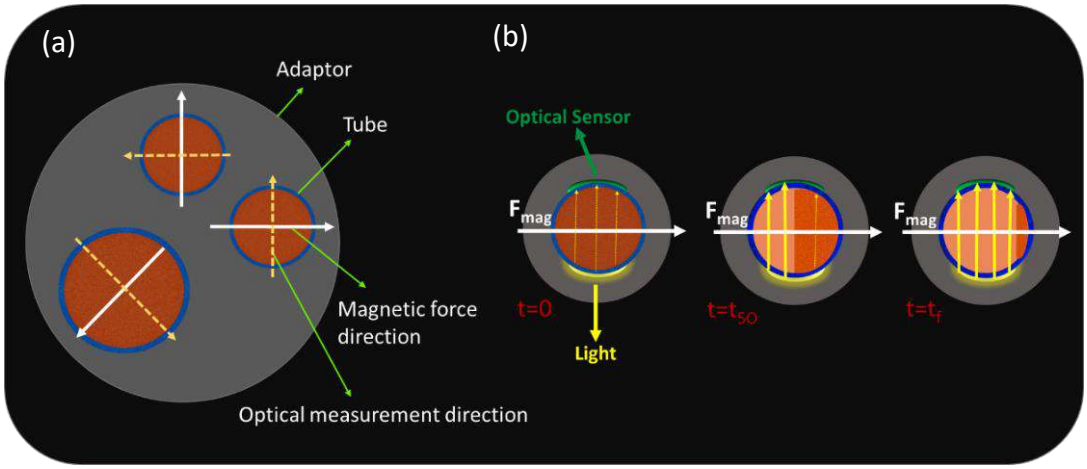

Figure 5. 1 (a) Schematic setup of magnetophoresis device (top view) contains three cylindrical cavities, two of them for 2 mL volume tubes and one for 15 mL tube. (b) The MS process for one tube is illustrated. Showing a hypothetical solution with a homogeneous distribution of MNP at the beginning of the separation process (t = 0), at the intermediate stage ($t = t_{50}$) and the final one ($t = t_f$) where the MNP have been moved towards the tube wall indicated by the orange coloring.

5.2.3 DLS

Hydrodynamic size (d_h) and polydispersity index (PDI) of MNP were determined by Dynamic Light Scattering (DLS) using a Zetasizer system (Malvern Instruments, UK). The device is equipped with a He/Ne laser with a wavelength of 632.8 nm illuminating the sample. The scattered light is detected at a scattering angle of 173°. All measurements were performed at T = 20 °C. The d_h values are reported as intensity weighted average diameters.

5.2.4 ACS

AC susceptibility (ACS) measurements were performed to determine particle cluster sizes and as a magnetic probe of the agglomeration of MNP using a Dynomag system (Rise Acreo, Sweden) [216]. In this method, the real part (in-phase component) χ' and imaginary part (out-of-phase component) χ'' of the linear magnetic susceptibility are measured at excitation frequencies in the

range 1 Hz – 500 kHz. All measurements were performed at 25 °C on MNP suspensions with a volume of 100 µL. By fitting the experimental data to a Debye model (multi-core model), which has been written in detail in reference [217], d_h and size distribution (σ) of MNP clusters were determined.

5.2.5 MPS

The non-linear dynamic magnetization response of MNP was measured by a Magnetic Particle Spectroscopy (MPS) device (MPS-3, Bruker Biospin, Germany) [54]. The device consists of a drive field coil and a receiving pick-up coil surrounded by an electromagnetic shielding. For measurements, we used a 30 µL sample volume filled into a PCR tube placed in the pick-up coil system of the device. The non-linear magnetic response of MNP was recorded at a drive field amplitude of 25 mT and (fixed) excitation frequency (f_{excite} = 25 kHz) at 37 °C. After filtering to suppress the excitation signal and Fourier transform the MPS spectrum of MNP shows amplitudes at odd multiples of the excitation frequency (A_i with i = 3, 5, 7, etc.). We used the third harmonic amplitude normalized to the iron amount (A_3^*) and the harmonic ratio A_5/A_3 as an indicator for the slope of the spectrum.

5.2.6 MPI

Magnetic particle imaging (MPI) measurements were performed using a preclinical 3D-MPI system (Bruker BioSpin GmbH, Ettlingen, Germany) working at excitation frequencies of 25 kHz, amplitudes of 12 mT in three orthogonal dimensions (x,y,z) and a selection gradient of 2.5 T/m in z-direction and 1.25 T/m in x- and y-directions). Image reconstructions were performed based on the system function (SF) approach using a small (point-like) reference sample measured with identical parameters for all MNP systems. To compare MPI resolution for samples before and after MS, we applied 200 μL of EM15 and EM120 samples after 4 min of MS in a phantom consisting of a spiral channel with a quadratic cross-section of 2x2 mm in a plastic carrier [218]. The concentrations of EM15 and EM120 samples after 4 min of separation were determined by phenanthroline spectrophotometric iron quantification assay about 10 and 55 mmol/L, respectively. Therefore, we diluted EM15 and EM120 samples to the same concentration (10 and 55 mmol/L), without inserting in the MS system, compared to the samples after MS and applied them in the MPI measurements. Four SFs of the tracer were recorded, before and after the MS and for 10 and 55 mmol/L. Image reconstructions with a field of view of 25x25x13 voxels (mm^3)

was performed using a signal-to-noise-ratio (SNR) ≥ 4, 20 Kaczmarz-iterations, and a regularization parameter $\lambda=10^{-5}$.

5.3. Results and Discussions

The reproducibility of the separation runs was investigated by recording the magnetophoresis curves of four EM samples with the same concentration of 8 mmol/L (EM8) for 3000 s (Figure 5.2 (a)). The mean t_{50} and p of these curves were 81(1) s and 3(6), respectively. As can be seen, the relative standard deviations of both values of about 2% underline the high reproducibility and stable operation conditions of the separation system.

Furthermore, the reversibility of magnetophoresis process was studied by recording eight times the magnetophoresis curve of one identical EM sample with a concentration of 15 mmol/L (EM15) for 500 s. Note, that after each measurement the sample was properly mixed using a vortex mixer. In Figure 5.2 (b) the recorded curves of the eight measurements show no significant changes in amplitude and shape. The average t_{50} and p of the curves were 66(2) s and 2.8(3), respectively. Therefore, magnetophoresis process can be considered as a reversible process.

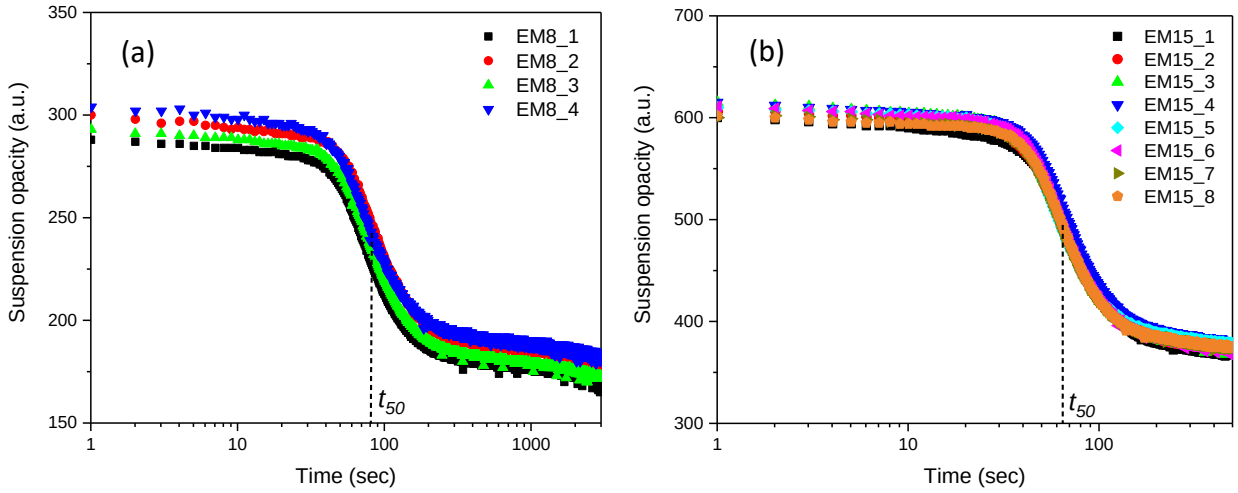

Figure 5. 2 (a) Reproducibility of LGMS: four different samples of 8 mmol/L concentration (EM8), and (b) the subsequent repetitions of the magnetophoresis experiments for one identical sample with 15 mmol/L concentration (EM15).

The magnetophoretical behavior of a sample with 10 mmol/L concentration (EM10) was studied over a 14 h time period (Figure 5.3 (a)). The magnetophoresis curve of this sample consists of two distinct steps which are ascribed to the extraction of MNP with different sizes. To clarify this, we

determined d_h and PDI by DLS for the EM10 sample material, which was taken about 200 μL from the center of the Eppendorf, at defined time points during the separation run. Figure 5.3 (b) shows the DLS curves of the EM10 before applying the magnetic field gradient (time point t_0), e.g. before introducing the sample into the separation device, t_1=3 min shortly after the first step, t_2 =50 min, and t_3 =3 h during the second step.

As it can be seen in Table 5.1 the d_h and PDI significantly changes (about 45%) from t_0 to t_1, while a slight difference is observed in the PDI for time points later than t_1. These results strongly suggest that the MS removes magnetic entities of different sizes. First, larger MNP or MNP agglomerates are removed. Due to their larger magnetic moment they are pushed with stronger attractive forces. Furthermore, these larger MNP could tend to form fast moving aggregates (e.g. chains), which result in a smaller d_h and PDI after t_1 as well. After accumulation of those MNP at the Eppendorf wall, smaller MNP, are more slowly moved towards the wall and they lead to the second accumulation.

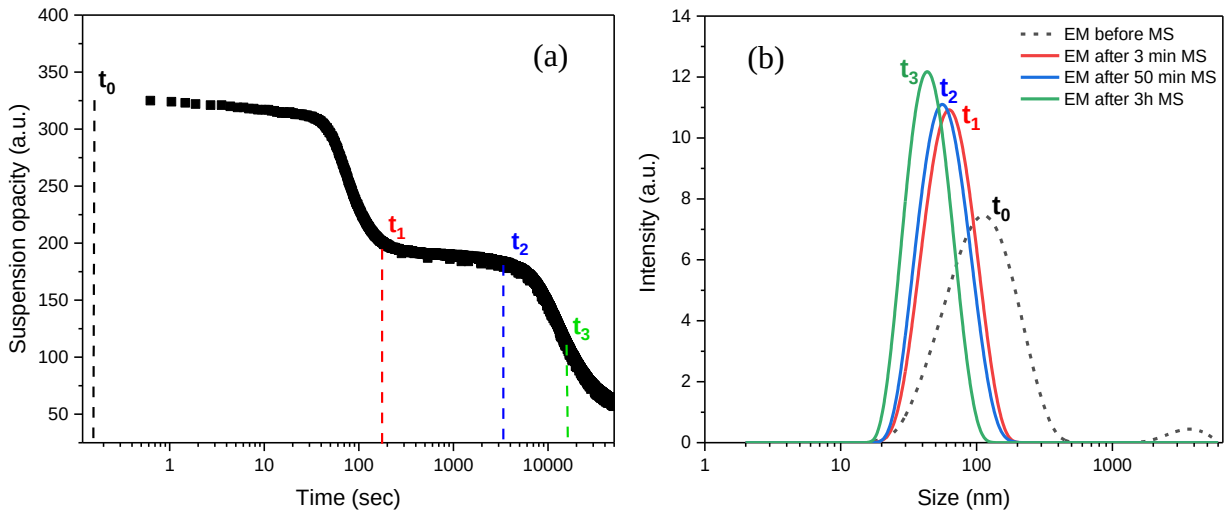

Figure 5. 3 (a) The magnetophoresis curve of EM10 over a 14 h time period, and (b) DLS of EM10 sample at t_0 before separation, t_1 after 3 min, t_2 after 50 min, and t_3 after 3h of inserting sample in separation system.

Furthermore, we used ACS as a magnetic probe to determine the agglomeration of MNP. The real part (χ') and imaginary part (χ'') of the ACS versus excitation frequency for EM10 sample at different points of time during the separation process were shown in Figure 5.4 (a, b). The signal in both χ' and χ''decrease with increasing separation time up to 3 h. Furthermore, there is a clear

frequency shift of the maxima of χ'and χ''components in all samples, starting with an EM sample before MS and followed by a significant shift after 3 min, 50 min and 3 h of MS. Figure 5.4b shows that the χ'' peak shifts towards higher frequencies after 3 h of separation which indicates a reduction of the MNP size.

Table 5.1 shows the d_h and size distribution (σ) considerably reduced after 3 min of separation, while minor differences can be observed afterwards (50 min, 3 h). That can suggest the elimination of agglomerated MNP from the suspension after 3 min of MS for this sample. These results confirm the DLS results, however the d_h measured by DLS is larger compared to the ACS result. Note that the DLS scattering intensity depends on the 6th power of the particle size leading to an over-interpretation of the average size especially in heterogeneous samples.

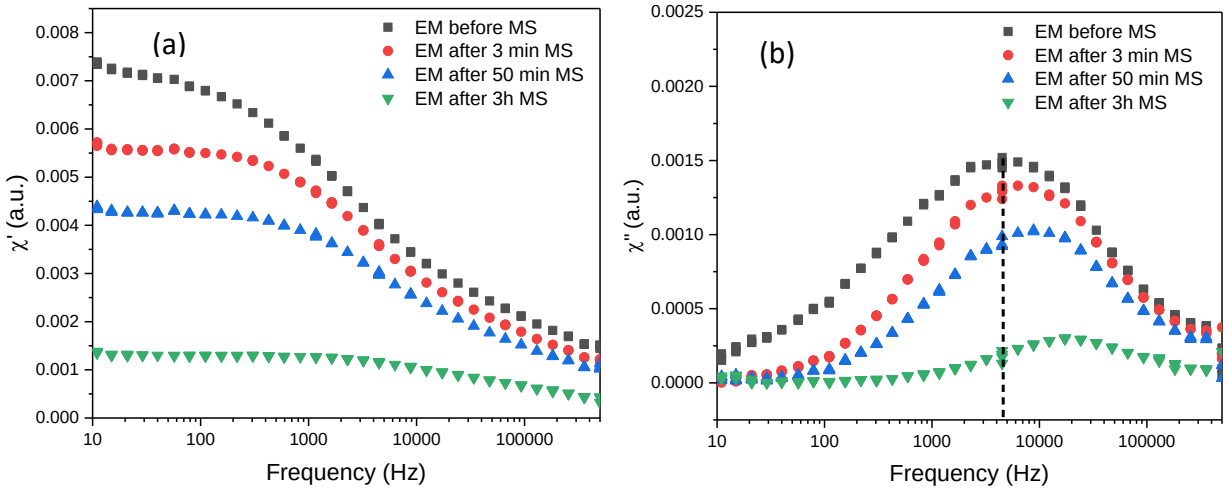

Figure 5. 4 (a, b) χ' and χ'' of ACS versus excitation frequency of EM10 sample before introducing the sample in separation system, after 3 min, 50 min, and 3 h of inserting sample in separation system. The vertical black line marks the peak position of χ'' of the sample before MS to better visualize the peak shift during the MS run.

The nonlinear magnetic susceptibility of EM10, before and after MS, was measured by MPS to study the magnetization properties of this sample during the MS process. All measurements were recorded at a drive field with an amplitude of 25 mT and at a 25 kHz fixed excitation frequency. The third harmonic amplitude normalized to the iron amount (A_3^*) and harmonic ratio (A_5/A_3) of MPS signal versus separation time have shown in Figure 5.5 (a, b), respectively. Table 5.1 shows that the parameters A_3^* and A_5/A_3improve about 35% and 11%, respectively, after up to 3 h of

separation. Improving the MPS signal by separation time can be due to the removal of agglomerated MNP from the suspension and narrowing the magnetic moment distribution. Therefore, time-controlled separation of MNP can be used to adjust size distribution and magnetic properties of MNP samples for the desired biomedical application (e.g. MPI) in a controlled manner.

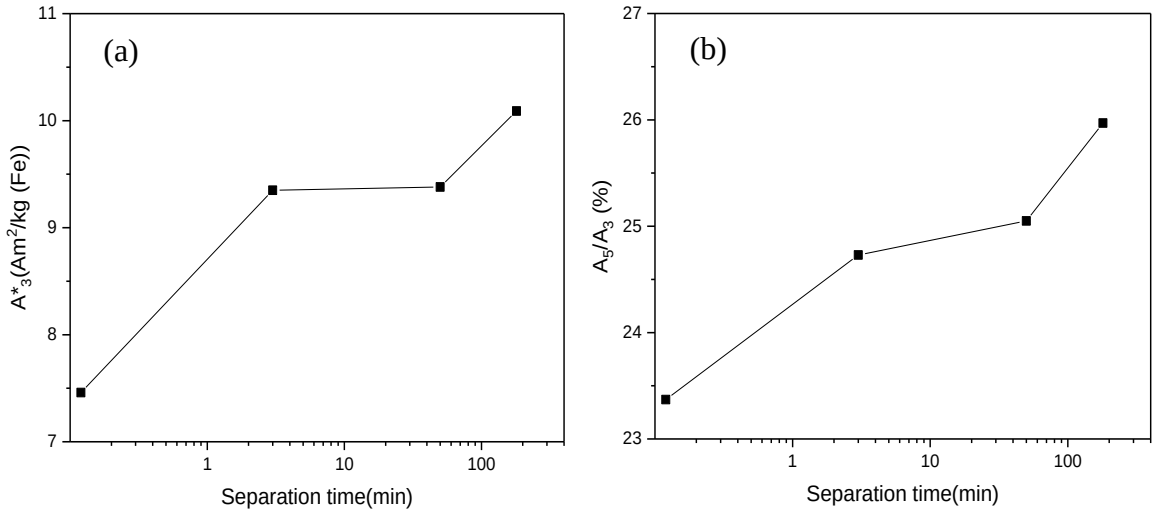

Figure 5. 5 Variation of (a) A_3^*, and (b) A_5/A_3 MPS parameters for EM10 sample during 3 h of separation time.

Table 5. 1 The characteristics of the EM10 sample before MS and during 3 h of MS by DLS, ACS and MPS.

Sample EM10	d_h **DLS (nm)**	**PDI DLS**	d_h **ACS (nm)**	σ **ACS**	A_3^* **(Am²/kg (Fe))**	A_5/A_3 **(%)**
Before MS (t_0)	113	0.25	50.0	2.16	7.46	23.37
After 3min MS (t_1)	62	0.14	40.7	1.79	9.35	24.73
After 50min MS (t_2)	56	0.13	37.5	1.75	9.38	25.05
After 3h MS (t_3)	44	0.11	26.5	1.75	10.09	25.97

In addition, the magnetophoretical behavior of EM samples with different concentrations of MNP was studied for 24 h separation. The magnetophoresis curves were shown in Figure 5.6 (a) for samples with concentrations ranging from 2 to 120 mmol/L. Figure 6b shows the primary opacity samples increase by increasing the concentration of MNP up to 15 mmol/L, then for higher

concentrations it does not considerably change and the first step disappeared (Figure 5.6 (a)), that can be attributed to the opacity saturation for high concentrated sample. To verify this, we recorded the primary opacity of two colors of inks such as black and blue with increasing percentage of concentration (0.1 to 100, v/v). The results (Figure 5.6 (c)) show that opacity gets saturated for samples at high ink concentrations, confirming the saturated opacity for EM samples with high concentrations of MNP. Therefore, it can be concluded that the photo diode is not capable of resolving the concentration change occurring during the removal of larger entities, resulting in the observed disappearance of the first accumulation for the higher concentrated samples.

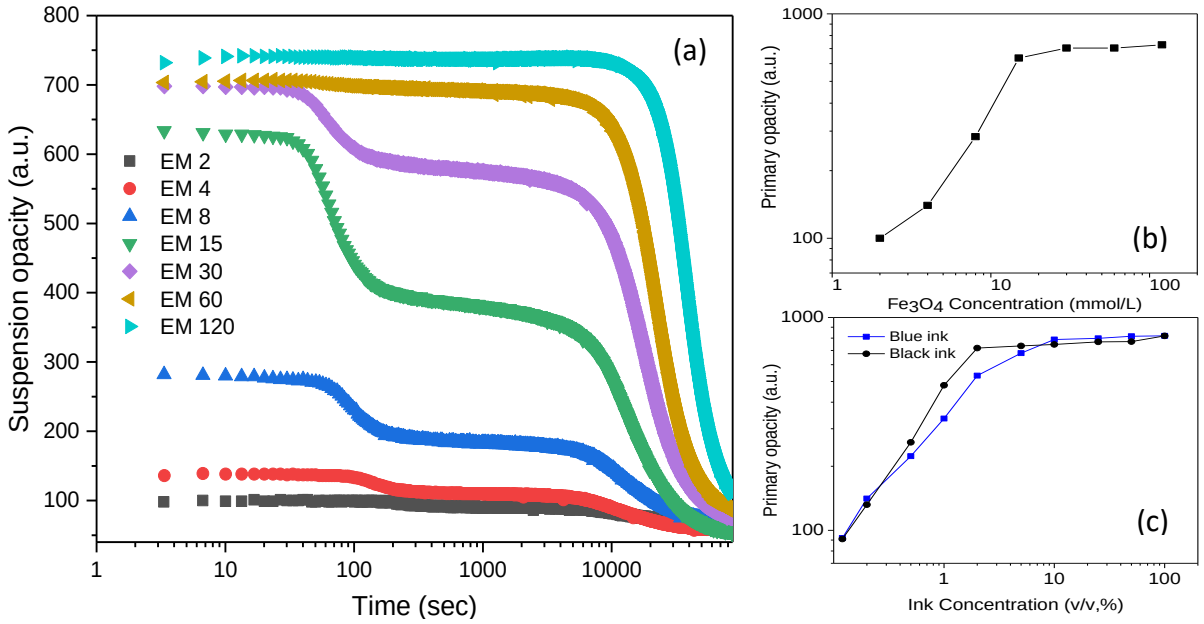

Figure 5. 6 (a) The magnetophoresis curve of EM samples in different concentrations ranging from 2 to 120 mmol/L for 24 h in a 15 T/m gradient field, and (b, c) the primary opacity as a function of MNP and ink concentration, respectively.

To study the effect of concentration on the separation of agglomerated MNP in suspension during the MS process we determined d_h and PDI of the EM samples by DLS for the time point t=4 min of MS (Figure 5.7 (a)). As mentioned before, we ascribe this first accumulation to be caused by agglomerated MNP occurring within the first 4 min of separation (Figure 5.6 (a)). For the sample with the lowest concentration, EM2, no significant accumulation was observed that can be due to the low number of MNP in suspension which results in lower interactions of MNP with neighbors and does not form chains or aggregates. Therefore, a slower separation process will occur.

Figure 5.7 (b, c) shows that both d_h and PDI of the samples significantly decrease with regard to their MNP concentration within the first 4 min of MS. Increasing the concentrations of MNP in suspension leads to an increase of the interactions between MNP and making longer chains and aggregations. Therefore, agglomerated MNP which possess larger size and magnetic moment move faster towards the Eppendorf wall [209], whereby smaller particles with smaller d_h and PDI remain in the Eppendorf center.

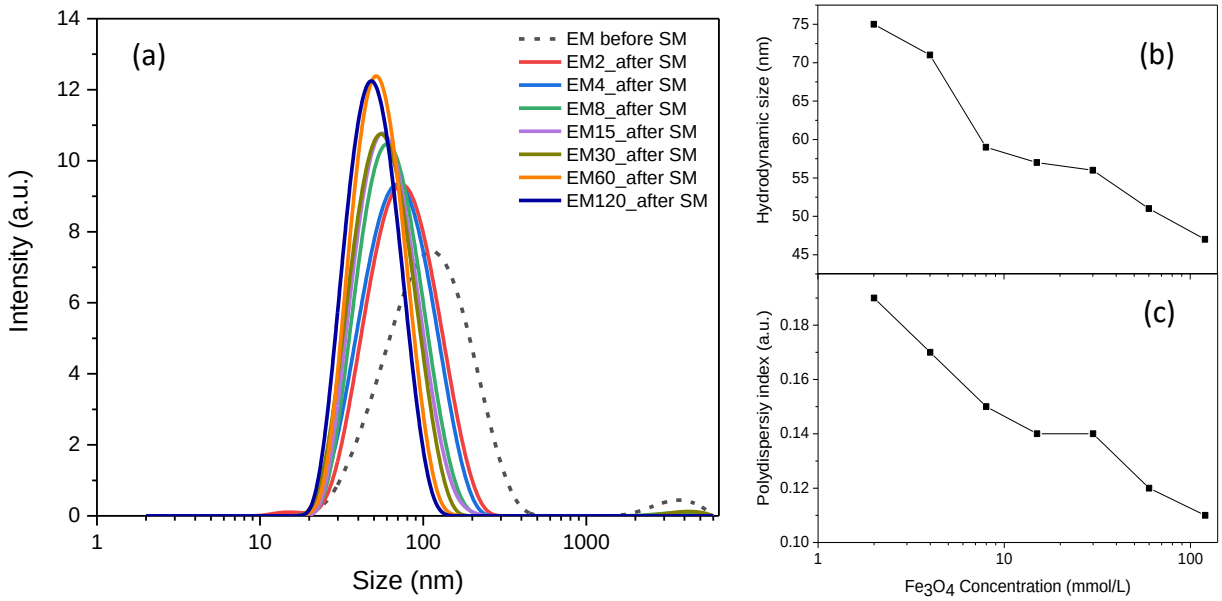

Figure 5. 7 (a) DLS measurements of samples before and 4 min after MS, and (b, c) d_h and PDI of samples 4 min after MS.

Since MPS is based on the same physical principle as MPI, it is a suitable technique for tracer evaluation [208]. The A_3^* and A_5/A_3 parameters of each sample were determined 4 min after MS to evaluate them as tracers. The results show the improvement of both A_3^* and A_5/A_3 by increasing the concentration of MNP in suspension. Therefore, it can be concluded that the separation process is more effective and quicker for samples with high concentrations and that these samples after a short separation time can be considered as more efficient MPI tracers compared to the non-separated ones. Table 5.2 summarizes parameters extracted from DLS and MPS measurements for EM samples extracted 4 min after MS.

Table 5. 2 DLS and MPS measurements of all EM samples after 4 min of MS.

Samples	h_d (DLS) (nm)	PDI (DLS) (nm)	A_3^* (Am^2/kg (Fe))	A_5/A_3 (%)
EM2	75	0.19	8.38	24.21
EM4	71	0.17	8.60	24.20
EM8	59	0.15	8.72	24.41
EM15	57	0.14	9.21	24.77
EM30	56	0.14	10.19	25.21
EM60	51	0.12	10.38	25.57
EM120	47	0.11	10.59	26.60

Reconstructed MPI images of EM15 and EM120 samples after 4 min of separation with 10 and 55 mmol/L concentrations, respectively, and EM samples without applying separation diluted to the same concentration are shown in Figure 5.8. For both concentrations a higher MPI image resolution was obtained compared to the respective sample before MS.

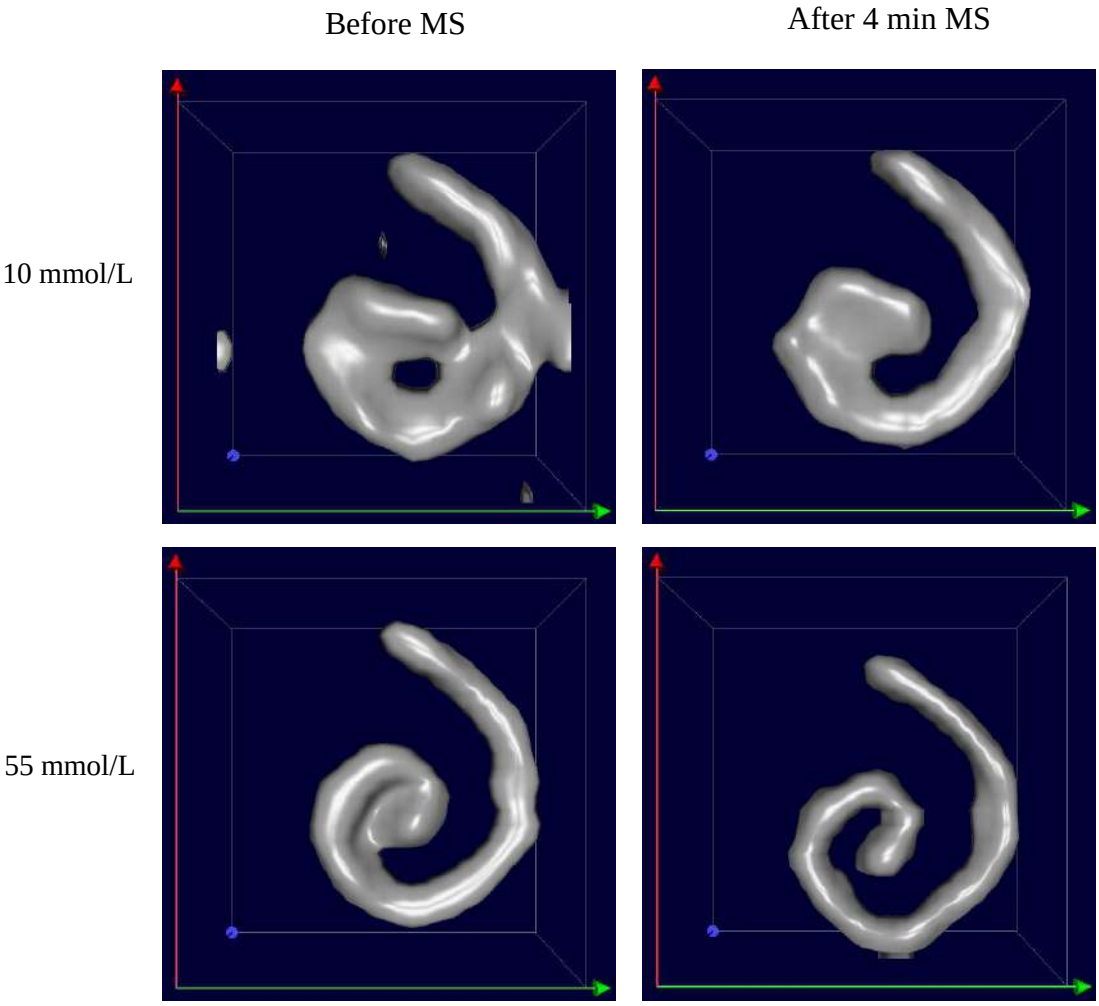

Figure 5. 8 Reconstructed MPI images of phantoms using 10 and 55 mmol/L of EM samples before and after MS.

We observe this benefit of MS already during the image reconstructions by the number of usable frequency components selected by the SNR ≥ 4. The MS improves the SNR of the recorded SFs and in this matter the number of usable frequency components for the image reconstruction is increased, see Table 5.3. The image reconstruction results in better resolution and less artefacts by the increased SNR in the MPI signal.

Table 5. 3 Selected frequency components for image reconstruction by the SNR ≥ 4

Usable frequency components	**Before MS**	**After MS**
10 mmol/L	337	424
55 mmol/L	998	1253

5.4. Summary

In this work we employed commercial IONP (EM) in aqueous phase for low gradient magnetic separation (LGMS) (<15 T/m) to improve their performance as MPI tracer. We demonstrated that the LGMS technique is capable of separating larger MNP entities from the suspension in a short period of time which allowed us to adjust the size distribution and magnetic properties of MNP via time-controlled magnetic separation. Finally, EM samples after LGMS showed higher image resolution in MPI compared to the sample in initial state. Therefore, it can be concluded that the LGMS method is an efficient, reproducible and fast method for MNP size selection and capable of adjusting the functional properties of MNP for biomedical applications.

Chapter 6: Conclusion and Future Works

This thesis presents the synthesis and characterization of iron oxide nanoparticles (IONPs) for biomedical applications. In this thesis, two different chemical methods were used for synthesis of (IONPs). The first method was green synthesis with a simple and cost effective co-precipitation. In this method natural rubber latex was used as the covering agent of MNPs. The prepared MNPs coated with natural rubber latex showed superparamagnetic behavior at room temperature and the magnetic characterization of the NRL-MNPs indicated that by covering MNPs with NRL and increasing the NRL concentration in synthesis process, the saturation magnetization of MNPs can significantly enhance. This property of NRL makes it so interesting as covering agents because it can not only improve the biocompatibility of MNPs but also enhance the saturation magnetization of MNPs that are two essential factors for biomedical applications. The prepared samples were evaluated as contrast agent for magnetic resonance imaging in phantom studies. The results demonstrated that the relaxivity ratio r2/r1 strongly depends on NRL shell thickness and increasing shell thickness or hydrodynamic size lead to decreasing the relaxivity ratio. Therefore, by adjusting the NRL concentration we can control the relaxivity ratio based on the type of diagnosis and diseases.

The second group of the iron oxide nanoparticles was synthesized by the thermal decomposition method, coated by oleic acid and modified by anthracene as a covering agent and fluorophore, respectively. The final nanocomposite was covered by polyvinyl alcohol in order to disperse it in aqueous phase to be usable in biomedical applications. To our knowledge, for the first time we synthesized multifunctional superparamagnetic iron oxide nanoparticles with high magnetic, fluorescent and radio-luminescent properties that can be extremely desirable for cancer diagnosis and therapy. In addition, a linear increase of the radio-luminescence intensity of this multifunctional nanocomposite as a function of the current applied in the X-ray tube was observed that is highly desired for biomedical applications.

Finally, we optimized the iron oxide nanoparticles coated with anionic surfactants using magnetic separation technique, by a low gradient magnetic separation (LGMS) (<15 T/m) method, to improve their performance as MPI tracers. The samples with different concentrations of magnetite (Fe_3O_4) nanoparticles were imaged in a preclinical MPI scanner, before and after magnetophoresis process. The images of the samples after separation process showed higher MPI resolution. Furthermore, we demonstrated that the LGMS technique is capable of separating larger MNP entities from the suspension in a short period of time which allowed us to adjust the size distribution and magnetic properties of MNP via time-controlled magnetic separation. Therefore, LGMS can be considered as a valuable, reproducible and fast method to narrow and control the size distribution of MNP for MPI and in vivo biomedical applications.

A proposal for future work based on the obtained results can be divided in three categories:

- The NRL coated MNPs can be applied in hyperthermia, due to their high magnetization, and the effect of NRL in heating process can be studied. In addition, these MNPs due to the high biocompatibility can be used in vivo in MRI and hyperthermia application.
- The multifunctional superparamagnetic nanoparticles with fluorescence and radio-luminescence properties can be used for photodynamic therapy to treat superficial cancer cells such as melanoma. Furthermore, we can replace anthracene with another organic molecular that have emission bands in near-infrared (NIR) in order to improve the diagnosis and treatment of cancer cells that localized in deeper part of the body.
- We can apply the purified MNPs by magnetic separation method as contrast agents for another imaging modality such as ultrasound and MRI to study the effect of size distribution of MNPs on their image resolution.

References

1. Sellmyer, D.J. and R. Skomski, *Advanced magnetic nanostructures*. 2006: Springer Science & Business Media.
2. Affronte, M., *Molecular nanomagnets for information technologies.* Journal of Materials Chemistry, 2009. **19**(12): p. 1731-1737.
3. Enterkin, J.A., K.R. Poeppelmeier, and L.D. Marks, *Oriented catalytic platinum nanoparticles on high surface area strontium titanate nanocuboids.* Nano letters, 2011. **11**(3): p. 993-997.
4. Galvis, H.M.T., et al., *Supported iron nanoparticles as catalysts for sustainable production of lower olefins.* Science, 2012. **335**(6070): p. 835-838.
5. Collins, P.G., et al., *Extreme oxygen sensitivity of electronic properties of carbon nanotubes.* science, 2000. **287**(5459): p. 1801-1804.
6. Ansari, A.A., et al., *Prospects of nanotechnology in clinical immunodiagnostics.* Sensors, 2010. **10**(7): p. 6535-6581.
7. Dingman, J., *Guest Commentary: Nanotechnology: Its Impact on Food Safety.* Journal of Environmental Health, 2008. **70**(6): p. 47-50.
8. Hillie, T. and M. Hlophe, *Nanotechnology and the challenge of clean water.* Nature nanotechnology, 2007. **2**(11): p. 663.
9. Farokhzad, O.C. and R. Langer, *Impact of nanotechnology on drug delivery.* ACS nano, 2009. **3**(1): p. 16-20.
10. Yang, H., et al., *Targeted dual-contrast T1-and T2-weighted magnetic resonance imaging of tumors using multifunctional gadolinium-labeled superparamagnetic iron oxide nanoparticles.* Biomaterials, 2011. **32**(20): p. 4584-4593.
11. Wadas, T.J., et al., *Targeting the αvβ3 integrin for small-animal PET/CT of osteolytic bone metastases.* Journal of Nuclear Medicine, 2009. **50**(11): p. 1873-1880.
12. Haubner, R. and C. Decristoforo, *Radiolabelled RGD peptides and peptidomimetics for tumour targeting.* Front Biosci, 2009. **14**(87286.20).
13. Borden, M.A., et al., *A stimulus-responsive contrast agent for ultrasound molecular imaging.* Biomaterials, 2008. **29**(5): p. 597-606.
14. Welsher, K., et al., *A route to brightly fluorescent carbon nanotubes for near-infrared imaging in mice.* Nature nanotechnology, 2009. **4**(11): p. 773.
15. Yu, E.Y., et al., *Magnetic particle imaging: a novel in vivo imaging platform for cancer detection.* Nano letters, 2017. **17**(3): p. 1648-1654.
16. Zhang, L., et al., *Imaging and cell targeting characteristics of magnetic nanoparticles modified by a functionalizable zwitterionic polymer with adhesive 3, 4-dihydroxyphenyl-l-alanine linkages.* Biomaterials, 2010. **31**(25): p. 6582-6588.
17. Lee, J.H., et al., *All-in-one target-cell-specific magnetic nanoparticles for simultaneous molecular imaging and siRNA delivery.* Angewandte Chemie, 2009. **121**(23): p. 4238-4243.
18. Shen, Z., A. Wu, and X. Chen, *Iron oxide nanoparticle based contrast agents for magnetic resonance imaging.* Molecular pharmaceutics, 2016. **14**(5): p. 1352-1364.
19. Mohammed, L., et al., *Magnetic nanoparticles for environmental and biomedical applications: A review.* Particuology, 2017. **30**: p. 1-14.

20. Goodarz Naseri, M., E.B. Saion, and A. Kamali, *An overview on nanocrystalline ZnFe 2 O 4, MnFe 2 O 4, and CoFe 2 O 4 synthesized by a thermal treatment method.* ISRN Nanotechnology, 2012. **2012**.
21. Corsi, F., et al., *Towards ideal magnetofluorescent nanoparticles for bimodal detection of breast-cancer cells.* Small, 2009. **5**(22): p. 2555-2564.
22. Lininger, C.N., et al., *Energetics of Lithium Insertion into Magnetite, Defective Magnetite, and Maghemite.* Chemistry of Materials, 2018. **30**(21): p. 7922-7937.
23. Friák, M., A. Schindlmayr, and M. Scheffler, *Ab initio study of the half-metal to metal transition in strained magnetite.* New journal of physics, 2007. **9**(1): p. 5.
24. Albanese, A., P.S. Tang, and W.C. Chan, *The effect of nanoparticle size, shape, and surface chemistry on biological systems.* Annual review of biomedical engineering, 2012. **14**: p. 1-16.
25. Arruebo, M., et al., *Magnetic nanoparticles for drug delivery.* Nano today, 2007. **2**(3): p. 22-32.
26. Bedanta, S., et al., *Magnetic nanoparticles: a subject for both fundamental research and applications.* Journal of nanomaterials, 2013. **2013**.
27. Mohapatra, J., M. Xing, and J.P. Liu, *Inductive Thermal Effect of Ferrite Magnetic Nanoparticles.* Materials, 2019. **12**(19): p. 3208.
28. Morrish, A.H., *The physical principles of magnetism.* The Physical Principles of Magnetism, by Allan H. Morrish, pp. 696. ISBN 0-7803-6029-X. Wiley-VCH, January 2001., 2001: p. 696.
29. Yahya, M., F. Hosni, and A.H. Hamzaoui, *Synthesis and ESR Study of Transition from Ferromagnetism to Superparamagnetism In La 0.8 Sr 0.2 MnO 3 Nanomanganite*, in *Nanosystems*. 2019, IntechOpen.
30. Montazer, M. and T. Harifi, *Nanofinishing of Textile Materials*. 2018: Woodhead Publishing.
31. Wu, W., Q. He, and C. Jiang, *Magnetic iron oxide nanoparticles: synthesis and surface functionalization strategies.* Nanoscale research letters, 2008. **3**(11): p. 397.
32. Assa, F., et al., *A biotechnological perspective on the application of iron oxide nanoparticles.* Nano Research, 2016. **9**(8): p. 2203-2225.
33. Banerjee, T., et al., *Preparation, characterization and biodistribution of ultrafine chitosan nanoparticles.* International journal of pharmaceutics, 2002. **243**(1-2): p. 93-105.
34. Moghimi, S.M., A.C. Hunter, and J.C. Murray, *Long-circulating and target-specific nanoparticles: theory to practice.* Pharmacological reviews, 2001. **53**(2): p. 283-318.
35. Park, Y.C., et al., *Effect of PEG molecular weight on stability, T2 contrast, cytotoxicity, and cellular uptake of superparamagnetic iron oxide nanoparticles (SPIONs).* Colloids and surfaces B: Biointerfaces, 2014. **119**: p. 106-114.
36. Wu, W., et al., *Recent progress on magnetic iron oxide nanoparticles: synthesis, surface functional strategies and biomedical applications.* Science and technology of advanced materials, 2015. **16**(2): p. 023501.
37. Huang, K.-S., et al., *Antimicrobial applications of water-dispersible magnetic nanoparticles in biomedicine.* Current medicinal chemistry, 2014. **21**(29): p. 3312-3322.
38. Lin, M.M., et al., *Development of superparamagnetic iron oxide nanoparticles (SPIONS) for translation to clinical applications.* IEEE transactions on Nanobioscience, 2008. **7**(4): p. 298-305.

39. Drmota, A., et al., *Microemulsion method for synthesis of magnetic oxide nanoparticles*, in *Microemulsions-an introduction to properties and applications*. 2012, IntechOpen.
40. Levy, L., et al., *Nanochemistry: synthesis and characterization of multifunctional nanoclinics for biological applications.* Chemistry of Materials, 2002. **14**(9): p. 3715-3721.
41. Unsoy, G., et al., *Magnetite: From synthesis to applications.* Current topics in medicinal chemistry, 2015. **15**(16): p. 1622-1640.
42. Dadfar, S.M., et al., *Iron oxide nanoparticles: Diagnostic, therapeutic and theranostic applications.* Advanced drug delivery reviews, 2019. **138**: p. 302-325.
43. Rockenberger, J., E.C. Scher, and A.P. Alivisatos, *A new nonhydrolytic single-precursor approach to surfactant-capped nanocrystals of transition metal oxides.* Journal of the American Chemical Society, 1999. **121**(49): p. 11595-11596.
44. Sun, S., et al., *Monodisperse mfe2o4 (m= fe, co, mn) nanoparticles.* Journal of the American Chemical Society, 2004. **126**(1): p. 273-279.
45. Park, J., et al., *Ultra-large-scale syntheses of monodisperse nanocrystals.* Nature materials, 2004. **3**(12): p. 891.
46. Sun, S. and H. Zeng, *Size-controlled synthesis of magnetite nanoparticles.* Journal of the American Chemical Society, 2002. **124**(28): p. 8204-8205.
47. Li, Y., M. Afzaal, and P. O'Brien, *The synthesis of amine-capped magnetic (Fe, Mn, Co, Ni) oxide nanocrystals and their surface modification for aqueous dispersibility.* Journal of Materials Chemistry, 2006. **16**(22): p. 2175-2180.
48. Chen, Z., *Size and shape controllable synthesis of monodisperse iron oxide nanoparticles by thermal decomposition of iron oleate complex.* Synthesis and Reactivity in Inorganic, Metal-Organic, and Nano-Metal Chemistry, 2012. **42**(7): p. 1040-1046.
49. Xiong, B., et al., *Separation of nanorods by density gradient centrifugation.* Journal of Chromatography A, 2011. **1218**(25): p. 3823-3829.
50. Bao, Y., J. Sherwood, and Z. Sun, *Magnetic iron oxide nanoparticles as T 1 contrast agents for magnetic resonance imaging.* Journal of materials chemistry C, 2018. **6**(6): p. 1280-1290.
51. Shin, T.-H., et al., *Recent advances in magnetic nanoparticle-based multi-modal imaging.* Chemical Society Reviews, 2015. **44**(14): p. 4501-4516.
52. Wu, L., et al., *A review of magnetic particle imaging and perspectives on neuroimaging.* American Journal of Neuroradiology, 2019. **40**(2): p. 206-212.
53. Bauer, L.M., et al., *Magnetic particle imaging tracers: state-of-the-art and future directions.* The journal of physical chemistry letters, 2015. **6**(13): p. 2509-2517.
54. Biederer, S., et al., *Magnetization response spectroscopy of superparamagnetic nanoparticles for magnetic particle imaging.* Journal of Physics D: Applied Physics, 2009. **42**(20): p. 205007.
55. Bauer, L.M., et al., *High-performance iron oxide nanoparticles for magnetic particle imaging–guided hyperthermia (hMPI).* Nanoscale, 2016. **8**(24): p. 12162-12169.
56. Meola, A., et al., *"Magnetic Particle Imaging (MPI) in Neurosurgery".* World neurosurgery, 2019.
57. Herz, S., et al., *Magnetic particle imaging guided real-time percutaneous transluminal angioplasty in a phantom model.* Cardiovascular and interventional radiology, 2018. **41**(7): p. 1100-1105.

58. Pradhan, A., P.K. Pandey, and P. Singh, *Overview of Fluorescence Spectroscopy and Imaging for Early Cancer Detection*, in *Neurophotonics and Biomedical Spectroscopy*. 2019, Elsevier. p. 253-328.
59. Zhao, J., et al., *Recent developments in multimodality fluorescence imaging probes.* Acta pharmaceutica sinica B, 2018. **8**(3): p. 320-338.
60. Calin, M.A., et al., *Optical techniques for the noninvasive diagnosis of skin cancer.* Journal of cancer research and clinical oncology, 2013. **139**(7): p. 1083-1104.
61. CHRISTOPOULOS, T.K. and E.P. DIAMANDIS, *Fluorescence immunoassays*, in *Immunoassay*. 1996, Elsevier. p. 309-335.
62. Cui, B., et al., *The use of carbon quantum dots as fluorescent materials in white LEDs.* New Carbon Materials, 2017. **32**(5): p. 385-401.
63. Samelson, H. and A. Lempicki, *Fluorescence and lifetimes of Eu chelates.* The Journal of Chemical Physics, 1963. **39**(1): p. 110-112.
64. Olmsted III, J., *Oxygen quenching of fluorescence of organic dye molecules.* Chemical Physics Letters, 1974. **26**(1): p. 33-36.
65. Wang, G., et al., *Magneto-fluorescent nanoparticles with high-intensity NIR emission, T 1- and T 2-weighted MR for multimodal specific tumor imaging.* Journal of Materials Chemistry B, 2015. **3**(15): p. 3072-3080.
66. Fischer, I., et al., *Continuous protein purification using functionalized magnetic nanoparticles in aqueous micellar two-phase systems.* Journal of Chromatography A, 2013. **1305**: p. 7-16.
67. Huang, Y.-F., Y.-F. Wang, and X.-P. Yan, *Amine-functionalized magnetic nanoparticles for rapid capture and removal of bacterial pathogens.* Environmental science & technology, 2010. **44**(20): p. 7908-7913.
68. Hyeon, T.H., et al., *Preparation of extremely small and uniform sized, iron oxide-based paramagnetic or pseudo-paramagnetic nanoparticles and MRI T1 contrast agents using the same*. 2018, Google Patents.
69. Weizenecker, J., et al., *Three-dimensional real-time in vivo magnetic particle imaging.* Physics in Medicine & Biology, 2009. **54**(5): p. L1.
70. Laurent, S., et al., *Magnetic fluid hyperthermia: focus on superparamagnetic iron oxide nanoparticles.* Advances in colloid and interface science, 2011. **166**(1-2): p. 8-23.
71. Chin, A.B. and I.I. Yaacob, *Synthesis and characterization of magnetic iron oxide nanoparticles via w/o microemulsion and Massart's procedure.* Journal of materials processing technology, 2007. **191**(1): p. 235-237.
72. Albornoz, C. and S.E. Jacobo, *Preparation of a biocompatible magnetic film from an aqueous ferrofluid.* Journal of magnetism and magnetic materials, 2006. **305**(1): p. 12-15.
73. Salazar-Alvarez, G., M. Muhammed, and A.A. Zagorodni, *Novel flow injection synthesis of iron oxide nanoparticles with narrow size distribution.* Chemical engineering science, 2006. **61**(14): p. 4625-4633.
74. Kim, D., et al., *Synthesis and characterization of surfactant-coated superparamagnetic monodispersed iron oxide nanoparticles.* Journal of Magnetism and Magnetic Materials, 2001. **225**(1-2): p. 30-36.

75. Laurent, S., et al., *Magnetic iron oxide nanoparticles: synthesis, stabilization, vectorization, physicochemical characterizations, and biological applications.* Chemical reviews, 2008. **108**(6): p. 2064-2110.
76. Guardia, P., A. Labarta, and X. Batlle, *Tuning the size, the shape, and the magnetic properties of iron oxide nanoparticles.* The Journal of Physical Chemistry C, 2010. **115**(2): p. 390-396.
77. Obaidat, I.M., B. Issa, and Y. Haik, *Magnetic properties of magnetic nanoparticles for efficient hyperthermia.* Nanomaterials, 2015. **5**(1): p. 63-89.
78. Ding, J., et al., *Cell-specific cytotoxicity of dextran-stabilized magnetite nanoparticles.* Colloids and Surfaces B: Biointerfaces, 2010. **79**(1): p. 184-190.
79. Silva, V., et al., *Synthesis and characterization of Fe3O4 nanoparticles coated with fucan polysaccharides.* Journal of Magnetism and Magnetic Materials, 2013. **343**: p. 138-143.
80. Guidelli, E.J., A.P. Ramos, and O. Baffa, *Silver nanoparticle films for metal enhanced luminescence: toward development of plasmonic radiation detectors for medical applications.* Sensors and Actuators B: Chemical, 2016. **224**: p. 248-255.
81. Guidelli, E.J., A.P. Ramos, and O. Baffa, *Optically stimulated luminescence under plasmon resonance conditions enhances x-ray detection.* Plasmonics, 2014. **9**(5): p. 1049-1056.
82. Chomoucka, J., et al., *Magnetic nanoparticles and targeted drug delivering.* Pharmacological Research, 2010. **62**(2): p. 144-149.
83. Arias, J., et al., *Development of carbonyl iron/ethylcellulose core/shell nanoparticles for biomedical applications.* International journal of pharmaceutics, 2007. **339**(1-2): p. 237-245.
84. Dutz, S., et al., *Influence of dextran coating on the magnetic behaviour of iron oxide nanoparticles.* Journal of Magnetism and Magnetic Materials, 2007. **311**(1): p. 51-54.
85. Kalkan, N.A., et al., *Preparation of chitosan-coated magnetite nanoparticles and application for immobilization of laccase.* Journal of Applied Polymer Science, 2012. **123**(2): p. 707-716.
86. Kumari, A., V. Kumar, and S.K. Yadav, *Plant extract synthesized PLA nanoparticles for controlled and sustained release of quercetin: a green approach.* PLoS One, 2012. **7**(7): p. e41230.
87. Guidelli, E.J., et al., *Green synthesis of colloidal silver nanoparticles using natural rubber latex extracted from Hevea brasiliensis.* Spectrochimica Acta Part A: Molecular and Biomolecular Spectroscopy, 2011. **82**(1): p. 140-145.
88. Othman, A., C. Hepburn, and H. Hasma, *Influence of non-rubber constituents on elastic properties of natural rubber vulcanizates.* Plastics, Rubber and Composites Processing and Applications, 1993. **19**(3): p. 185-94.
89. Gaboriaud, F., et al., *Unravelling the nanometre-scale stimuli-responsive properties of natural rubber latex particles using atomic force microscopy.* Soft Matter, 2012. **8**(9): p. 2724-2729.
90. Neves-Junior, W., et al., *Influence of fabrication process on the final properties of natural-rubber latex tubes for vascular prosthesis.* Brazilian Journal of Physics, 2006. **36**(2B): p. 586-591.
91. Herculano, R.D., et al., *Natural rubber latex used as drug delivery system in guided bone regeneration (GBR).* Materials Research, 2009. **12**(2): p. 253-256.

92. Ereno, C., et al., *Latex use as an occlusive membrane for guided bone regeneration.* Journal of Biomedical Materials Research Part A, 2010. **95**(3): p. 932-939.
93. Sharp, W.V. and W.H. Falor, *Rubber latex tubing as a vascular prosthesis.* The American Journal of Surgery, 1963. **105**(6): p. 802-811.
94. Ferreira, M., et al., *Angiogenic properties of natural rubber latex biomembranes and the serum fraction of Hevea brasiliensis.* Brazilian Journal of Physics, 2009. **39**(3): p. 564-569.
95. Guidelli, É.J., et al., *Silver nanoparticles delivery system based on natural rubber latex membranes.* Journal of nanoparticle research, 2013. **15**(4): p. 1536.
96. Furuya, M., et al., *Cytotoxicity and anticancer activity of natural rubber latex particles for cancer cells.* Materials Today Chemistry, 2017. **5**: p. 63-71.
97. Araujo, J.F., et al., *A portable Hall magnetometer probe for characterization of magnetic iron oxide nanoparticles.* Journal of Magnetism and Magnetic Materials, 2017. **426**: p. 159-162.
98. Liyanage, N.K., *Collodial stability of natural rubber latex.* Bull. Rubber Res. Inst. Sri Lanka, 1999. **9**: p. 9-16.
99. Shen, M., et al., *The synthesis and characterization of monodispersed chitosan-coated Fe 3 O 4 nanoparticles via a facile one-step solvothermal process for adsorption of bovine serum albumin.* Nanoscale research letters, 2014. **9**(1): p. 296.
100. Guidelli, E.J., et al., *Synthesis and characterization of silver/alanine nanocomposites for radiation detection in medical applications: the influence of particle size on the detection properties.* Nanoscale, 2012. **4**(9): p. 2884-2893.
101. Balazs, A.C., T. Emrick, and T.P. Russell, *Nanoparticle polymer composites: where two small worlds meet.* Science, 2006. **314**(5802): p. 1107-1110.
102. Thompson, R.B., et al., *Predicting the mesophases of copolymer-nanoparticle composites.* Science, 2001. **292**(5526): p. 2469-2472.
103. Gómez-Lopera, S.A., et al., *Colloidal stability of magnetite/poly (lactic acid) core/shell nanoparticles.* Langmuir, 2006. **22**(6): p. 2816-2821.
104. Prokop, A., et al., *Hydrogel-based colloidal polymeric system for protein and drug delivery: physical and chemical characterization, permeability control and applications*, in *Filled Elastomers Drug Delivery Systems*. 2002, Springer. p. 119-173.
105. Beck-Broichsitter, M., et al., *Biophysical investigation of pulmonary surfactant surface properties upon contact with polymeric nanoparticles in vitro.* Nanomedicine: Nanotechnology, Biology and Medicine, 2011. **7**(3): p. 341-350.
106. Sansatsadeekul, J., J. Sakdapipanich, and P. Rojruthai, *Characterization of associated proteins and phospholipids in natural rubber latex.* Journal of bioscience and bioengineering, 2011. **111**(6): p. 628-634.
107. Eldridge, D.S., R.J. Crawford, and I.H. Harding, *The role of metal ion-ligand interactions during divalent metal ion adsorption.* Journal of colloid and interface science, 2015. **454**: p. 20-26.
108. Homola, A. and R. James, *Preparation and characterization of amphoteric polystyrene latices.* Journal of colloid and interface science, 1977. **59**(1): p. 123-134.
109. Todd, D.J., et al., *Cutaneous changes of nephrogenic systemic fibrosis: predictor of early mortality and association with gadolinium exposure.* Arthritis & Rheumatism: Official Journal of the American College of Rheumatology, 2007. **56**(10): p. 3433-3441.

110. Wang, Y., et al., *Synthesis of Fe3O4 magnetic fluid used for magnetic resonance imaging and hyperthermia.* Journal of Magnetism and Magnetic Materials, 2011. **323**(23): p. 2953-2959.
111. Lopez, J.A., et al., *Synthesis and characterization of Fe3O4 magnetic nanofluid.* Revista Latinoamericana de Metalurgia y Materiales, 2010. **30**(1): p. 60-66.
112. Guidelli, E., O. Baffa, and D. Clarke, *Enhanced UV emission from silver/ZnO and gold/ZnO core-shell nanoparticles: photoluminescence, radioluminescence, and optically stimulated luminescence.* Scientific reports, 2015. **5**: p. 14004.
113. Hang, D.-R., et al., *Annealing effects on the optical and morphological properties of ZnO nanorods on AZO substrate by using aqueous solution method at low temperature.* Nanoscale research letters, 2014. **9**(1): p. 632.
114. Xie, R., et al., *Enhancement and patterning of ultraviolet emission in ZnO with an electron beam.* Applied Physics Letters, 2006. **88**(13): p. 134103.
115. Mozaffari, M., et al., *The effect of cobalt substitution on magnetic hardening of magnetite.* Journal of Magnetism and Magnetic Materials, 2014. **354**: p. 119-124.
116. Jafari, A., et al., *Effect of annealing temperature on magnetic phase transition in Fe3O4 nanoparticles.* Journal of Magnetism and Magnetic Materials, 2015. **379**: p. 305-312.
117. Chen, D., et al., *Fourier transform infrared spectral analysis of polyisoprene of a different microstructure.* International Journal of Polymer Science, 2013. **2013**.
118. Dghim, F., et al., *Laticifers identification and natural rubber characterization from the latex of Periploca angustifolia Labill.(Apocynaceae).* Flora-Morphology, Distribution, Functional Ecology of Plants, 2015. **217**: p. 90-98.
119. Sun, X., et al., *β-Cyclodextrin-assisted synthesis of superparamagnetic magnetite nanoparticles from a single Fe (III) precursor.* The Journal of Physical Chemistry C, 2008. **112**(44): p. 17148-17155.
120. Farrell, E., et al., *Cell labelling with superparamagnetic iron oxide has no effect on chondrocyte behaviour.* Osteoarthritis and cartilage, 2009. **17**(7): p. 961-967.
121. Bucak, S., et al., *Protein separations using colloidal magnetic nanoparticles.* Biotechnology Progress, 2003. **19**(2): p. 477-484.
122. Hergt, R. and S. Dutz, *Magnetic particle hyperthermia—biophysical limitations of a visionary tumour therapy.* Journal of Magnetism and Magnetic Materials, 2007. **311**(1): p. 187-192.
123. Yoshida, Y., et al., *Ex vivo investigation of magnetically targeted drug delivery system.* Journal of Magnetism and Magnetic Materials, 2007. **310**(2): p. 2880-2882.
124. Corti, M., et al., *Magnetic and relaxometric properties of polyethylenimine-coated superparamagnetic MRI contrast agents.* Journal of Magnetism and Magnetic Materials, 2008. **320**(14): p. e316-e319.
125. Yoo, J.-W., *Toward improved selectivity of targeted delivery: The potential of magnetic nanoparticles.* Archives of pharmacal research, 2012. **35**(1): p. 1-2.
126. Li, X., et al., *Multimodality imaging in nanomedicine and nanotheranostics.* Cancer biology & medicine, 2016. **13**(3): p. 339.
127. Conlan, R., R. Ernst, and E. Hahn, *A life-saving window on the mind and body: The development of magnetic resonance imaging.* Beyond Discovery: The Path from Research to Human Benefit, 2001.

128. Kanda, T., et al., *High signal intensity in the dentate nucleus and globus pallidus on unenhanced T1-weighted MR images: relationship with increasing cumulative dose of a gadolinium-based contrast material.* Radiology, 2014. **270**(3): p. 834-841.
129. Rogosnitzky, M. and S. Branch, *Gadolinium-based contrast agent toxicity: a review of known and proposed mechanisms.* Biometals, 2016. **29**(3): p. 365-376.
130. Hasebroock, K.M. and N.J. Serkova, *Toxicity of MRI and CT contrast agents.* Expert opinion on drug metabolism & toxicology, 2009. **5**(4): p. 403-416.
131. Ahmad, T., et al., *Particle size dependence of relaxivity for silica-coated iron oxide nanoparticles.* Current Applied Physics, 2012. **12**(3): p. 969-974.
132. Arsalani, S., et al., *Green Synthesis and Surface Modification of Iron Oxide Nanoparticles with Enhanced Magnetization Using Natural Rubber Latex.* ACS Sustainable Chemistry & Engineering, 2018.
133. Kim, B.H., et al., *Large-scale synthesis of uniform and extremely small-sized iron oxide nanoparticles for high-resolution T 1 magnetic resonance imaging contrast agents.* Journal of the American Chemical Society, 2011. **133**(32): p. 12624-12631.
134. Taboada, E., et al., *Relaxometric and magnetic characterization of ultrasmall iron oxide nanoparticles with high magnetization. Evaluation as potential T 1 magnetic resonance imaging contrast agents for molecular imaging.* Langmuir, 2007. **23**(8): p. 4583-4588.
135. Zeng, L., et al., *Ultrasmall water-soluble metal-iron oxide nanoparticles as T 1-weighted contrast agents for magnetic resonance imaging.* Physical Chemistry Chemical Physics, 2012. **14**(8): p. 2631-2636.
136. Guardia, P., et al., *Surfactant effects in magnetite nanoparticles of controlled size.* Journal of Magnetism and Magnetic Materials, 2007. **316**(2): p. e756-e759.
137. Khurshid, H., et al., *Synthesis and magnetic properties of hybrid nanostructures of Pt–Fe x O y.* Journal of Materials Chemistry C, 2013. **1**(40): p. 6553-6558.
138. Salunkhe, A., et al., *Synthesis and magnetostructural studies of amine functionalized superparamagnetic iron oxide nanoparticles.* RSC Advances, 2015. **5**(24): p. 18420-18428.
139. Maggioni, D., et al., *Superparamagnetic iron oxide nanoparticles stabilized by a poly (amidoamine)-rhenium complex as potential theranostic probe.* Dalton Transactions, 2014. **43**(3): p. 1172-1183.
140. Fang, M., et al., *Particle size and magnetic properties dependence on growth temperature for rapid mixed co-precipitated magnetite nanoparticles.* Nanotechnology, 2012. **23**(14): p. 145601.
141. Tsoi, G., et al., *Memory effects in a superparamagnetic γ− Fe 2 O 3 system.* Physical Review B, 2005. **72**(1): p. 014445.
142. Del Bianco, L., et al., *Exchange bias and structural disorder in the nanogranular Ni⁄ Ni O system produced by ball milling and hydrogen reduction.* Physical Review B, 2008. **77**(9): p. 094408.
143. Urquijo Morales, J.P., et al., *One step synthesis of magnetic particles covered with casein surfactant.* Revista EIA, 2014(SPE1): p. 47-59.
144. Hajesmaeelzadeh, F., et al., *Effect of coating thickness of iron oxide nanoparticles on their relaxivity in the MRI.* Iranian journal of basic medical sciences, 2016. **19**(2): p. 166.

145. Lu, A.H., E.e.L. Salabas, and F. Schüth, *Magnetic nanoparticles: synthesis, protection, functionalization, and application.* Angewandte Chemie International Edition, 2007. **46**(8): p. 1222-1244.
146. Heikham, F.D. and D.S. Thiyam, *Fabrication of Spherical Magneto-Luminescent Hybrid MnFe2O4@ YPO4: 5 Eu3+ Nanoparticles for Hyperthermia Application.* ChemistrySelect, 2017. **2**(31): p. 10010-10019.
147. Arsalani, S., et al., *Magnetic Fe3O4 nanoparticles coated by natural rubber latex as MRI contrast agent.* Journal of Magnetism and Magnetic Materials, 2019. **475**: p. 458-464.
148. Arsalani, S., et al., *The effect of magnetization of natural rubber latex-coated magnetite nanoparticles on shear wave dispersion magneto-motive ultrasound.* Physics in Medicine & Biology, 2019. **64**(21): p. 215019.
149. Lu, H., et al., *Synthesis and characterization of multi-functional nanoparticles possessing magnetic, up-conversion fluorescence and bio-affinity properties.* Journal of Materials Chemistry, 2004. **14**(8): p. 1336-1341.
150. Xu, H., et al., *Antibody conjugated magnetic iron oxide nanoparticles for cancer cell separation in fresh whole blood.* Biomaterials, 2011. **32**(36): p. 9758-9765.
151. Gonzales-Weimuller, M., M. Zeisberger, and K.M. Krishnan, *Size-dependant heating rates of iron oxide nanoparticles for magnetic fluid hyperthermia.* Journal of magnetism and magnetic materials, 2009. **321**(13): p. 1947-1950.
152. Fortin, J.-P., et al., *Size-sorted anionic iron oxide nanomagnets as colloidal mediators for magnetic hyperthermia.* Journal of the American Chemical Society, 2007. **129**(9): p. 2628-2635.
153. Kayal, S. and R. Ramanujan, *Doxorubicin loaded PVA coated iron oxide nanoparticles for targeted drug delivery.* Materials Science and Engineering: C, 2010. **30**(3): p. 484-490.
154. Lee, J.H., et al., *All-in-one target-cell-specific magnetic nanoparticles for simultaneous molecular imaging and siRNA delivery.* Angewandte Chemie International Edition, 2009. **48**(23): p. 4174-4179.
155. Kaushik, A., et al., *Iron oxide-chitosan hybrid nanobiocomposite based nucleic acid sensor for pyrethroid detection.* Biochemical Engineering Journal, 2009. **46**(2): p. 132-140.
156. Ortega, D., *Structure and magnetism in magnetic nanoparticles.* Magnetic Nanoparticles: From Fabrication to Clinical Applications, 2012: p. 3.
157. Corr, S.A., Y.P. Rakovich, and Y.K. Gun'ko, *Multifunctional magnetic-fluorescent nanocomposites for biomedical applications.* Nanoscale Research Letters, 2008. **3**(3): p. 87.
158. Govindaiah, P., et al., *Luminescent iron oxide nanoparticles prepared by one-pot aphen-functionalization.* Macromolecular research, 2010. **18**(11): p. 1109-1114.
159. Zhang, X.Q., et al., *Multimodal nanodiamond drug delivery carriers for selective targeting, imaging, and enhanced chemotherapeutic efficacy.* Advanced materials, 2011. **23**(41): p. 4770-4775.
160. Serrano García, R., S. Stafford, and Y. Gun'ko, *Recent progress in synthesis and functionalization of multimodal fluorescent-magnetic nanoparticles for biological applications.* Applied Sciences, 2018. **8**(2): p. 172.
161. Yu, C.-J., S.-M. Wu, and W.-L. Tseng, *Magnetite nanoparticle-induced fluorescence quenching of adenosine triphosphate–BODIPY conjugates: application to adenosine*

triphosphate and pyrophosphate sensing. Analytical chemistry, 2013. **85**(18): p. 8559-8565.

162. Song, C., G.-Y. Wang, and D.-M. Kong, *A facile fluorescence method for versatile biomolecular detection based on pristine α-Fe2O3 nanoparticle-induced fluorescence quenching.* Biosensors and Bioelectronics, 2015. **68**: p. 239-244.
163. Xu, Y., et al., *Multifunctional Fe3O4 cored magnetic-quantum dot fluorescent nanocomposites for RF nanohyperthermia of cancer cells.* The Journal of Physical Chemistry C, 2010. **114**(11): p. 5020-5026.
164. Lim, E.-K., et al., *Self-assembled fluorescent magnetic nanoprobes for multimode-biomedical imaging.* Biomaterials, 2010. **31**(35): p. 9310-9319.
165. de Sousa Silvaa, R.L., et al., *Luminescent and Magnetic Properties of Fe3O4@ SiO2: phen: Eu3.* Materials Research, 2017. **20**(5): p. 1317-1321.
166. Islam, M.N., et al., *Silica encapsulation of sonochemically synthesized iron oxide nanoparticles.* Electronic Materials Letters, 2013. **9**(6): p. 817-820.
167. Ramazani, A., et al., *Development and Characterization of Thermosensitive Polymer-Coated Iron Oxide Nanoparticles as a Novel Ferrofluid.* J Biomim Biomater Tissue Eng, 2013. **18**(111): p. 2.
168. Chen, H., et al., *Magnetic and optical properties of multifunctional core–shell radioluminescence nanoparticles.* Journal of materials chemistry, 2012. **22**(25): p. 12802-12809.
169. Lai, C.W., et al., *Iron oxide nanoparticles decorated oleic acid for high colloidal stability.* Advances in Polymer Technology, 2018. **37**(6): p. 1712-1721.
170. Sinha, N., et al., *Enhancement in semiconducting and optical properties in doped anthracene micro crystals.* Physica B: Condensed Matter, 2015. **470**: p. 15-20.
171. Sinha, N., et al., *Effect of zinc chloride on structural, optical and dielectric behavior of solution grown anthracene crystal.* Physica B: Condensed Matter, 2011. **406**(17): p. 3206-3209.
172. Ren, C., et al., *Preparation and properties of a new multifunctional material composed of superparamagnetic core and rhodamine B doped silica shell.* Nanotechnology, 2007. **18**(34): p. 345604.
173. Zhang, Y., J. Cheng, and W. Liu, *Characterization and Relaxation Properties of a Series of Monodispersed Magnetic Nanoparticles.* Sensors, 2019. **19**(15): p. 3396.
174. Burnham, P., et al., *Magnetization and specific absorption rate studies of ball-milled iron oxide nanoparticles for biomedicine.* Journal of Nanoparticles, 2013. **2013**.
175. Zhang, L., R. He, and H.-C. Gu, *Oleic acid coating on the monodisperse magnetite nanoparticles.* Applied Surface Science, 2006. **253**(5): p. 2611-2617.
176. Chen, M.-J., et al., *Magnetic fluids' stability improved by oleic acid bilayer-coated structure via one-pot synthesis.* Chemical Papers, 2016. **70**(12): p. 1642-1648.
177. Willis, A.L., N.J. Turro, and S. O'Brien, *Spectroscopic characterization of the surface of iron oxide nanocrystals.* Chemistry of materials, 2005. **17**(24): p. 5970-5975.
178. Montagne, F., et al., *Preparation and characterization of narrow sized (o/w) magnetic emulsion.* Journal of magnetism and magnetic materials, 2002. **250**: p. 302-312.
179. Masur, S., et al., *Characterization of the oleic acid/iron oxide nanoparticle interface by magnetic resonance.* Journal of Magnetism and Magnetic Materials, 2016. **415**: p. 8-12.

180. Deacon, G. and R. Phillips, *Relationships between the carbon-oxygen stretching frequencies of carboxylato complexes and the type of carboxylate coordination.* Coordination Chemistry Reviews, 1980. **33**(3): p. 227-250.
181. Cataldo, F., D.A. García-Hernández, and A. Manchado, *Sonochemical synthesis of fullerene C60/anthracene diels-alder mono and bis-adducts.* Fullerenes, Nanotubes and Carbon Nanostructures, 2014. **22**(6): p. 565-574.
182. Pereira da Silva, S., D. Costa de Moraes, and D. Samios, *Iron oxide nanoparticles coated with polymer derived from epoxidized oleic acid and cis-1, 2-cyclohexanedicarboxylic anhydride: synthesis and characterization.* J Material Sci Eng, 2016. **5**(247): p. 2169-0022.1000247.
183. Jadhav, N.V., et al., *Synthesis of oleic acid functionalized Fe3O4 magnetic nanoparticles and studying their interaction with tumor cells for potential hyperthermia applications.* Colloids and Surfaces B: Biointerfaces, 2013. **108**: p. 158-168.
184. Mahdavi, M., et al., *Synthesis, surface modification and characterisation of biocompatible magnetic iron oxide nanoparticles for biomedical applications.* Molecules, 2013. **18**(7): p. 7533-7548.
185. Niculaes, D., et al., *Asymmetric assembling of iron oxide nanocubes for improving magnetic hyperthermia performance.* ACS nano, 2017. **11**(12): p. 12121-12133.
186. Osuntokun, J. and P.A. Ajibade, *Structural and thermal studies of ZnS and CdS nanoparticles in polymer matrices.* Journal of Nanomaterials, 2016. **2016**.
187. Begum, M.H.A., et al., *Preparation and characterization of polyvinyl alcohol–starch composites reinforced with pulp.* SN Applied Sciences, 2019. **1**(9): p. 1091.
188. Baffa, O., et al., *Development of an optical pumped gradiometric system to detect magnetic relaxation of magnetic nanoparticles.* Journal of Magnetism and Magnetic Materials, 2019. **475**: p. 533-538.
189. Valeur, B., *Molecular fluorescence.* digital Encyclopedia of Applied Physics, 2003: p. 477-531.
190. Berezin, M.Y. and S. Achilefu, *Fluorescence lifetime measurements and biological imaging.* Chemical reviews, 2010. **110**(5): p. 2641-2684.
191. Lakowicz, J.R., *Principles of fluorescence spectroscopy*. 2013: Springer Science & Business Media.
192. Guidelli, E.J., et al., *Mechanistic insights and controlled synthesis of radioluminescent ZnSe quantum dots using a microfluidic reactor.* Chemistry of Materials, 2018. **30**(23): p. 8562-8570.
193. Janczak, C.M., et al., *Polystyrene-Core, Silica-Shell Scintillant Nanoparticles for Low-Energy Radionuclide Quantification in Aqueous Media.* ACS applied materials & interfaces, 2018. **10**(5): p. 4953-4960.
194. Banerjee, S., A.K. Both, and M. Sarkar, *Probing the Aggregation and Signaling Behavior of Some Twisted 9, 9′-Bianthryl Derivatives: Observation of Aggregation-Induced Blue-Shifted Emission.* ACS Omega, 2018. **3**(11): p. 15709-15724.
195. Umar, A. and S. Atabo, *A review of imaging techniques in scientific research/clinical diagnosis.* MOJ Anat & Physiol, 2019. **6**(5): p. 175-183.
196. Du, Y., et al., *Design of superparamagnetic nanoparticles for magnetic particle imaging (MPI).* International journal of molecular sciences, 2013. **14**(9): p. 18682-18710.

197. Araujo, J.F., et al., *Novel scanning magnetic microscopy method for the characterization of magnetic nanoparticles.* Journal of Magnetism and Magnetic Materials, 2020. **499**: p. 166300.
198. Ziemian, S., et al., *Optimization of iron oxide tracer synthesis for magnetic particle imaging.* Nanomaterials, 2018. **8**(4): p. 180.
199. Yoshida, T., T. Sasayama, and K. Enpuku, *Effect of core size distribution of immobilized magnetic nanoparticles on harmonic magnetization.* International Journal on Magnetic Particle Imaging, 2017. **3**(1).
200. Pacakova, B., et al., *Spinel ferrite nanoparticles: correlation of structure and magnetism.* Magnetic Spinels–Synthesis, Properties and Applications, 2017: p. 4-6.
201. Petosa, A.R., et al., *Aggregation and deposition of engineered nanomaterials in aquatic environments: role of physicochemical interactions.* Environmental science & technology, 2010. **44**(17): p. 6532-6549.
202. Gutiérrez, L., et al., *Aggregation effects on the magnetic properties of iron oxide colloids.* Nanotechnology, 2019.
203. Arami, H., et al., *In vivo delivery, pharmacokinetics, biodistribution and toxicity of iron oxide nanoparticles.* Chemical Society Reviews, 2015. **44**(23): p. 8576-8607.
204. Arsalani, S., et al., *Synthesis of Radioluminescent Iron Oxide Nanoparticles Functionalized by Anthracene for Biomedical Applications.* Colloids and Surfaces A: Physicochemical and Engineering Aspects, 2020: p. 125105.
205. Latham, A.H., et al., *Capillary magnetic field flow fractionation and analysis of magnetic nanoparticles.* Analytical chemistry, 2005. **77**(15): p. 5055-5062.
206. Löwa, N., et al., *Hyphenation of field-flow fractionation and magnetic particle spectroscopy.* Chromatography, 2015. **2**(4): p. 655-668.
207. Stephens, J.R., J.S. Beveridge, and M.E. Williams, *Analytical methods for separating and isolating magnetic nanoparticles.* Physical Chemistry Chemical Physics, 2012. **14**(10): p. 3280-3289.
208. Löwa, N., et al., *Hydrodynamic and magnetic fractionation of superparamagnetic nanoparticles for magnetic particle imaging.* Journal of Magnetism and Magnetic Materials, 2015. **380**: p. 266-270.
209. De Las Cuevas, G., J. Faraudo, and J. Camacho, *Low-gradient magnetophoresis through field-induced reversible aggregation.* The Journal of Physical Chemistry C, 2008. **112**(4): p. 945-950.
210. Yavuz, C.T., et al., *Low-field magnetic separation of monodisperse Fe3O4 nanocrystals.* science, 2006. **314**(5801): p. 964-967.
211. Leong, S.S., S.P. Yeap, and J. Lim, *Working principle and application of magnetic separation for biomedical diagnostic at high-and low-field gradients.* Interface focus, 2016. **6**(6): p. 20160048.
212. Andreu, J., et al., *Simple analytical model for the magnetophoretic separation of superparamagnetic dispersions in a uniform magnetic gradient.* Physical Review E, 2011. **84**(2): p. 021402.
213. Benelmekki, M., et al., *Horizontal low gradient magnetophoresis behaviour of iron oxide nanoclusters at the different steps of the synthesis route.* Journal of Nanoparticle Research, 2011. **13**(8): p. 3199-3206.

214. Lim, J., et al., *Magnetophoresis of iron oxide nanoparticles at low field gradient: the role of shape anisotropy.* Journal of colloid and interface science, 2014. **421**: p. 170-177.
215. Benelmekki, M., et al., *Magnetophoresis of colloidal particles in a dispersion of superparamagnetic nanoparticles: theory and experiments.* Soft Matter, 2012. **8**(22): p. 6039-6047.
216. Ahrentorp, F., et al., *Sensitive magnetic biodetection using magnetic multi-core nanoparticles and RCA coils.* Journal of Magnetism and Magnetic Materials, 2017. **427**: p. 14-18.
217. Ludwig, F., et al., *Analysis of ac susceptibility spectra for the characterization of magnetic nanoparticles.* IEEE Transactions on Magnetics, 2017. **53**(11): p. 1-4.
218. Kosch, O., et al., *Evaluation of a separate-receive coil by magnetic particle imaging of a solid phantom.* Journal of Magnetism and Magnetic Materials, 2019. **471**: p. 444-449.